

---

---

LUDWIG-MAXIMILIANS-UNIVERSITÄT MÜNCHEN

Radiative Cooling  
and  
Optical Temperature Sensing

---

Nicola Mara Kerschbaumer

München 2022

---

---



# Radiative Cooling and Optical Temperature Sensing

Dissertation

to obtain the doctoral degree of natural sciences (Dr. rer. nat.)



at the faculty of Physics

of the Ludwig-Maximilians-Universität München

submitted by

**Nicola Mara Kerschbaumer**

from Starnberg

Munich, August 11<sup>th</sup> 2022

Doctoral committee

First referee: Prof. Dr. Jochen Feldmann

Second referee: Prof. Dr. Thomas Klar

Chairman: Prof. Dr. Joachim Rädler

Assessor: Prof. Dr. Jan von Delft

Date of the oral exam: October 18<sup>th</sup> 2022

# Radiatives Abkühlen und optische Temperaturmessungen

Dissertation

zur Erlangung des Doktorgrades der Naturwissenschaften (Dr. rer. nat.)



an der Fakultät für Physik

der Ludwig-Maximilians-Universität München

vorgelegt von

**Nicola Mara Kerschbaumer**

aus Starnberg

München, 11. August 2022

Promotionskommission

Erstgutachter: Prof. Dr. Jochen Feldmann

Zweitgutachter: Prof. Dr. Thomas Klar

Vorsitzender: Prof. Dr. Joachim Rädler

Beisitzer: Prof. Dr. Jan von Delft

Tag der mündlichen Prüfung: 18. Oktober 2022

*dedicated to my parents, who always supported my curiosity*





## Publications, Conferences and Awards

### Scientific Publications of Results Presented in This Work

- N. M. Kerschbaumer, S. Niedermaier, T. Lohmüller, J. Feldmann  
*Contactless and spatially structured cooling by directing thermal radiation*  
**Scientific Reports** 11(1): 16209 (2021)
- N. M. Kerschbaumer, L. I. Fochler, M. Reichenspurner, S. Rieger, M. Fedoruk, J. Feldmann, T. Lohmüller  
*Twisted light Michelson interferometry for high precision refractive index measurements*  
**Optics Express** 30(16): 29722-29734 (2022)

### Additional Publications of My Time as a PhD Student

- S. Rieger, S. Schönweitz, K. Frank, T. Fürmann, N. M. Kerschbaumer, V. Steidl, J. Fang, M. Döblinger, B. Nickel, J. K. Stolarczyk, J. Feldmann  
*Anisotropic polarons and self-trapping in bismuth oxyiodide (BiOI) nanoplatelets*  
**ACS Nano** under review (2022)


### Conferences and Workshops

- *Workshop on Optical Spectroscopy of New Materials 2019* (Talk)  
Haigerloch, Germany, March 2019
- *DPG Summer School - Exciting Nanostructures: Characterizing Advanced Confined Systems* (Poster)  
Bad Honnef, Germany, July 2019
- *CLEO Europe/EQEC Conference* (Poster)  
virtual, June 2021
- *European Optical Society Annual Meeting "EOSAM"* (Talk)  
Rom, Italy, September 2021
- *Photothermal Effects in Plasmonics* (Poster)  
Porquerolles, France, October 2021
- *SPIE Photonics West* (Talk)  
San Francisco (hybrid), USA, January 2022

- *Optical Spectroscopy of new Materials (Optima) 2022 (Talk)*  
Fall-Lenggris, Germany, July 2022

## Awards and more

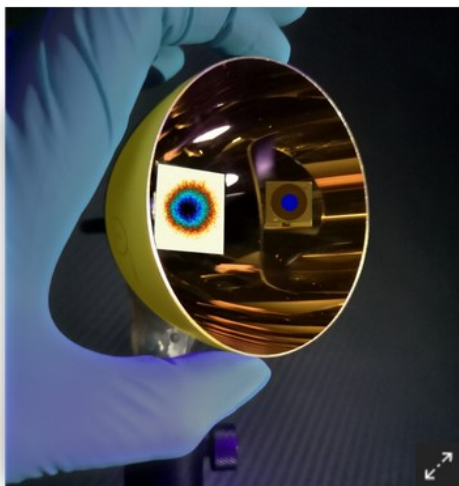
- **CeNS Travel Award**  
*SPIE Photonics West (Talk)*  
San Francisco (hybrid), USA, January 2022
- **News Publication**  
*One-way for thermal radiation*  
Ludwig-Maximilians-Universität München 2021



# One-way for thermal radiation

1 Sep 2021

LMU physicists have developed a novel method for contactless cooling of objects.



Contactless cooling of a sample by directional steering of thermal radiation. Nicola Kerschbaumer | © Jochen Feldmann/ LMU

Everyone knows what it's like to be out on a cold and cloudless winter night when the skies are studded with stars. In the open the cold is all too keenly felt. But in a forest, under the protective cover of the trees, it is less so. The reason for this difference is thermal radiation, which is emitted by the body and, depending on the nature of one's surroundings, may be replaced by a smaller amount of radiation emanating from the environment. With a temperature of  $-270^{\circ}\text{C}$ , the Universe is far colder than our own immediate surroundings, and therefore emits hardly any thermal radiation. Research groups around the world have recently begun to explore novel methods for cooling buildings and clothing, even in broad daylight, by enhancing the rate of heat exchange with the Universe – without the need for further energy consumption. However, potential applications of these methods for technological or experimental purposes – on a small scale – have rarely been investigated up to now.

Researchers led by Professor [Jochen Feldmann](#) at LMU's Nano-Institute have now succeeded in generating a cold gradient in an experimental sample by targeted and contactless control of the distribution of thermal radiation. "To do so, we simulated the effect of the remote Universe with the aid of a distant cryostat," says Nicola Kerschbaumer, a PhD student in Feldmann's team and first author of the

# Zusammenfassung

Temperatur und Licht sind untrennbar miteinander verbunden. Wärmestrahlung beeinflusst Temperatur und Temperatur beeinflusst optische Eigenschaften von Materialien. Ziel dieser Arbeit ist, diese Wechselbeziehung einerseits zur radiativen Kühlung von Körpern zu verwenden, und andererseits Licht für ein neuartiges Temperaturmessverfahren zu nutzen.

In den letzten Jahren hat das Konzept der passiven radiativen Kühlung für Anwendungen auf dem Gebiet der Wärmeregulierung von Gebäuden und der Energieeinsparung immer mehr Aufmerksamkeit auf sich gezogen. Auf diesem Gebiet werden nanophotonische Oberflächen entwickelt, um Wärmestrahlung im atmosphärischen Fenster zu emittieren, während gleichzeitig Sonnenlicht reflektiert wird. Das Ergebnis ist ein Netto-Kühleffekt, der keinen Energieaufwand erfordert. Diese Kühlwirkung kann weiter verbessert werden, wenn die Möglichkeit zur systematischen Lenkung von Wärmestrahlung, d.h. von elektromagnetischen Wellen, mithilfe von optischen Elementen in Betracht gezogen wird. Bisher wurde die Idee, Wärmestrahlung zur berührungslosen Kühlung zu fokussieren, noch kaum untersucht. In der ersten Hälfte dieser Arbeit wird durch Anwendung eines elliptischen Spiegels der Sichtfaktor der radiativen Wärmeübertragung um einen Faktor 92 gesteigert. Mit diesem Ansatz werden verschiedene Proben durch Strahlung gekühlt und räumlich strukturierte Kühlungsmuster entstehen auf ihren Oberflächen. Zu den ersten Anwendungen unter Ausnutzung dieses Kühlweges zählt auch die Unterkühlung von Flüssigkeiten.

In der zweiten Hälfte dieser Dissertation wird ein neuartiges Verfahren zur hochpräzisen Temperaturmessung eingeführt. In diesem Fall wird die Temperatur genutzt, um Strahlung zu beeinflussen. Dieses Konzept beruht auf der Temperaturabhängigkeit des Brechungsindex, was wiederum die ein Medium durchdringende Strahlung beeinflusst. Zur Nutzung dieser Abhängigkeit wird ein Interferometer in einer Michelson-Konfiguration gebaut und transparente Flüssigkeitsproben werden in einem der Arme platziert. Gedrehte Lichtmoden, die einen Bahndrehimpuls enthalten, werden verwendet, da die Interferenz derartiger Strahlen mit entgegengesetzter Helizität ein Interferenzmuster ergibt, das für Phasenveränderung empfindlich ist, d.h. jegliche Veränderung des Brechungsindex der untersuchten Probe. Mit diesem Aufbau werden Änderungen des Brechungsindex mit einer Auflösung in der Größenordnung von  $10^{-7}$  messbar. Neben der bereits genannten Temperaturabhängigkeit steht der Brechungsindex auch mit der Konzentration der Flüssigkeitsproben in Relation. Diese beiden Parameter werden unabhängig voneinander untersucht und das Interferometer erzielt Auflösungen im  $\mu\text{K}$ - und  $\mu\text{M}$ -Bereich bei Temperatur- beziehungsweise Konzentrationsmessungen. Die Anwendung dieser Art von Interferometrie mit gedrehtem Licht führt zu einem neuen, stabilen und leicht umzusetzenden Verfahren für die Überwachung von Temperatur und Konzentration in Flüssigkeitsproben *in situ*.



# Abstract

Temperature and light are intrinsically related to each other. Thermal radiation impacts temperature and temperature impacts optical properties of materials. The aim of this work is to use this relationship to radiatively cool down bodies on the one hand and to employ light for a novel temperature sensing method on the other hand.

Over the course of the last years, the concept of passive radiative cooling has become a topic of considerable interest for applications in the context of thermal building management and energy saving. In this field, nanophotonic surfaces are engineered to emit thermal radiation in the atmospheric window, while simultaneously reflecting sunlight. The result is a net cooling effect that does not require energy input. This cooling can be further enhanced when considering the possibility to systematically direct thermal radiation, i.e., electromagnetic waves with the aid of optical elements. Prior to this work, the idea to focus thermal radiation for contactless cooling was only scarcely explored. In the first half of this work an elliptical mirror is applied to increase the view factor of radiative heat transfer by a factor of 92. With this approach various samples are cooled down radiatively and spatially structured cooling patterns are generated on their surfaces. First applications exploiting this cooling pathway even include the supercooling of liquids.

In the second half of this thesis a novel method for ultra-precise temperature measurements is introduced. In this case temperature is used to manipulate radiation. This concept relies on the temperature-dependence of the refractive index, which in turn influences radiation passing through a medium. To utilize this dependence, an interferometer in a Michelson configuration is built and transparent liquid samples are placed in one of the arms. Twisted light modes containing orbital angular momentum are used, since interfering such beams with opposing helicity yields an interference pattern, which is sensitive to any phase change, i.e., any refractive index change of the observed sample. With this setup refractive index changes on the order of  $10^{-7}$  can be resolved. Besides the already mentioned temperature-dependence, the refractive index also relies on the concentration of the liquid samples. Both of these parameters are studied independently and the interferometer achieves resolutions in the  $\mu\text{K}$  and  $\mu\text{M}$  range for temperature and concentration measurements, respectively. Applying this type of twisted light interferometry yields a novel, robust and easily implemented method for *in situ* temperature and concentration monitoring in liquid samples.



# Contents

<b>Zusammenfassung</b>	<b>vii</b>
<b>Abstract</b>	<b>ix</b>
<b>1 Introduction</b>	<b>1</b>
<b>2 Fundamentals</b>	<b>5</b>
2.1 Radiative Cooling . . . . .	6
2.1.1 Pathways of Heat Transfer in Physical Systems . . . . .	6
2.1.2 Black Body Radiation . . . . .	11
2.1.3 Absorptivity and Emissivity . . . . .	14
2.1.4 Applications of Radiative Cooling: From the Universe to the Laboratory	16
2.2 Optical Temperature Sensing . . . . .	22
2.2.1 Interferometric Temperature Measurements . . . . .	22
2.2.2 Michelson Interferometer . . . . .	23
2.2.3 Light Modes . . . . .	24
2.2.4 Interfering OAM Beams . . . . .	31
<b>3 Directing Thermal Radiation for Spatially Structured Cooling</b>	<b>35</b>
3.1 Thermal Emitter and Absorber . . . . .	36
3.1.1 Black Body Emission . . . . .	36
3.1.2 Highly Emissive Hot Sample . . . . .	37
3.1.3 Absorbing Cold Reservoir . . . . .	38
3.1.4 Cooling Power . . . . .	39
3.2 Directing Thermal Radiation . . . . .	39
3.2.1 Manipulating the View Factor . . . . .	40
3.2.2 Enhancing the View Factor by Optics . . . . .	41
3.2.3 Quantification of the View Factor Enhancement . . . . .	43

---

3.3	Experimental Setup . . . . .	44
3.4	Creating a Lateral Temperature Profile . . . . .	46
3.4.1	Central Minimum . . . . .	47
3.4.2	Shaping the Thermal Pattern . . . . .	50
3.5	Radiative Cooling Dynamics . . . . .	51
3.5.1	Metal Velvet Sample . . . . .	52
3.5.2	Biological Sample . . . . .	54
3.6	Radiative Supercooling . . . . .	55
3.6.1	Supercooling: Cooling Liquids Below Their Freezing Point . . . . .	55
3.6.2	Microfluidic Chips . . . . .	57
3.6.3	Supercooling Dynamics . . . . .	58
<b>4</b>	<b>Temperature Sensing With Twisted Light</b>	<b>63</b>
4.1	Setup of an Orbital Angular Momentum Interferometer . . . . .	63
4.1.1	Light Source and Basic Optical Components . . . . .	64
4.1.2	Spiral Phase Plates . . . . .	65
4.1.3	Turning Helicity . . . . .	66
4.2	Determination of the Interference Pattern Rotation . . . . .	67
4.2.1	Daisy Flower Interference Pattern . . . . .	67
4.2.2	Evaluation Software . . . . .	69
4.2.3	Resolution Limit . . . . .	71
4.3	Measuring Temperature With Twisted Light . . . . .	73
4.3.1	Measurement Conditions . . . . .	73
4.3.2	Temperature Sensing Results . . . . .	76
4.3.3	Determination of the Thermo-Optic Coefficient . . . . .	78
4.4	Beyond Temperature: Concentration Measurements . . . . .	80
4.4.1	Sodium Chloride . . . . .	81
4.4.2	Glucose . . . . .	83
4.4.3	Comparison to Literature Values . . . . .	85
4.5	Benchmarking the OAM Interferometer . . . . .	88



Contents	1
4.5.1 Shot Noise and Phase Noise . . . . .	89
4.5.2 Interferometer Comparison . . . . .	90
<b>5 Conclusion</b>	<b>93</b>
<b>References</b>	<b>97</b>
<b>List of Figures</b>	<b>114</b>
<b>List of Tables</b>	<b>115</b>
<b>Acknowledgments</b>	<b>117</b>



# 1 Introduction

*Nothing is more important to us on Earth than the Sun. Without the Sun's heat and light, the Earth would be a lifeless ball of ice-coated rock. The Sun warms our seas, stirs our atmosphere, generates our weather patterns, and gives energy to the growing green plants that provide the food and oxygen for life on Earth. – NASA<sup>1</sup>*

As beautifully phrased by the NASA, solar radiation is what enables life on Earth in the first place. In combination with the atmosphere, radiation incident on Earth from the Sun creates this unique environment within a cold universe. The Earth, on the other hand, emits excess heat in the form of thermal radiation in the infrared range through the atmosphere, which acts as a selective transmitter, to the cold universe. Substantial disturbances to this system, for example an increasingly opaque atmosphere, cause a rise of temperature on Earth and a significant effect on our climate. During the course of this thesis, heat records were broken almost every year in various countries<sup>2</sup> and heat waves are predicted to occur more frequently, last longer and at higher temperatures in the near future.<sup>3</sup>

Actively using the cold universe as a heat sink for cooling via radiation away from Earth is a concept already known to ancient civilizations. For example, in desert countries this concept was used for the nocturnal production of ice.<sup>4</sup> However, it was not until 2014 when Raman *et al.*<sup>5</sup> were the first to successfully engineer a nanophotonic device that could effectively enable such radiative cooling also during the day. This material combines a high emission within the atmospheric window, with simultaneous

high reflectivity in the visible range. Thereby, daytime ambient radiative cooling was enabled for housing applications. With such cooling surfaces substantial temperature differences of up to 40 °C below ambient<sup>6</sup> were achieved.

Thermal radiation is widely utilized in various scientific and engineering applications for temperature manipulation. Predominately, it is discussed in the context of heating bodies. Photothermal effects are extensively applied in generating temperature gradients, thermophoresis and multiple further applications. In contrast, actively cooling with thermal radiation is only scarcely applied in the laboratory. Since the energy flow is always from hot to cold, funneling energy for a net cooling effect requires thermal engineering. This close interplay of thermal radiation and temperature, and more specifically the interaction of thermal radiation and matter, is studied in this work. In the first half, thermal radiation is emitted away from a body to cool it down. In the second half, light is radiated onto a body to measure its temperature. Thereby, two novel methods of providing contactless, radiative means to manipulate and measure temperature are introduced.

Radiative cooling is enhanced by using geometrical optics and thereby directing thermal radiation. This can be thought of as an analogy to using a magnifying glass to focus sunlight, but the other way around. A new setup is devised, in which the cold universe is exchanged by a cryostat and instead of the Earth a sample emitter is investigated. Put in simple words, radiative cooling was brought from the universe into the laboratory. An elliptical mirror directs thermal radiation for enhanced and structured radiative cooling. Importantly, the setup is not placed in a vacuum but in ambient conditions, thus enabling a high applicability. Thermal conduction and convection counteract the radiative cooling pathway and impose a limitation. Fundamental physical laws, concepts and phenomena governing thermal radiation are introduced in the first half of [Chapter 2](#). In [Chapter 3](#), ambient radiative cooling is studied experimentally. The view factor coverage, i.e., the solid angle of radiation, is specifically optimized. First applications include radiative supercooling as well as the cooling of a biological sample in form of a plant leaf. It is often overlooked that several floral species have extremely high emissivities in the atmospheric window<sup>7-9</sup> and thus may contribute to natural radiative cooling.

Light, however, can not only be used to manipulate temperature, but also to measure temperature itself. The impact of temperature on the refractive index is exploited for such measurements. Many optical properties of materials are temperature-dependent and thus in turn it is possible to deduct information about the temperature of a body. As

---

a second method, a special type of interferometer is built for high-precision temperature measurements using beams containing orbital angular momentum. Interfering beams with such light modes results in a specific interference pattern, enabling high-precision measurements of refractive index changes. The fundamentals of these helical light modes and their interference patterns are introduced in the second half of [Chapter 2](#). The experimental setup of the interferometer as well as the obtained results constitute [Chapter 4](#). Since a change in refractive index can not only be caused by temperature, the principle is extended to also determine the concentration of solutions.



# 2

## Fundamentals

*This chapter introduces the physical phenomena governing the relation of thermal radiation and temperature  $h\nu \leftrightarrow T$ . First, the concept of heat transfer, especially via thermal radiation, is introduced. The laws of Gustav Kirchhoff, Max Planck and Wilhelm Wien constitute the framework for the physical description of thermal radiation, based on the theoretical concept of a black body.*

*Secondly, the possibility to measure temperature with light is discussed. This is considered in the form of temperature influencing the refractive index of materials, causing a measurable change. Interferometry and Laguerre Gaussian light modes are introduced, which, taken together, provide the basis to measure refractive index changes that can be correlated to changes in temperature.*

## 2.1 Radiative Cooling

Radiative cooling describes the process of cooling down a body via its own thermal radiation. This is a direct consequence of the first law of thermodynamics, which is based on the conservation of energy. It is conceptually easier to grasp when imagining two bodies within an isolated system. The total energy inside this system is constant per definition. However, the two bodies can exchange energy with each other. Mathematically this can be expressed as<sup>10</sup>

$$\Delta U_1 = Q_2 - W_1, \quad (2.1)$$

in which  $\Delta U_1$  is the internal energy of the first body,  $Q_2$  is the heat supplied to the first body by the second body, which can be negative, and  $W_1$  is the work done by the first body on the second body. In the same fashion, Equation 2.1 could be formulated for the perspective of the second body.<sup>11,12</sup>

The possibility for such energy exchange between two bodies relies on the pathways of thermal energy transfer. The bodies will exchange thermal energy with each other, however, the net energy transferred is determined by the direction of heat exchange, which is always from hot to cold. The warmer of the two bodies therefore experiences a cooling effect.

### 2.1.1 Pathways of Heat Transfer in Physical Systems

Although this work focuses on radiative heat transfer, the other pathways, i.e., conduction and convection, have to be considered as well since all three processes always take place simultaneously. Again, the thermal exchange between the two bodies is considered. For thermal conduction and convection, the energy transfer rate has a linear or quadratic dependence on the temperature difference  $\Delta T$  of the two bodies.<sup>13</sup> In contrast, for thermal energy transfer via the radiative pathway, the transferred energy rate depends on  $\Delta T^4$ . It is most relevant at high temperature differences and is commonly considered in astrophysical applications, where hot bodies, such as stars, are located in the cold universe.<sup>14</sup> Thermal radiation also plays a role in everyday situations. For example in buildings, the energy transferred to the surrounding environment via radiation is often of a similar magnitude as the energy transferred by convection.<sup>13</sup>



## Thermal Conduction

Heat flow within a material along a temperature gradient from regions of high temperature to regions of low temperature is called thermal conduction.<sup>15</sup> The local conductive heat flux density  $\mathbf{q}_{\text{cond}}$  can be described by Fourier's law<sup>16</sup>

$$\mathbf{q}_{\text{cond}} = -\kappa \nabla T, \quad (2.2)$$

where  $\kappa$  is the thermal conductivity of the material and  $\nabla T$  is the temperature gradient. The heat flux density  $\mathbf{q}_{\text{cond}}$  is the amount of energy flowing through a defined unit area per unit time. The conductivity is often treated as a constant, which is only true for isotropic solids. In solids, thermal energy, also referred to as heat, is dissipated through vibrations and collisions of molecules, the propagation of phonons or free electrons. Generally, pure metals have the highest thermal conductivity. In liquids and gases, the collision and diffusion of molecules dominates thermal conduction. In all cases the thermal conductivity is dependent on temperature and for metals usually decreases with increasing temperature, while it is the other way around for gases.<sup>15</sup> Figure 2.1 illustrates this form of heat transfer within a solid schematically.

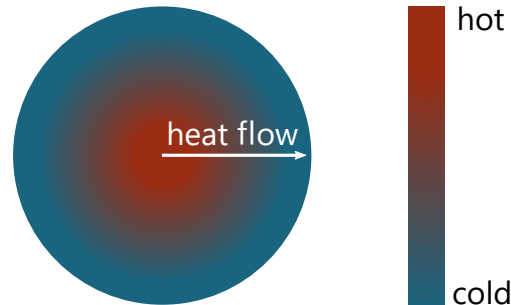


**Figure 2.1: Thermal conduction illustrated schematically.** When a temperature gradient is present within a solid, the direction of thermal energy flow is from hot to cold.

## Convection

Thermal energy transfer via a transport medium, such as a liquid or gas, is referred to as convection. This heat transfer mechanism is most commonly encountered at surfaces between solid materials and air, but it also occurs for solids placed in liquids. Material properties of a body and its surrounding medium such as density, pressure, thermal conductivity and specific heat influence the energy transfer via convection. Compared to conduction, the energy transfer takes place at the interface of a body and the surrounding medium and not within the body.<sup>17</sup> Equation 2.3 mathematically describes the thermal energy transferred per unit time  $\dot{Q}_{\text{conv}}$  between a body and a surrounding fluid

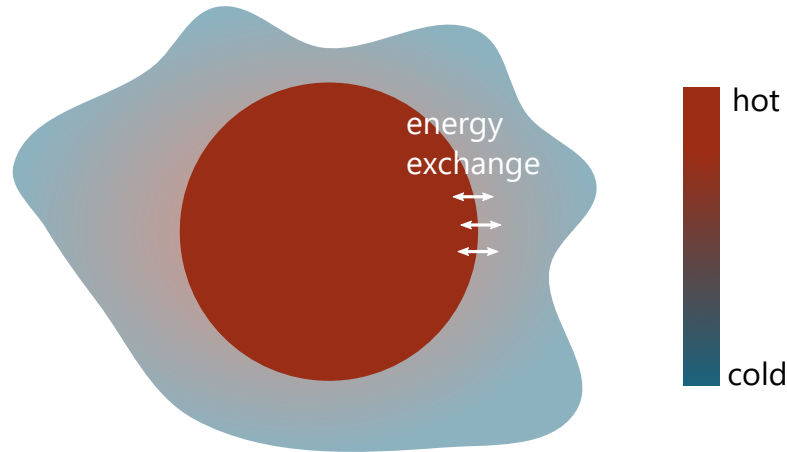


**Figure 2.2: Convection illustrated schematically.** This form of energy exchange takes place at the interface between a solid and the surrounding air or liquid. The air closer to the hot solid will be warmer than the air further away.

$$\dot{Q}_{\text{conv}} = hA(T_{\text{solid}} - T_{\text{liquid}})^n, \quad (2.3)$$

where  $h$  is the heat transfer coefficient,  $A$  is the surface area of the body and  $n$  is the aforementioned power with  $1 < n < 2$ .<sup>18</sup> A schematic illustration of this process is provided in [Figure 2.2](#). In contrast to the above described conduction process, here, the energy transport takes place by the actual movement of individual particles.

## Radiation

While conduction and convection require lattice vibrations and ballistic effects to transfer thermal energy, the only way to transport thermal energy through a vacuum is via radiation. Thermal radiation is an electromagnetic wave that is caused by spontaneous energy fluctuations in quantized energetic levels. The average magnitude of the fluctuation is called temperature. In contrast to conduction and convection, two bodies exchanging energy via radiation do not require a medium between them. A schematic of this exchange is shown in [Figure 2.3](#) and in this picture it is assumed that the bodies are located inside a perfect vacuum.

We consider a volume element  $dV_1$  and a surface element  $dA_1$  on the first body, which is the hot one in this case. Those elements are thermally radiating onto the distant surface section  $dA_2$  on the second body. In this picture the finite volume element  $dV_1$  has a constant absolute value of the energy flux  $q_V$  and the surface element  $dA_1$  has the respective value  $q_A$ . Then  $q_V \cdot dV_1 + q_A \cdot dA_1$  is the total power arriving on the surface section  $dA_2$  of the second body.<sup>13</sup>

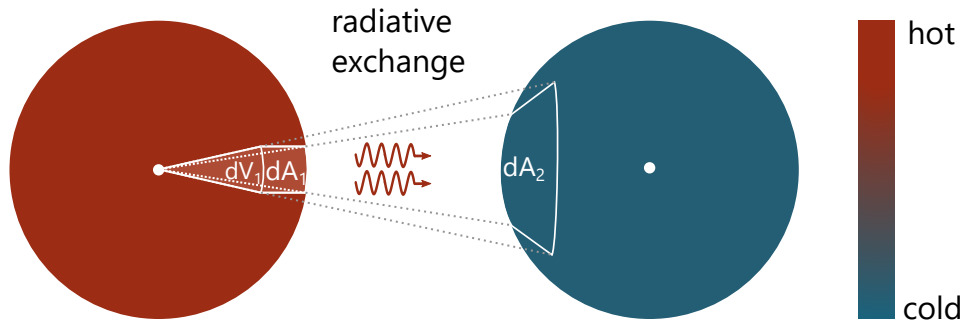


**Figure 2.3: Thermal radiation illustrated schematically.** This form of energy exchange does not require a medium between the bodies. The thermal radiation originating from the volume element  $dV_1$  and the surface element  $dA_1$  of the hot body arrives at the surface element  $dA_2$  of the cold body.

When calculating the total radiative power  $P_{\text{rad},2}$  arriving on the second body, it is necessary to consider the contribution of every surface and volume element emitting in the direction of body 2. This can be expressed as

$$P_{\text{rad},2} = \int_A q_A dA_1 + \int_V q_V dV_1. \quad (2.4)$$

Usually, thermal radiation originating from inside a body would not reach the surface. Therefore, thermal radiation is mostly considered to be emitted from the surface. This convention is also adopted in this thesis.

Above, a perfect vacuum was assumed between both bodies. In reality, this is not necessarily the case and especially not in this work. The medium between the two bodies influences the efficiency of the radiative exchange, since radiation can be absorbed or scattered. Thus, when quantifying the total energy transferred via the radiative pathway, the spectral dependence must be considered.<sup>13</sup>

### Impact of the View Factor

Radiative energy transfer occurs between objects that “see” each other. For this exchange, a certain surface area to emit from and to absorb by are essential. The so-called view factor is the measure of the solid angle via which a body can radiatively exchange energy with a second body. As thermal radiation is omni-directional, it is best to describe it in spherical coordinates.

For comparison in [Figure 2.4](#), a surface element  $dA$  is shown in Cartesian as well as spherical coordinates. In [Figure 2.4 a](#), a solid angle originating from the central origin  $O$  is projected onto the half-sphere with radius  $r$  on which the surface element  $dA$  is highlighted. In [Figure 2.4 b](#), spherical coordinates are introduced to show the projection of such a surface

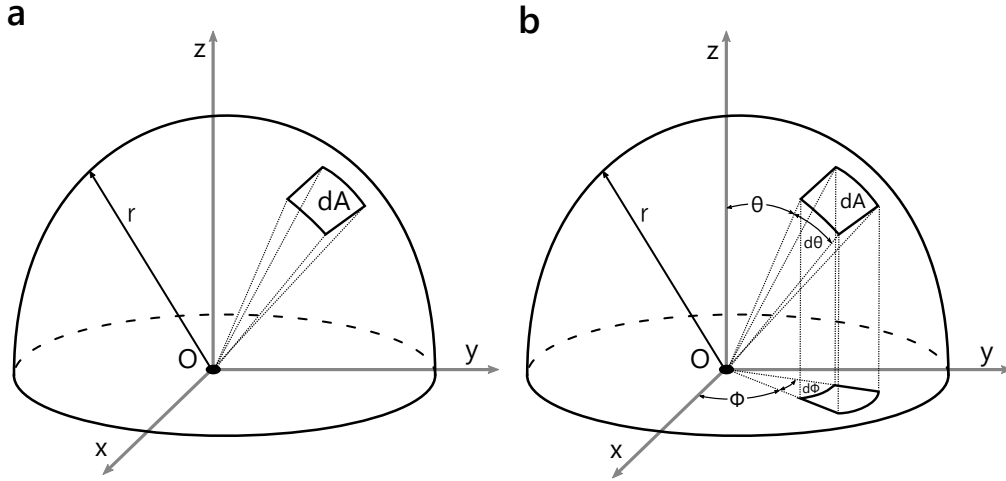


**Figure 2.4: View factor in Cartesian and spherical coordinates.** (a) The view factor of a point of origin  $O$  in a Cartesian coordinate system is drawn.  $dA$  describes a surface element. (b) Transforming  $dA$  into a spherical coordinate system highlights the relation between both systems. [Adapted from Reference [13]].

element  $dA$  onto the  $xy$ -plane in the Cartesian coordinate system. The zenith angle  $\theta$  and the azimuthal angle  $\phi$  describe the axes in this system, where  $\theta$  is measured between the  $z$ -axis and the direction normal to  $dA$ . The sides of the surface element  $dA$  can be rewritten as  $r d\theta$  along the  $\theta$  direction and  $r \sin \theta d\phi$  along the  $\phi$  direction. The solid angle element  $d\Omega$  can therefore be given by

$$d\Omega = \frac{dA}{r^2} = \frac{r d\theta r \sin \theta d\phi}{r^2} = \sin \theta d\theta d\phi. \quad (2.5)$$

As a reminder for spherical coordinate systems, when integrating  $d\Omega$  over the entire hemispherical domain, the complete hemisphere is given by

$$\int_{\cap} d\Omega = \int_{\theta=0}^{\pi/2} d\theta \int_{\phi=0}^{2\pi} d\phi \sin \theta = 2\pi, \quad (2.6)$$

resulting in the maximal solid angle  $2\pi$  for a half-sphere. Half-spheres are commonly considered when quantifying the thermal radiation between two bodies, since this is the maximum surface area that any point on a surface of either body can perceive for radiative energy exchange. Generally, the view factor is an essential measure when quantifying radiative heat exchange. Calculating it for non-uniform radiation or shapes is an analytical problem that requires extensive calculation power,<sup>19–23</sup> however, in this work we consider the common approach with uniform radiation in all directions.

## Newton's Law of Cooling

Isaac Newton described the process of cooling of a body already in 1701.<sup>24,25</sup> He introduced a temperature scale and observed that the temperature difference between a warm body and its cooler surrounding environment decreases over time.<sup>24</sup> Interestingly, he did not include mathematical formulae in his original publication. He simply described his findings for the body's temperature change over time  $T_{\text{body}}(t)$ , which in retrospect can be expressed mathematically as<sup>26</sup>

$$T_{\text{body}}(t) = T_{\text{env}} + (T_{\text{body}}(t = 0) - T_{\text{env}})e^{-t/\tau}. \quad (2.7)$$

Here,  $T_{\text{env}}$  is the temperature of the surrounding environment and can be considered constant.  $T_{\text{body}}(t = 0)$  is the initial temperature of the body and  $\tau$  is the coefficient of heat transfer. More recently, it has been discussed that Newton's law of cooling accurately describes cooling via the conductive and convective pathways, however, the radiative pathway is not sufficiently considered by this law. Vollmer *et al.*<sup>27</sup> provide a computational analysis of Newton's law of cooling and quantify the deviation for large  $\Delta T = T_{\text{body}}(t = 0) - T_{\text{env}}$  and for materials involving a high contribution of the radiative component.

### 2.1.2 Black Body Radiation

The basic principles and assumptions behind black body emitters are discussed next. The gedankenexperiment of an ideal black body is elaborated and the laws of Max Planck, Wilhelm Wien, Josef Stefan and Ludwig Boltzmann, which govern its thermal radiative properties, will be set into context.

#### Ideal Black Bodies

A black body is a theoretical concept of an idealized body, postulated by Gustav Kirchhoff in 1860,<sup>13</sup> which absorbs all radiation incident on it. It does not reflect any electromagnetic radiation and is completely black to the observer. Therefore, its ability to absorb thermal radiation reaches the maximum possible value,  $\alpha = 1$ . Absorptivity is explained in detail in [Subsection 2.1.3](#). Efforts are made to construct near-perfect black bodies. For example "Vertically Aligned Nanotube Array (Vanta) Black" surfaces are commercially available since a few years and possess an absorptivity of 0.9996. They consist of a forest of carbon nanotubes that makes it nearly impossible for any incident light to be reflected and thus to escape.<sup>28</sup> Recently, a team at the Massachusetts Institute of Technology even managed to achieve an

absorptivity of 0.99996 and, therefore, surpassed the absorptivity of commercial Vanta Black by an order of magnitude.<sup>29</sup>

### Planck's Law of Black Body Radiation

When it comes to the emission of black bodies, Planck's law has to be considered. Max Planck aimed to achieve a more profound mathematical framework explaining thermal radiation and investigated the spectral dependence of thermal emission.<sup>30</sup> His law formulates how a black body's temperature  $T$  influences the emission spectrum of the very same body. The spectral density distribution  $I_{\text{BB}}(T, \lambda)$  of this emission is given by

$$I_{\text{BB}}(T, \lambda) = \frac{2hc_0^2}{\lambda^5} \frac{1}{\exp\left(\frac{hc_0}{\lambda k_{\text{B}}T}\right) - 1} d\lambda d\Omega, \quad (2.8)$$

where  $h$  denotes the Planck constant,  $c_0$  is the speed of light in vacuum,  $k_{\text{B}}$  the Boltzmann constant and  $\lambda$  the emission wavelength.<sup>13</sup>

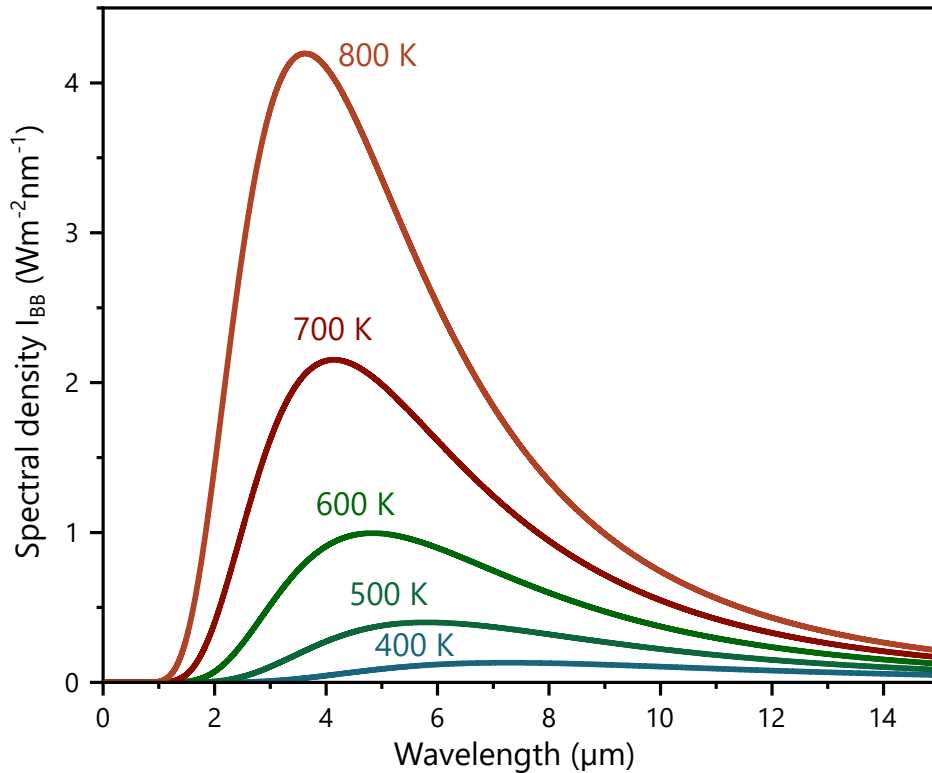


**Figure 2.5: Spectra for different temperatures according to Planck's law.** Exemplary Planck spectra for temperatures  $T$  of 400 K, 500 K, 600 K, 700 K and 800 K.

Figure 2.5 shows examples of such spectral density distributions for different temperatures. With increasing temperature, a blue-shift of the maximum emission wavelength is observed.

Higher temperatures allow for the population of energetically higher states, which explains this blue-shift of the spectra. Moreover, the probability for radiative transitions to occur also increases, causing the rise in the total spectral density.

### Wien's Displacement Law

Wilhelm Wien's displacement law relates the wavelength of maximum intensity  $\lambda_{\max}$  of the black body emission spectra as shown in [Figure 2.5](#) to the black body's emission temperature  $T$ . These physical quantities are inversely proportional, so their product is a constant<sup>31</sup>

$$\lambda_{\max} \cdot T = 2897.7729 \mu\text{m} \cdot \text{K}. \quad (2.9)$$

This relation had been proposed by Wilhelm Wien already in 1893, even before Max Planck published his work on thermal radiation distributions (1901).<sup>30,31</sup>

### Stefan-Boltzmann Law and Total Emitted Power

It is of interest to calculate the total emitted power  $P$ . To achieve this, for a given temperature  $T$ , the black body's spectral density distribution  $I_{\text{BB}}$  given by [Equation 2.8](#) is integrated over a half-sphere and all wavelengths. This results in the Stefan-Boltzmann law<sup>32,33</sup>

$$P = \sigma \cdot \epsilon \cdot A \cdot T^4, \quad (2.10)$$

where  $\epsilon$  is the emissivity,  $A$  is the surface area of the emitter and  $\sigma$  is the Stefan-Boltzmann constant which is given by

$$\sigma = \frac{2\pi^5 k_{\text{B}}^4}{15h^3 c_0^2}. \quad (2.11)$$

[Equation 2.10](#) shows that the total emitted power via thermal radiation depends on  $T^4$ . Hence in this case, the correlation between temperature and energy transfer is much stronger as for conduction or convection (cf. [Equation 2.2](#) and [Equation 2.3](#), respectively).

At this point the above mentioned absorptivity  $\alpha$  and emissivity  $\epsilon$  are the last properties that need to be discussed to fully describe and quantify the radiative exchange between bodies.

### 2.1.3 Absorptivity and Emissivity

Fundamental pillars of thermal radiation – namely the absorptivity and the emissivity of bodies – are introduced next. Their relation to each other in form of Kirchhoff's law concludes the discussion of the basic physical concepts behind thermal radiation.

#### Absorptivity $\alpha$

A body can absorb the energy carried by incident radiation. Thereby, the body's internal energy increases. Quantitatively, the absorptivity is the absorbed fraction of the incident energy. The temperature  $T$  of the absorbing body's surface has to be considered along with the spectral and directional characteristics of the absorbed radiation. In mathematical terms, the absorptivity is given by<sup>13</sup>

$$\alpha(\lambda, \theta, \phi, T) = \frac{I_{\text{absorbed}}(\lambda, \theta, \phi, T) dA d\lambda \cos \theta d\Omega}{I_{\text{incident}}(\lambda, \theta, \phi, T) dA d\lambda \cos \theta d\Omega}. \quad (2.12)$$

Here,  $I_{\text{absorbed}}(\lambda, \theta, \phi, T)$  is the intensity of absorbed radiation and  $I_{\text{incident}}(\lambda, \theta, \phi, T)$  is the incident radiation. It is presented in a differential form and it is necessary to integrate over the surface area, all wavelengths and the solid angle, as introduced in Equation 2.5, to obtain absolute values. Essentially, the ability of a body to absorb radiation is dependent on the incident radiation as well as the properties of the receiver. Other characteristics, such as the surface morphology, also impact absorptivity.<sup>34</sup>

#### Emissivity $\epsilon$

Now, we are considering a hot body that is emitting thermal energy through the radiative pathway. A body's effectiveness in emitting thermal energy in the form of radiation is quantified in the so-called emissivity. It is described by the amount of thermal energy emitted at a given temperature compared to the amount emitted by an ideal black body, at the same temperature. Therefore, it can be thought of as a measure of how much it resembles a black body in terms of thermal emission. Compared to ideal black bodies, for real bodies, the thermal radiation is not necessarily uniform in all directions. Considering the dependencies, the directional spectral emissivity is given by<sup>13</sup>

$$\epsilon(\lambda, \theta, \phi, T) = \frac{I(\lambda, \theta, \phi, T) dA d\lambda \cos \theta d\Omega}{I_{\text{BB}}(\lambda, T) dA d\lambda \cos \theta d\Omega}. \quad (2.13)$$

This describes the ratio of the intensity emitted normal to the direction  $(\theta, \phi)$  for a projected area element  $dA$  compared to the intensity emitted of a black body at the same temperature.



Despite the dependencies indicated in Equation 2.13, often only averaged emissivity data is available for different materials.

It is difficult to generalize which materials present high or low emissivities. Examples of good emitters are generally surfaces with a rough, grainy texture,<sup>35</sup> such as charcoal or polypropylene. Exemplary emissivity values are given in Figure 2.6. Due to the naming of a black body, it would be intuitive that darker materials would emit better. However, this is not necessarily true as the visible spectrum only represents a small fraction of the wavelength range in which a material can emit thermal radiation. For temperatures common on Earth, most thermal radiation actually takes place in the infrared, as predicted by Planck's law (Equation 2.8). Snow, for example has a high total emissivity, as well as water or wood. Oil paint falls into a similar category, independent of the apparent color. However, one generalization that can be made is that dielectric materials have a tendency for higher emissivity values than metals, unless the metals are strongly oxidized.<sup>13</sup>

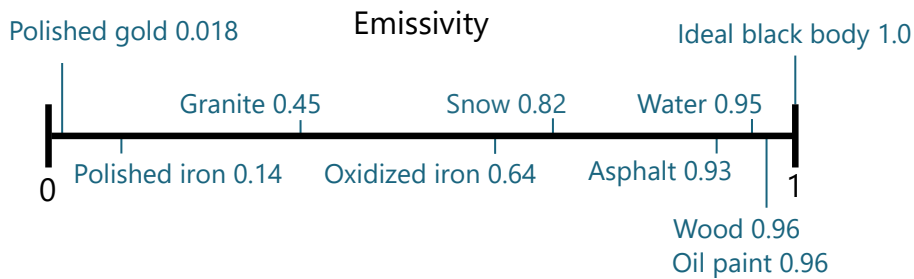


**Figure 2.6: Total emissivities of selected materials.** Metals as well as dielectrics occurring in nature are chosen to illustrate the spectrum of emissivities. The values are obtained from Reference [13].

### Kirchhoff's Law

Gustav Kirchhoff investigated the relation of absorptivity and emissivity in 1859 and came to the conclusion that, since black body radiation is always independent of direction, the absorptivity and the emissivity for any given direction must be equal<sup>36</sup>

$$\epsilon(\lambda, \theta, \phi, T) = \alpha(\lambda, \theta, \phi, T). \quad (2.14)$$

This equation is valid as long as the incident radiation is independent of the direction and has the spectral distribution of a black body.<sup>37</sup> Therefore, bodies that absorb thermal radiation well will also emit it well, at least in the identical direction.

For averaged values of absorptivity or emissivity, this is not necessarily true. Often, as part of the averaging process, the value for absorptivity is weighted for the solar spectrum, while, as mentioned above, most thermal radiation emitted at typical temperatures on Earth lies

in the infrared range. Thus, average emissivity values are often much higher than average absorptivity values.

#### 2.1.4 Applications of Radiative Cooling: From the Universe to the Laboratory

Since the general pathways of thermal energy transfer and relevant theoretical concepts have been covered now, radiative cooling and especially its potential factual applications can be mapped out. Only in recent years, a new field of research concerning experimental radiative cooling has opened up since the breakthrough publication by the Fan group in Stanford.<sup>5</sup> In such research, bodies are cooled down by “harvesting the cold of the universe”.<sup>38</sup>

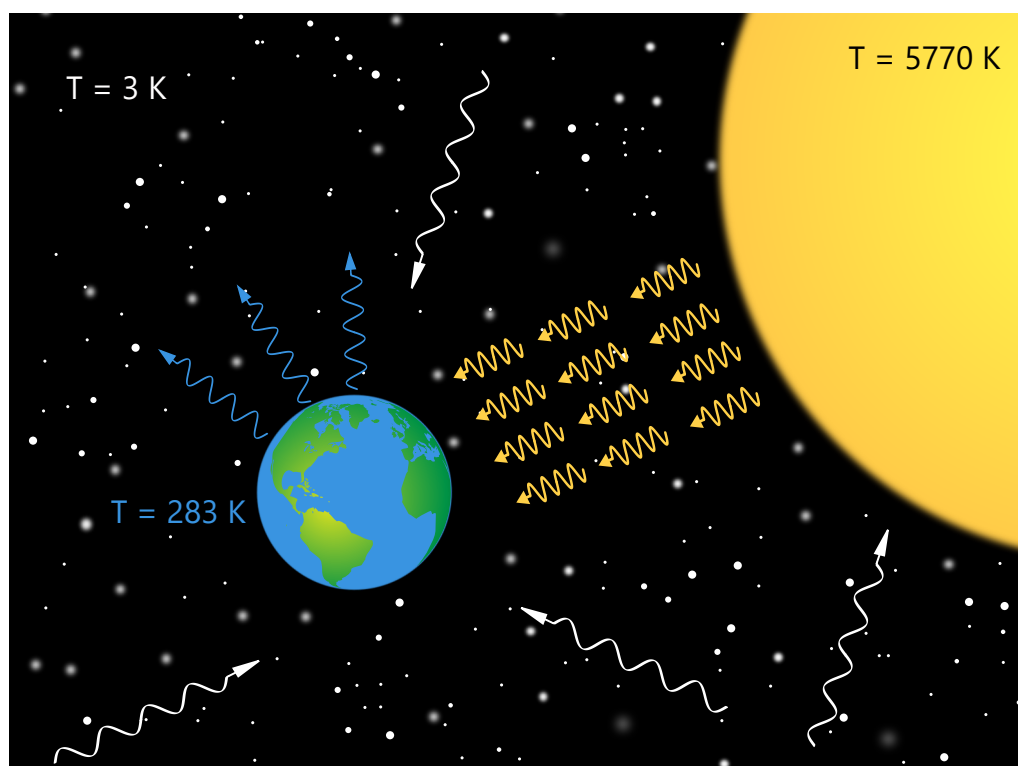


**Figure 2.7: Radiative thermal exchange between the Sun, the Earth and the universe.** Radiation emitted from Earth (blue) can be absorbed by the cold universe. The Sun constantly emits radiation (yellow) onto Earth and thereby decreases its internal energy. The universe emits thermal radiation in all directions (white) but with much lower intensity. The temperature values refer to the surfaces of the bodies, since thermal radiation is emitted there.

The basic concept involves using thermal radiation to take away energy and entropy from Earth.<sup>39</sup> The general principle of this and the roles of the Sun, the Earth and the cold universe are depicted in [Figure 2.7](#). The intensity of the radiation is indicated schematically by the number of arrows and the emission wavelength is indicated by the periodicity of the wavy arrows according to Wien’s displacement law ([Equation 2.9](#)), but not drawn to scale. The universe itself is extremely cold, at a temperature of approximately  $3\text{ K}$ .<sup>40</sup> The origin of this temperature value is highly investigated and thought to be remaining energy of the big

bang.<sup>41</sup> Due to the low temperature of the universe, the radiation incident on Earth from space is virtually non-existent. The black body emission spectra, according to Planck's law (Equation 2.8) for the Sun, the Earth and the cold universe are plotted in Figure 2.8. Earth with an average surface temperature of most recently 283 K (this value has significantly increased in the past century, as shown by Rohde *et al.*<sup>42</sup>) emits black body radiation mainly in the infrared region with a  $\lambda_{\max} = 10.24 \mu\text{m}$ .

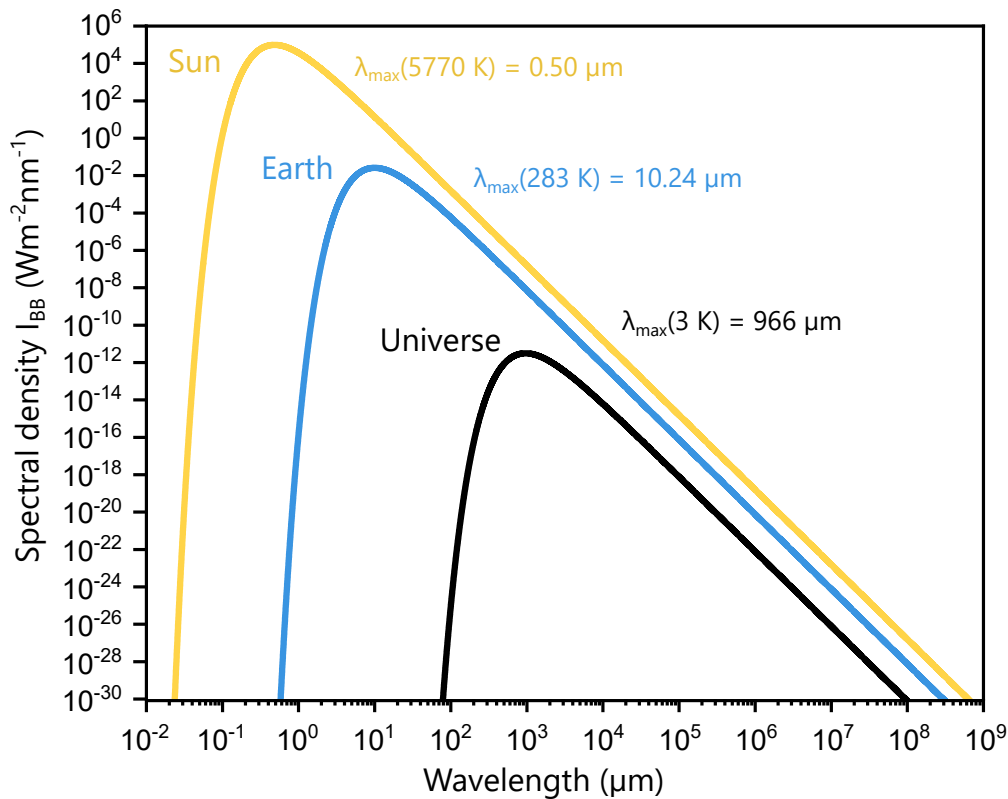


**Figure 2.8: Planck spectra of the Sun, the Earth and the universe.** The emission spectra have been calculated using Equation 2.8 for the Sun at  $T = 5770 \text{ K}$ , the Earth at  $T = 283 \text{ K}$  and the cold universe at  $T = 3 \text{ K}$ . The wavelengths of maximum emission  $\lambda_{\max}$  are also presented according to Equation 2.9. Both axes are logarithmic.

The Sun at a surface temperature of approximately  $5770 \text{ K}$ <sup>43</sup> is the main source of radiative energy incident on Earth, due to its proximity and radiation intensity. Its core temperature is much higher, at approximately  $1.5 \cdot 10^7 \text{ K}$ .<sup>44</sup> Compared to the Sun, other stars play a minor role and can be neglected in this model. Due to its high surface temperature, the Sun emits radiation with a maximum of about  $10^5 \text{ W m}^{-2} \text{ nm}^{-1}$  while the Earth's peak emission is at around  $10^{-2} \text{ W m}^{-2} \text{ nm}^{-1}$  and the cold universe can virtually be neglected at  $10^{-12} \text{ W m}^{-2} \text{ nm}^{-1}$ . This is a significant difference in order of magnitude from Sun to Earth of 7 orders and then again from Earth to the universe of 10 orders of magnitude. It becomes evident how the Sun dominates thermal emission in this system while the universe

hardly emits any radiation onto Earth and can therefore be considered as a cold reservoir for radiative cooling.

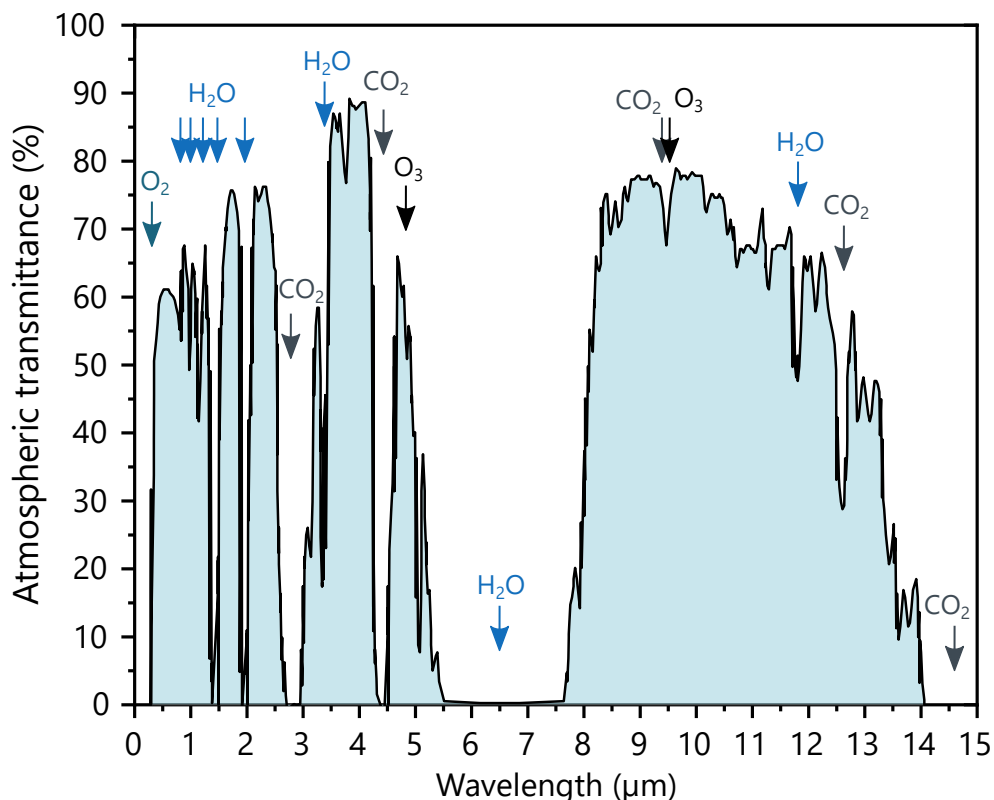


**Figure 2.9: Transmittance of the Earth's atmosphere.** The molecules responsible for specific transmittance drops are highlighted with arrows indicating the respective spectral position. [Adapted from Reference [45]].

For a more realistic picture, the influence of Earth's atmosphere has to be taken into account. Both, the efficiencies of radiation of the Sun onto the Earth and of the Earth into the universe are highly dependent on the selective spectral properties of the atmosphere. The atmospheric transmittance is highly dependent on the wavelength of the radiation (see Figure 2.9). Up to 5  $\mu\text{m}$ , sharp minima can be seen mainly due to absorbance of the vibrational modes of  $\text{H}_2\text{O}$  (combinations of symmetric and asymmetric stretching and bending)<sup>46</sup> and  $\text{CO}_2$  (asymmetric stretching for absorption at 4.26  $\mu\text{m}$  and symmetric vibration modes).<sup>47</sup> Only modes leading to dipole changes can absorb infrared radiation. From 5.5 to 7.5  $\mu\text{m}$ ,  $\text{H}_2\text{O}$  absorbs nearly all radiation and the atmosphere is not transparent at all. In the range of 8 to 13  $\mu\text{m}$ , however, a relatively continuous transmittance of roughly 70 % is measured. This range is therefore often referred to as the "atmospheric window".<sup>48</sup> For longer wavelengths above 14  $\mu\text{m}$  and up to roughly 100  $\mu\text{m}$  the atmosphere is nearly opaque.<sup>49</sup>

Altering the atmospheric chemical composition, for example by burning fossil fuels or extensive usage of fertilizers, increases the absorption in the atmospheric window and therefore reduces the amount of thermal radiation exiting the atmosphere.<sup>50</sup> This is commonly

referred to as the Greenhouse Effect.<sup>51-54</sup> As mentioned above, most radiation emitted from Earth is in the infrared range and therefore Earth's cooling mechanism is compromised, leading to global warming.<sup>55-57</sup> Very close to the maximum of black body emission of Earth, a CO<sub>2</sub> mode absorbs energy. Thus, increased CO<sub>2</sub> emission effectively further diminishes the atmospheric window.

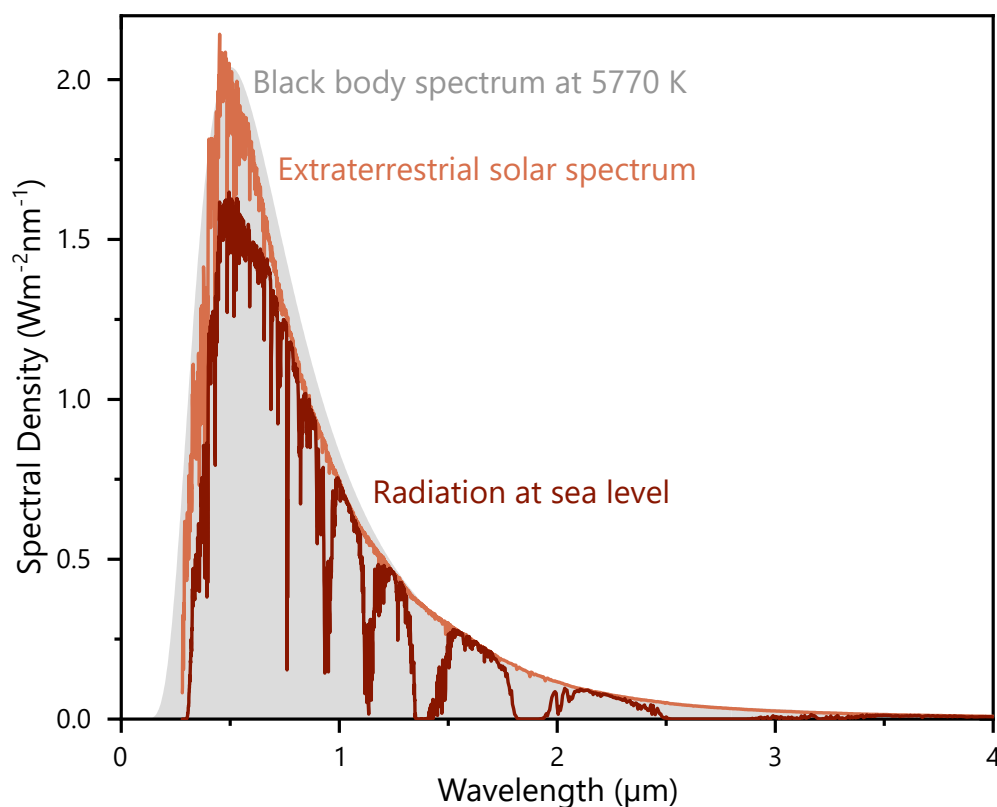


**Figure 2.10: Solar spectrum above and below the Earth's atmosphere.** The solar radiation is measured above (orange) and below (dark red) Earth's atmosphere. A black body spectrum for a body at  $T = 5770$  K is plotted to approximate the emission spectrum of the Sun. The data above the atmosphere is measured by satellites, space shuttles or high-altitude aircraft. [Data retrieved from Reference [58]].

The solar spectrum is shown in Figure 2.10. Solar radiation is measured above the atmosphere using satellites, space shuttles or high-altitude aircraft and is shown in orange while radiation measured below the atmosphere at sea level is presented in dark red.<sup>58</sup> The spectrum of a black body with  $T = 5770$  K is provided in light gray. Firstly, the conformity of the extraterrestrial solar spectrum with Planck's law of radiation can be seen. The Sun can be approximated as a black body and from this the temperature of the surface of the Sun at 5770 K has been retrieved. The surface temperature of multiple stars has been obtained by this method.<sup>59</sup> Secondly, the impact of the atmosphere on the solar spectrum at sea level becomes evident. Strong minima indicate the absorption bands of the molecules, as described and depicted in Figure 2.9.

As introduced above, the field of passive radiative cooling uses the natural thermal emission of a body on Earth and the cold universe to absorb this radiation in order to achieve a net cooling effect. This is particularly interesting, as due to global warming the demand for cooling systems is projected to increase by 72 % until 2100.<sup>60</sup> Additionally, models predict that heat waves will occur more often, last longer and be hotter in the second half of the 21<sup>st</sup> century.<sup>3</sup> With such prospects the urge for developing alternative cooling methods with low demand for energy is absolutely evident.

Generally, the idea to use the natural thermal emission to cool down an object on Earth against the cold universe,<sup>48,61,62</sup> has been investigated theoretically<sup>63,64</sup> and even with first attempts for experimental realization<sup>65,66</sup> for several decades, however, these approaches were not efficient yet. The practical challenge lies in the need to have a material with a highly selective emissivity within the atmospheric window between 8 to 13  $\mu\text{m}$ .<sup>67</sup> Simultaneously, it is crucial for the material to have a high reflectance below this window, specifically to reflect incoming sunlight for daytime application.

Looking firstly at the selective emission, several photonic surfaces have been engineered theoretically and experimentally and became very efficient within the last decades. Implementations include photonic band gap materials,<sup>68</sup> photonic crystals with altered thermal emission,<sup>69</sup> coherent thermal emission,<sup>70</sup> thermal antennas,<sup>71</sup> using infrared metamaterials for selective emission<sup>72</sup> and general broadband emitters.<sup>73–75</sup> Nanophotonic structures or metamaterials are ideal for such applications as the particle size is crucial for its interaction with light. For example, dielectric particles have the ability to resonantly scatter light if the particle size is adjusted to the radiation wavelength.<sup>39,76</sup>

Now combining these emissive properties with the requirement of high reflectivity within the solar spectrum, the field of radiative cooling during the day and night has emerged. Several groups have investigated numerous approaches to meet the above mentioned requirements, including integrated photonic solar reflectors consisting of  $\text{HfO}_2$ ,<sup>5</sup> silica photonic crystals,<sup>77</sup> polydimethylsiloxane (PDMS) with underlying gold,<sup>78</sup> random glass-polymer structures,<sup>79</sup> porous polymer coatings<sup>80</sup> and many more materials. With this, it has been shown that it is possible to achieve incredible cooling powers of  $>100 \text{ W m}^{-2}$  allowing cooling down to a record low of 42 °C below ambient temperature ( $\approx 20 \text{ °C}$ ) under vacuum conditions during the daytime.<sup>6</sup> Also, since it is desirable to use such cooling methods on a large scale, several groups have more recently attempted to commercialize this concept by utilizing low-cost materials such as paint as shown by Mandal *et al.*<sup>81</sup>

In most of the above mentioned works, these principles have been applied to maximize radiative cooling on extremely large scales. The most effective passive coolers are maintained within vacuum conditions to avoid reheating by thermal conduction and convection.<sup>6</sup> This,

---

however, poses a great limitation for practical implementation. Due to the dependence on the directionality of the radiation, emphasized in [Subsection 2.1.1](#), the question arises whether this directionality can be used to enhance the cooling effect, even outside of vacuum chambers. The possibility to direct and thereby focus thermal radiation for radiative cooling is investigated in [Chapter 3](#). For the research conducted in this thesis, radiative cooling is brought from the universe into the laboratory and studied under ambient conditions in detail.

## 2.2 Optical Temperature Sensing

Temperature influences radiation and thereby gives us the opportunity to measure temperature using radiation. This case is referred to as optical temperature sensing. Just as contactless temperature manipulation is of high interest, contactless measurement of temperature is equally important and enables contactless high precision measurements.

In contrast to conventional invasive temperature measurement options, an alternative approach leverages thermal radiation. While this has been commonly applied for many years in the field of astrophysical determination of star temperatures, the commercial application has sky-rocketed since the COVID-19 pandemic in 2020.<sup>82,83</sup> In laboratory as well as manufacturing contexts such temperature measurements have already been applied more commonly, mainly by using thermal cameras. A less explored option to measure temperatures independent of emissivities is given by optical interferometry. Since temperature can influence optical properties, using incoming light as a means of detection is possible.<sup>84–87</sup> A novel approach to high-precision interferometric temperature determination embodies the second project presented in this thesis. Therefore, interferometry basics are introduced next.

### 2.2.1 Interferometric Temperature Measurements

Interferometers offer a contactless sensing method by bringing multiple, usually two, beams of light into overlap and creating a specific interference pattern. In general, light is directed through a transmissive sample or reflected by a non-transmissive sample. Upon a change in temperature in the sample, the phase of the light is changed, altering the interference pattern. Essentially, the temperature of a sample may alter its optical parameters, which can be detected in an interferometer. When measuring in reflection, a sample's expansion can be measured.<sup>88</sup> When measuring in transmission, e.g., in liquid samples, the change in the refractive index of the medium can be observed.<sup>84</sup>

Optical thermometers based on interferometers have been reported.<sup>89–93</sup> However, interferometric approaches for high precision temperature sensing are limited to a handful of publications. Only recently, Zhao *et al.*<sup>86</sup> and Xia *et al.*<sup>87</sup> have designed an ultrasensitive temperature measurement setup based on an interferometer, reaching resolutions of 0.630 mK and 5 mK, respectively.

Interferometers come in many different shapes, the most applied ones being Michelson, Fabry-Perot and Mach-Zehnder interferometers, which all differ in the arrangement of the optical components. In this work, a Michelson interferometer is built and thus this section will focus on such a Michelson arrangement.



## 2.2.2 Michelson Interferometer

Albert Michelson and Edward Morley developed the idea of interfering light in the 1880s<sup>94</sup> and were awarded with the 1907 Nobel Prize in Physics.<sup>95</sup> Their method has developed over the past century to an extent that only recently enabled the detection of gravitational waves.<sup>96,97</sup> This also yielded the Nobel Prize in Physics in 2017.<sup>98</sup>

Various types of light sources can be applied in Michelson interferometry.<sup>94,99</sup> However, most commonly, laser light is used due to its monochromaticity, coherence and directionality, which are beneficial characteristics for interferometry applications.<sup>70</sup> Figure 2.11 depicts a basic Michelson interferometer. A single beam is divided by a beam splitter into two paths along the arms of the interferometer, the measurement arm and the reference arm. A sample is placed in the measurement arm which induces a phase shift for the light in the measurement arm relative to the reference arm. At the end of both arms end mirrors guide the beams back to the beam splitter, in which the beams are brought to interference. When both arms use Gaussian light modes, the result is a Newton's rings interference pattern, in which the rings propagate radially with phase changes induced in the measurement arm.

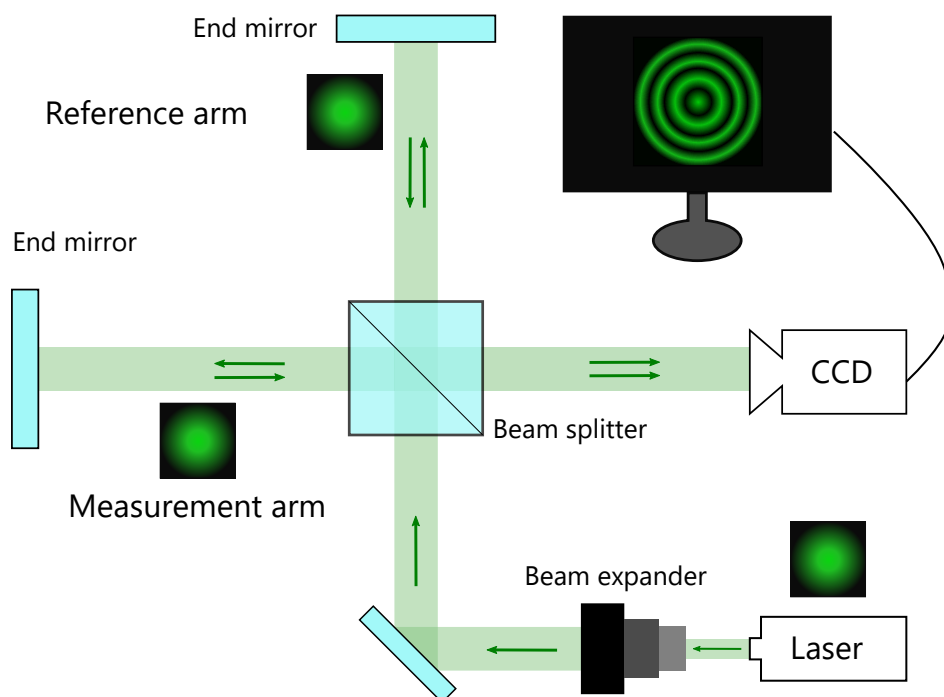


**Figure 2.11: Basic interferometer in a Michelson configuration.** A laser beam is first expanded, then directed onto a beam splitter, where it is divided into two equal beams. End mirrors reflect the beams back and the beam splitter brings them into interference. A CCD camera detects this signal and the resulting interference pattern is analyzed by a computer.

While the basic interferometer is limited in its resolution by the wavelength  $\lambda$  of the light source, many approaches overcome this limitation by far. Promising adaptations to standard Michelson interferometry are categorized into so-called homodyne and heterodyne setups. Homodyne interferometers work with a single frequency of light interfering with itself. One way to achieve a resolution below the diffraction limit is by using polarized light. The information is retrieved from a modulation of the phase of an oscillating signal, this modulation is then compared to the phase of the reference arm oscillation. This principle can be applied in combination with frequency combs<sup>100</sup> and exhibits picometer<sup>101–104</sup> or even sub-picometer<sup>105,106</sup> resolutions.

Generally speaking, heterodyne interferometers have received their name as light of different frequencies interferes in both arms. An acousto-optic modulator can realize such frequency-shifted beams originating from a single laser. This frequency shift then provides more accurate information in the interference pattern. Resulting analyses can be translated into tens of picometer<sup>107</sup> and low noise biological measurements<sup>108</sup> can be performed. A selection of further interferometers is presented in [References \[106, 109–112\]](#).

### 2.2.3 Light Modes

For several centuries, one of the major conflicts in natural sciences was the conceptualization of radiative energy flow – whether to consider it in wave form or in quantized particle form. Isaac Newton and Christiaan Huygens supported opposite points of view. Eventually, in 1865 James Clerk Maxwell provided a mathematical framework of 20 equations that connect both ideas. Later on, Oliver Heaviside simplified this into 4 equations, today known as the Maxwell equations.<sup>113</sup> Albert Einstein finally recognized the existence of light quanta in order to explain the photo-electrical effect which allowed Max Planck to then correctly interpret the spectral distribution of black body radiation. Finally, Louis de Broglie proved the equivalence of the two interpretations and coined the term *wave-particle dualism*.<sup>114</sup>

The Maxwell equations provide the basis for modern day electrodynamics and encompass the momentum and energy properties of light.<sup>115</sup> They set the foundation to mathematically derive Gaussian and Laguerre Gaussian (LG) light modes, the latter playing a crucial role in this work. From the Maxwell equations, the so-called wave equation can be derived, which is a partial differential equation describing the field propagation of electromagnetic waves.

The wave equation in its time-independent form is called the Helmholtz equation and is usually the starting point for the derivation of various light modes under the paraxial approximation.<sup>116–118</sup> A full mathematical derivation can be found for example in [References](#)

[119–121]. From the above described equations, it is possible to derive the most fundamental light mode – the Gaussian mode – as well as the LG mode.

## Gaussian Modes

Most commercial lasers operate in the Gaussian mode, which is also referred to as  $TEM_{00}$  (transverse electromagnetic) mode. This mode can be derived when considering the solution with minimal divergence and minimal transversal extension to the Helmholtz equation. When following the calculations performed in Reference [121], the electric field of the fundamental laser mode results in

$$\mathbf{E}(r, z) = E_0 \frac{w_0}{w(z)} \exp \left[ -i(kz + r^2 \left( \frac{1}{w^2(z)} + \frac{ik}{2R(z)} \right)) - \Psi(z) \right], \quad (2.15)$$

where  $r = \sqrt{x^2 + y^2}$  is the radial direction and  $z$  is the propagation direction.  $E_0$  is the amplitude of the electric field,  $w_0$  is the beam waist and  $w(z)$  is the radius at which the field amplitude has decreased to  $\frac{1}{e}$  compared to the center.  $k$  is the absolute value of the wave vector  $\mathbf{k}$ , which points in the direction of light propagation and  $k = \frac{\omega}{c_0} = \frac{2\pi}{\lambda}$ . For light waves in vacuum, this is parallel to the Poynting vector, which indicates the direction of energy flux.<sup>122</sup>  $R(z)$  is the radius of the curvature of the beam's wavefront and  $\Psi(z) = \arctan\left(\frac{z}{z_R}\right)$  is the so-called Gouy phase, attributable to the phase velocity of light.<sup>121</sup> From Equation 2.15 we can introduce the Rayleigh length  $z_R$

$$z_R = \frac{kw_0^2}{2} = \frac{\pi w_0^2}{\lambda}. \quad (2.16)$$

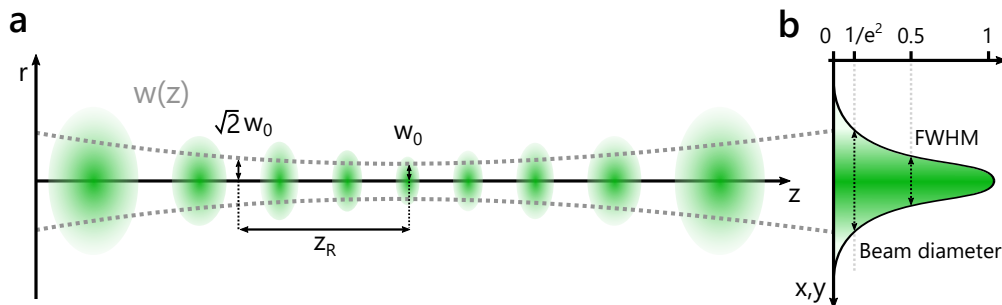


**Figure 2.12: Fundamental Gaussian mode.** The light beam has a transversal extension  $w(z)$  and propagates along the  $z$ -axis. **(a)** In the mode profile of a Gaussian beam  $w_0$  indicates the minimal beam waist while the distance to  $\sqrt{2}w_0$  is termed the Rayleigh length  $z_R$ . **(b)** The resulting intensity profile is Gaussian shaped. The diameter where the electric field intensity is decreased to  $\frac{1}{e^2}$  is coined the beam diameter. The FWHM is defined as the full width of the beam at half the maximum intensity.

The Rayleigh length is defined as the distance between the area at the waist of the beam to where the cross section of the area of the beam doubles<sup>120</sup> (see Figure 2.12 a). The corresponding light intensity  $I(r, z) = |\mathbf{E}(r, z)|^2$  has a Gaussian profile in the  $xy$ -plane, hence the naming of this light mode.<sup>120</sup> This is visualized in Figure 2.12 b. The beam diameter is defined as the width where the intensity  $I(r, z)$  of the electromagnetic field is reduced by  $\frac{1}{e^2}$  compared to the central maximum. The full width at half maximum (FWHM) is the width where the maximum intensity is halved.

### Laguerre Gaussian Modes and Optical Vortex Beams

In the breakthrough experimental work by Allen *et al.*<sup>123</sup> in 1992, optical vortices containing orbital angular momentum (OAM) were experimentally generated for the first time. The OAM each photon can contain corresponds to  $l\hbar$ ,<sup>115,123–125</sup> where  $l$  is an integer and the so-called topological charge of the beam.

Often, when such beams are introduced, confusion regarding circularly polarized light arises. While each photon carries  $\hbar\omega$  energy and  $\hbar k$  linear momentum, the spin angular momentum (SAM) is constrained to  $\hbar$ .<sup>126</sup> Aligning all spin angular momenta in a beam results in circular polarization. Circular polarized light can still propagate in Gaussian light modes.

When light with angular momentum interacts with a particle, this angular momentum can be transferred onto the particle for both SAM and OAM. In the case of SAM, the particle can be spun around its own axis. For OAM, the particle can revolve around the beam axis.<sup>127</sup> Figure 2.13 depicts this essential difference. In both cases the light propagates along the  $z$ -axis. The Poynting vector in circularly polarized light is still parallel to the  $z$ -axis, while in light containing OAM, it spirals around this beam axis.<sup>126</sup> It is possible to switch between beams containing SAM and OAM, or to combine them.<sup>128,129</sup>

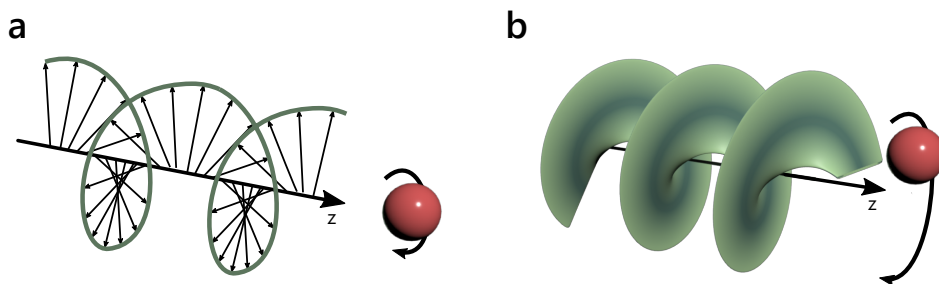


**Figure 2.13: Spin angular momentum and orbital angular momentum.** (a) In circularly polarized light, the photons pertain SAM. Upon interaction with a particle, it spins the particle around its own axis. (b) For light with OAM, the spatial distribution of the electromagnetic field rotates around the propagation axis. It can revolve a particle around the beam axis.

Generally, the orbital angular momentum arises from an off-axis effect of the linear momentum of light relative to the center of the optical beam.<sup>115</sup> Such OAM beams are a beautiful,

visible connection between classical and quantum physics. A Laguerre Gaussian mode is an example of a beam containing OAM and therefore resembling an optical vortex or helix and is used in this thesis. In literature, such beams are commonly referred to as LG, vortex or OAM beams. The OAM is a parameter of the LG beam. In this work, LG beam and OAM beam will be used interchangeably for the here described beam.

An OAM beam exhibits an azimuthal phase structure of  $\exp(-il\phi)$ , meaning the electric field of the resulting laser beam resembles a screw or Fusilli pasta. The wavelength  $\lambda$  describes the distance the electric field propagates along  $z$  during one full rotation of the beam around the azimuthal angle. For easier understanding, such a beam is visualized in [Figure 2.14 a](#) from the side and in [Figure 2.14 b](#) from the front.

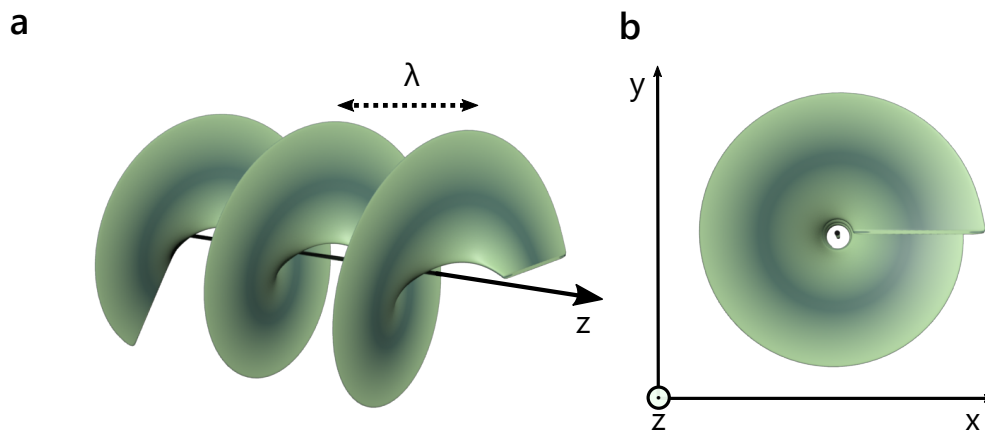


**Figure 2.14: Laguerre Gaussian mode.** (a) The LG mode containing orbital angular momentum resembles a screw propagating along the  $z$ -axis in the side view. The wavelength  $\lambda$  describes the distance the electric field propagates along  $z$  during one full rotation of the beam around the azimuthal angle. (b) In the frontal view the central minimum is visible.

Before diving into the mathematical definition and derivation, such vortices can be related to known phenomena. Vortices are common in fluid dynamics, for example in liquids or even in natural occurrences such as tornadoes or spiral galaxies, even present in the Milky way. Optical vortices can be imagined similarly. Additionally, likewise to fluid vortices, they exhibit a central minimum, which is also referred to as a singularity in its phase.<sup>130</sup> Analogies to a phase singularity can also be observed in nature, for example when considering the time on the North Pole. It describes the position where all time zones meet, therefore the time is undefined. Such a phase singularity is a perfect zero in intensity.<sup>115</sup> An example where similar beams with a central minimum first enabled super-resolution microscopy is in stimulated-emission-depletion (STED) microscopy.<sup>131,132</sup>

In order to derive the mathematical concept behind such beams, we will consider the equation derived for Gaussian beams in [Equation 2.15](#) and modulate the amplitude with a periodic

function  $\alpha = \arctan\left(\frac{k_x}{k_y}\right)$ . This work follows the derivation in Reference [120]. The electric field then exhibits an  $\exp(-il\phi)$  dependence, which is the so-called Hilbert factor.<sup>130</sup>

The angular variable is now given by  $\phi = \arctan\left(\frac{y}{x}\right)$ . The standard definition of an LG mode is given by

$$E_{l,p}(r, \phi, z) = \frac{e^{-il\phi}}{w(\zeta)} \left(\frac{r}{w(\zeta)}\right)^l L_p^l\left(\frac{2r^2}{w(\zeta)^2}\right) \exp\left[ikz - \frac{r^2}{w_0^2(1+i\zeta)} - i\psi_{l,p}^L\right]. \quad (2.17)$$

$L_p^l$  denotes the Laguerre functions, well known for example from the hydrogen model in quantum mechanics, where  $p$  and  $l$  are integers. In order to comprehend the notations, plotting the calculated mode profiles helps to understand the expressions introduced in Equation 2.17. The resulting intensity profiles in the  $xy$ -plane are shown for different  $p$  and  $l$  values in Figure 2.15.

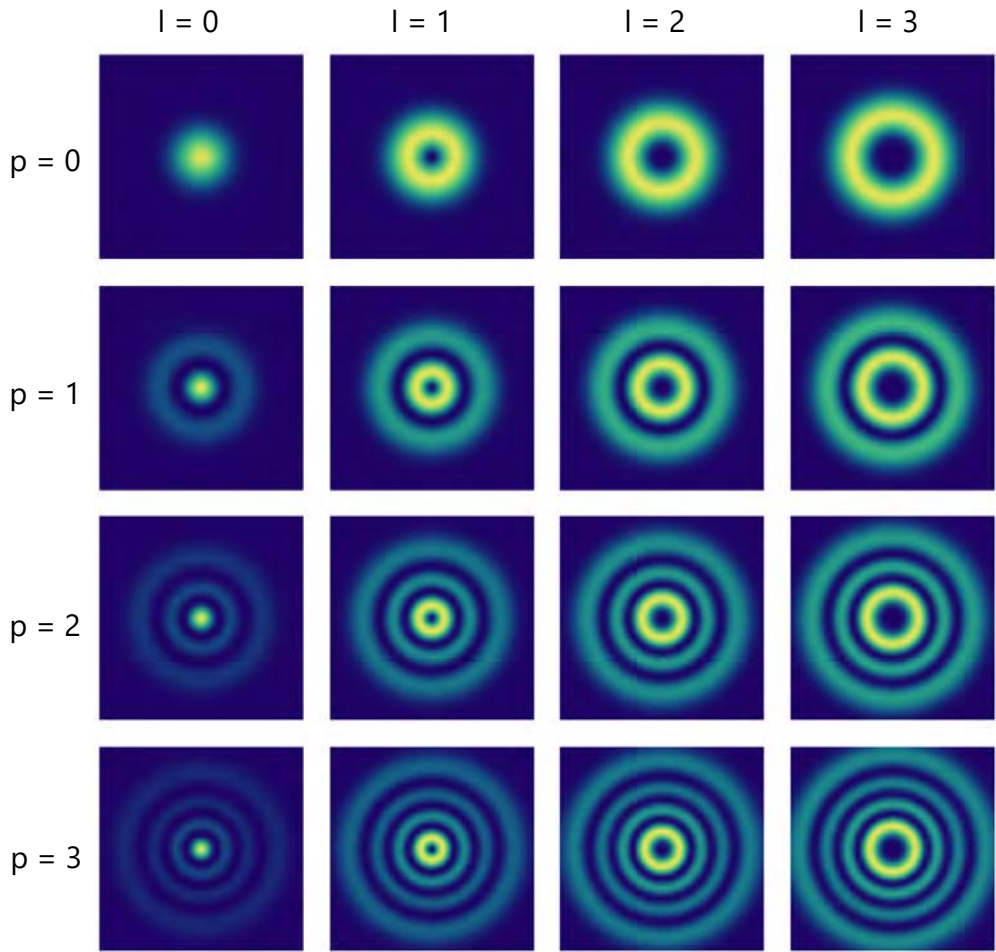


**Figure 2.15: Beam profiles of LG modes.** LG modes with various radial mode indices  $p$  and topological charges  $l$ . With increasing  $l$ , the diameter of the beam and of the central singularity also increase. The number of radial maxima is given by  $p + 1$ . [Adapted from Reference [133]].

The number of maxima radially present in an LG beam is given by  $p + 1$  and is referred to as the radial mode index.<sup>134</sup> The topological charge  $l$  on the other hand is commonly called the chirality of a beam and counts the number of full  $2\pi$  cycles of phase change in the beam when going  $360^\circ$  around the propagation axis  $z$  in a perpendicular plane. To put in other words, when “cutting” an LG beam, the number of electric field maxima in each cross section defines the topological charge  $l$ . For higher  $l$ , the beam diameter increases and the central minimum becomes larger. An LG beam with  $p = 0$  and  $l = 0$  is equivalent to the fundamental Gaussian mode. For better understanding, a 3D visualization of “cut” LG beams with different topological charges is included in Figure 2.16.

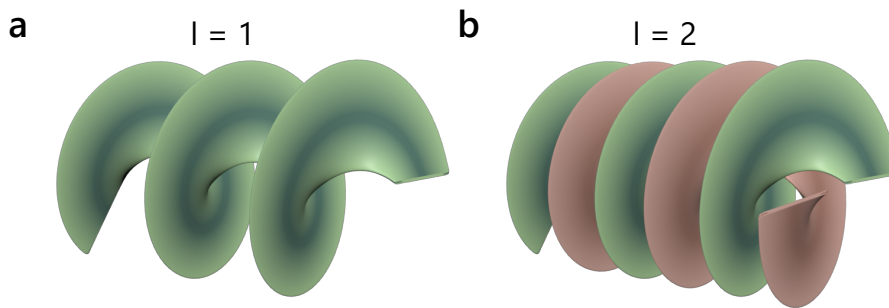


**Figure 2.16: LG modes with different topological charges.** LG modes with topological charges (a)  $l = 1$  and (b)  $l = 2$  are visualized in 3D. An LG mode with  $l = 2$ , can be considered as two intertwined  $l = 1$  modes.

Continuing the elaboration of Equation 2.17,  $r$  is used analogously as in the Gaussian beam derivation as a radial coordinate and defined by  $r = \sqrt{x^2 + y^2}$ . The beam center is therefore at  $r = 0$  and always in a minimum of intensity (for  $l \neq 0$ ).  $w(\zeta)$  defines the transversal expansion of the beam in terms of the reduced coordinate  $\zeta = \frac{z}{z_R}$ . Lastly, a new phase in terms of the Laguerre functions  $\psi_{l,p}^L(\zeta)$  was introduced and is defined as  $\psi_{l,p}^L(\zeta) = (l + 2p + 1) \arctan(\zeta)$ . At this point it is important to note that the topological charge  $l$  can also be negative. The physical meaning behind this is the definition of the turning direction of the spiral. They can rotate in either direction which is absolutely crucial for this work as discussed in depth in theory (Subsection 2.2.4) and experimentally (Subsection 4.1.3). Mathematically, the topological charge is given by the path integral<sup>130</sup>

$$l = \frac{1}{2\pi} \oint_C \nabla \phi(\mathbf{r}) dr. \quad (2.18)$$

$C$  is a small loop surrounding the singularity and  $\phi(\mathbf{r})$  the phase distribution. A more intuitive understanding can be obtained when considering a famous artwork, the Penrose staircase.<sup>135</sup> It shows connected stair cases going upwards while also being joined in the end, therefore resembling a loop. Such a structure is only possible in phase space but not in real space.<sup>130</sup> Essentially this means that the phase increases continuously from 0 to  $2\pi$  going in a circle

and when reaching  $2\pi$ , the phase is equal to 0 again and “jumps back” to 0. The topological charge  $l$  represents the number of such “phase jumps” occurring within one full rotation around the azimuthal angle. This is visualized in Figure 2.17 for topological charges  $l = 1$  and  $l = 2$ .

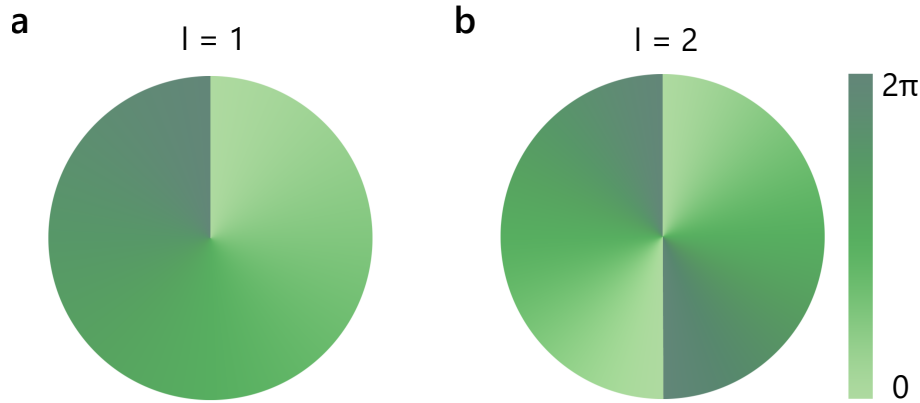


**Figure 2.17: The phase distribution in LG beams.** (a) The phase distribution ranges from 0 to  $2\pi$  and increases around the azimuthal angle over  $360^\circ$  for  $l = 1$ . (b) For  $l = 2$ , the phase increase from 0 to  $2\pi$  exists twice and each phase shifting section only spans  $180^\circ$ .

### Generation of OAM Beams

OAM beams have been experimentally investigated in the past 30 years,<sup>123,130</sup> with rapidly increasing interest. In order to generate OAM beams, the individual Gaussian pulses can be thought to be wrenched apart around the azimuthal angle, thereby generating the Fusilli shape. It is necessary to induce a phase shift from 0 to  $2\pi$  when going around the azimuthal angle once over one wavelength  $\lambda$  and to stitch individual wave fronts together perfectly.

One method for generating such OAM beams is by using a spiral phase plate (SPP).<sup>136–140</sup> Such a phase plate is used in this work and, therefore, elaborated in detail in Subsection 4.1.2. Other possible methods include using diffraction gratings,<sup>124,141</sup> q-plates<sup>142</sup> or spatial light modulators (SLMs).<sup>143–145</sup> SLMs consist of an array of liquid crystals of which the refractive index can be switched individually by applying an electric field. They can therefore be used for multiple beam shapes and are not specific for a topological charge or a certain wavelength, like SPPs are. Another faster and low cost option are digital micro-mirror devices (DMDs).<sup>146</sup> However, they do not possess the same conversion efficiencies as SLMs do. Placing diffractive elements, such as compensation prisms or additional gratings in the beam path, can even facilitate the generation of white-light optical vortices.<sup>147–149</sup> More recently, metasurfaces have been applied in order to generate and manipulate OAM beams of all shapes and colors.<sup>128,129,150–152</sup>



All of the above mentioned methods are based on mode conversion, usually starting at a Gaussian  $TEM_{00}$  mode. More recently, the bottom-up method of coherent beam combining (CBC), which is a widely applied technique,<sup>153–160</sup> was extended to OAM beams first theoretically<sup>161–165</sup> and later experimentally.<sup>166–168</sup> The great advantage this approach offers is the possibility for switchable, high power (kW range) output beams. However, the challenge lies within the phase purity as all combined beams need to result in a perfect helical wave front. To fulfill this requisition, artificial deep learning has been applied in order to generate OAM beams with completely eliminated phase noise.<sup>169–171</sup>

### Applications of OAM Beams

Several groups have engineered such beams in various ways finding applications in almost all fields of optics, ranging from imaging, optical communication to optical manipulation and quantum optics.<sup>115,172–177</sup> One of the first applications was in fact to combine such OAM beams with optical tweezers.<sup>178,179</sup> In these experiments the angular momentum was transferred to a trapped particle and it was orbited around the beam,<sup>180</sup> as depicted in Figure 2.13 b. In contrast, when spin angular momentum is transferred onto a particle in an optical trap, it begins to rotate around its own axis<sup>181</sup> (Figure 2.13 a). SAM and OAM have been combined in optical traps and cause particles to simultaneously rotate around their own axis as well as to orbit around the beam's axis.<sup>182</sup> Combining SAM and OAM beams can be achieved by combining multiple methods, for example waveplates and SLMs. The generated beams are then referred to as polarization vortices or vector vortex beams.<sup>130,183–186</sup> The principle of OAM was also extended to electron beams, which interestingly enough causes an induced magnetic field due to the azimuthal dependence of the Poynting vector<sup>187–189</sup> and may find interesting application for electron microscopy.<sup>190</sup> One of the most interesting applications of OAM beams can be found in quantum communication. OAM beams extend the toolbox for degrees of freedom in light beams by an infinite amount. When with polarized light only left- or right-handed circularly polarized light  $\pm\sigma$  was feasible, the possible combinations employing beams containing OAM are endless.<sup>191</sup> OAM beams with a topological charge of  $l = 10, 010$  have been generated for this purpose.<sup>192</sup>

### 2.2.4 Interfering OAM Beams

OAM beams also offer high potential in interferometric methods for measurement purposes.<sup>193–195</sup> The measurement of the rotational Doppler effect<sup>196</sup> and their application in gravitational wave detection<sup>197–200</sup> or the possibility to differentiate between elevations and depressions in an interferogram<sup>201,202</sup> are examples of OAM beams in interferometric configurations. Interfering two OAM beams with opposing helicity and identical topological

charge results in a distinct interference pattern and is discussed in References [125, 126, 203]. An example of such an interference pattern originating from two OAM beams with  $l = 6$  and  $l = -6$  is shown in Figure 2.18. The OAM beams for the individual paths of the interferometer are shown in the first two panels. Interference patterns created by OAM beams with opposing topological charge exhibit  $2l$  fringes, twelve in this case. For this approach, it is necessary to invert the helicity of one of the beams. This is described in detail in Subsection 4.1.3. A very obvious application of such interferometry using OAM beams is therefore simply the determination of the topological charge of the beam.<sup>204</sup>

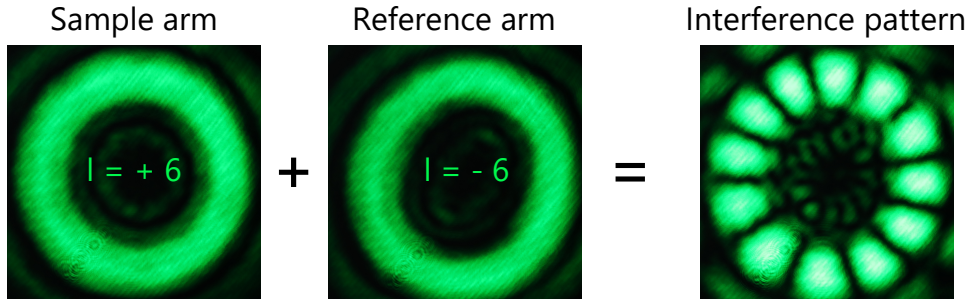


**Figure 2.18: Interference of two OAM beams with  $l = 6$  and  $l = -6$ .** When two OAM beams with opposing helicity are brought to interference, the result is such a daisy flower pattern.

As part of this work, a Michelson interferometer using OAM beams was built. When introducing a phase shift  $\Delta\Phi$  in one of the interferometer arms, an azimuthal rotation of the interference pattern can be observed. This rotation angle  $\Delta\theta_{\text{rot}}$  can be measured and expressed as<sup>133,233</sup>

$$\Delta\theta_{\text{rot}} = \frac{360^\circ}{2\pi l} \cdot \Delta\Phi = \underbrace{\frac{360^\circ}{l\lambda} \Delta d \cdot n}_{\text{reflection}} = \underbrace{\frac{360^\circ}{l\lambda} d \cdot \Delta n}_{\text{transmission}} \quad (2.19)$$

in which  $l$  is the aforementioned topological charge of the interfering beams. The shift  $\Delta\Phi$  can either be induced by a change in the optical path length or by changing the refractive index of the medium the beam is propagating through. Both of these options are considered separately.

The first case is considered in the part labeled “reflection” in the equation above. Here, the optical path length  $\Delta d$  is changed and the refractive index  $n$  is considered to be constant. An example of this case was published by Emile *et al.*<sup>205</sup> in 2017 where the displacement of an end mirror, i.e., changing  $\Delta d$ , led to an interference pattern rotation. They used a piezo stage to move the mirror in steps of 50 nm and proposed a resolution of just 44 pm when being able to detect a rotation of the interference pattern of  $0.25^\circ$ . This is a remarkable resolution, especially given the simplicity of the setup, not requiring any specific vacuum conditions

or signal post-processing methods. This principle can also be applied to achieve precise thickness measurements.

In the second scenario, the optical path length is constant and changes of the refractive index of the propagation medium  $\Delta n$  are considered. In Equation 2.19, this case is referred to as “transmission”. This has not yet been emphasized in literature but will be investigated in this work. Here, the beam passes through a transparent sample and the optical path through this medium  $d$  is kept constant. Therefore, changes in the rotation angle  $\theta_{\text{rot}}$  of the interference pattern can be explicitly attributed to changes of the refractive index  $\Delta n$ .

Advancing the application of OAM interferometry to perform contactless temperature measurements on fluid samples is the second core project of this work. For this, the dependence of the refractive index on temperature is employed. Furthermore, the concentration of solutions exhibits a refractive index dependence. The experimental implementation of OAM interferometry to measure temperature and concentration changes in liquid samples is presented in Chapter 4.



# 3

## Directing Thermal Radiation for Spatially Structured Cooling

*This chapter presents the development of a novel method for contactless spatially structured cooling. To further expand the principle of radiative cooling, the possibility to direct thermal radiation in a controlled manner by using geometrical optics is investigated. The aim is to thereby substantially improve the efficiency of this cooling pathway and achieve a significant cooling effect in ambient conditions. Thermal conduction and convection counteract the cooling mechanism. With this radiative cooling setup, the cooling dynamics and spatially structured cooling patterns for different solid samples are investigated in detail. The concept is then extended to cool down a plant leaf, the first biological sample to be measured via this novel method. Lastly, the concept is applied to demonstrate radiative supercooling of a liquid sample inside a microfluidic chip.*

Radiative cooling in the laboratory environment is mainly discussed theoretically<sup>206</sup> or in near-field applications where resonant heat transfer is achieved. Similar as in Förster resonance energy transfer (FRET)<sup>207</sup> or plasmonic applications,<sup>208</sup> it is well established that the radiative properties of a surface also highly depend on the surrounding environment.<sup>209</sup> Therefore, the near-field is attractive to study such effects as it provides possible efficient relaxation pathways, as experimentally shown by Guha *et al.*<sup>210</sup>

However, radiative cooling in the far-field on the scale of cm has not yet been investigated in this detail. The underlying principle of this work is to investigate the possibility to manipulate the direction of black body radiation and thereby enhance radiative cooling. Generally, the direction of thermal emission can be manipulated using optics, as for any other radiation. When collecting the black body radiation of a body and directing it away onto a cold reservoir or heat sink, it is theoretically possible to cool down the surface of the emitting body.

## 3.1 Thermal Emitter and Absorber

In order to practically implement the idea of radiative structured cooling, thermal emission parameters have to be optimized for radiative cooling. Due to the great relevance of the emissive and absorptive properties of samples exchanging thermal radiation, these two bodies are defined before the optical element is examined.

### 3.1.1 Black Body Emission

In this work, when bringing radiative cooling to the laboratory (cf. [Subsection 2.1.4](#)), the cold universe is exchanged by a sample inside a cryostat at 77 K (liquid nitrogen (N<sub>2</sub>) temperature) and Earth is exchanged with a sample to be cooled down from room temperature, which is 295 K in the controlled laboratory environment. The corresponding Planck spectra are presented in ([Figure 3.1](#)). For the temperature range around room temperature from 0 to 40 °C, the respective range of  $\lambda_{\max}$  values, according to [Equation 2.9](#), is indicated (light red bar). Temperatures of the samples studied in this work will not exceed this range. Coincidentally, this range lies well within the atmospheric window. The spectral densities of the hot sample (red graph) and the cryostat (blue graph) in [Figure 3.1](#) differ by a factor of  $10^7$  in this relevant range. As the heat transfer from the hot to the cold body clearly exceeds the heat transfer in the opposite direction, the radiation from the cryostat to the hot sample can be neglected and the net energy transfer is evidently from the room temperature sample to the cryostat.

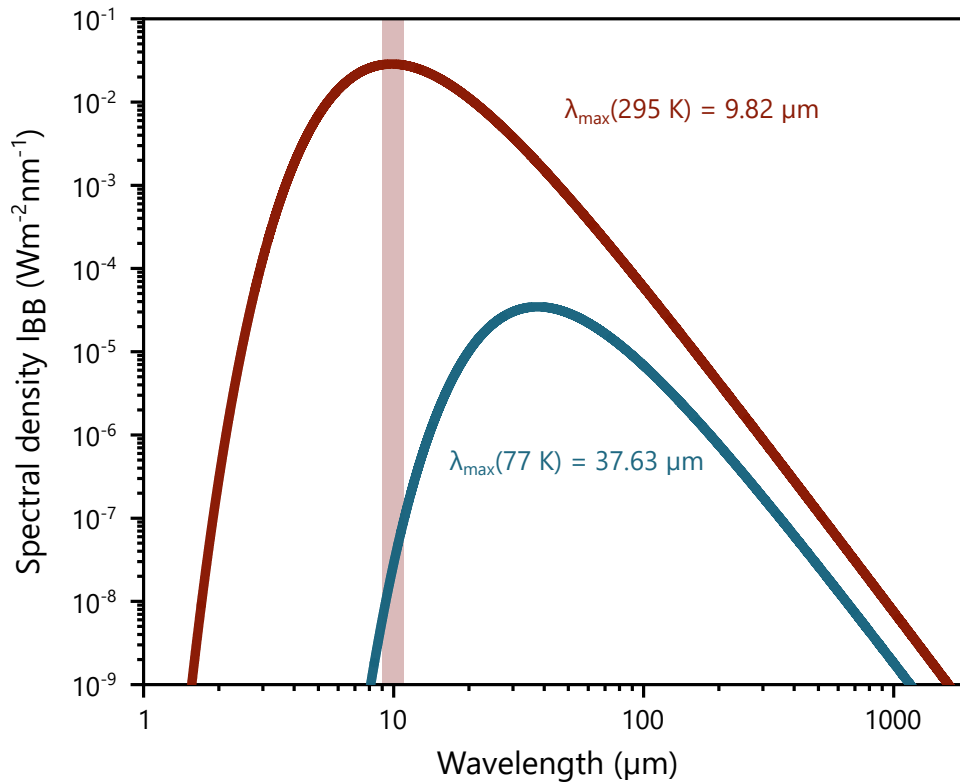


**Figure 3.1:** Planck spectra of the room temperature sample and cryostat cooled sample. The light red bar indicates  $\lambda_{\max}$  for temperatures ranging from 0 to 40 °C. Both axes are logarithmic.

So far, the only input parameters for these plots are the temperatures of the sample and the cold reservoir. From the Planck spectra, the thermal radiation properties are deduced. Considering  $\lambda_{\max}$  for the room temperature sample, it becomes evident that the optics have to be optimized for this wavelength in order to manipulate such radiation.

### 3.1.2 Highly Emissive Hot Sample

First, the hot sample is discussed. As described in [Subsection 2.1.3](#), the emissivity is a crucial material parameter when investigating the radiative energy transfer of a sample. A sample with a high emissivity around  $\lambda = 9.82 \mu\text{m}$  is needed, as this is the maximum emission wavelength at room temperature. A commercially available sample with a high emissivity of  $\epsilon = 0.985$  for the desired wavelength is a metal oxide coated film on aluminum foil (“metal velvet”) purchased from *ACM Coatings GmbH* (subsidiary of *Acktar Advanced Coatings Ltd*, Kiryat Gat, Israel). A metal velvet film cut to a sample size of  $\sim 4 \text{ cm}^2$  and fixed on a glass substrate is used as an emissive sample. The extremely low values of reflectance for this film are presented in [Figure 3.2](#).

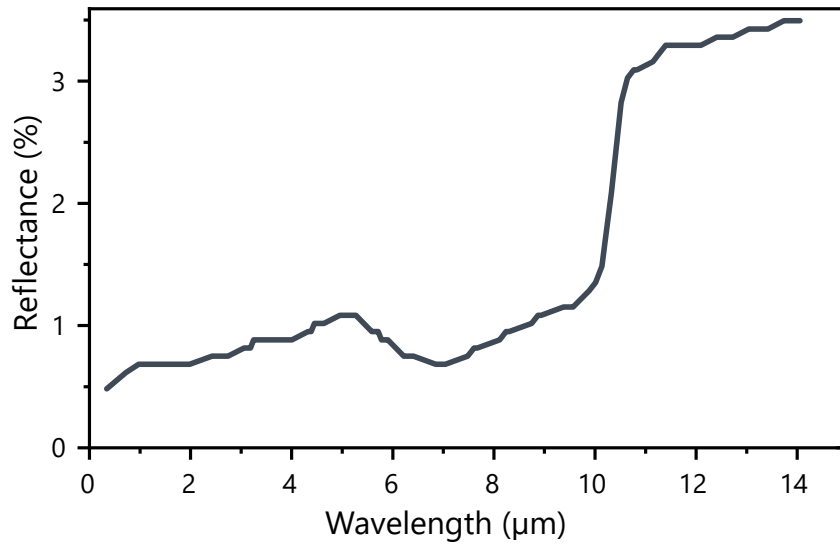


**Figure 3.2: Reflectance of the metal velvet coating.** This data is kindly provided by *Acktar Coatings GmbH*. [Adapted from Reference [211]].

### 3.1.3 Absorbing Cold Reservoir

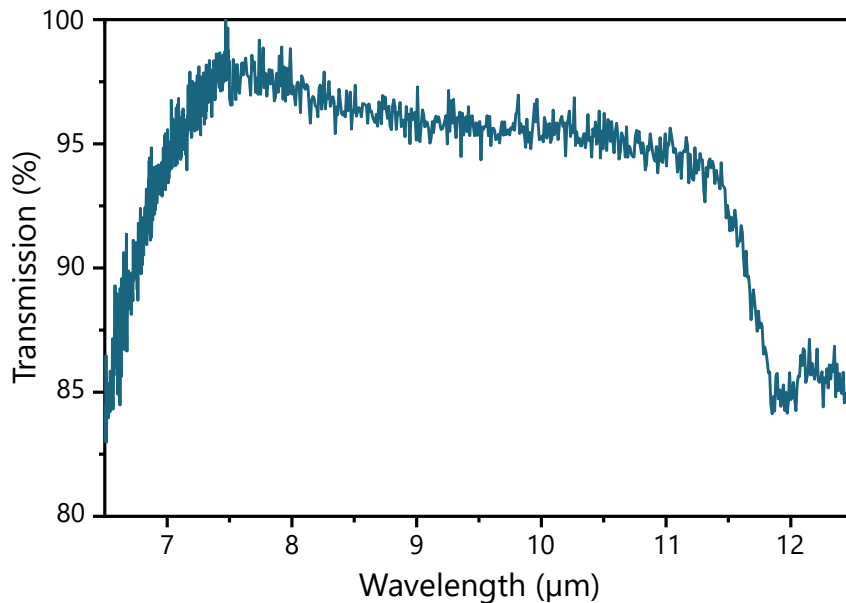


**Figure 3.3: Germanium window transmission.** Transmission data for the germanium cryostat window. The data is kindly provided by *Thorlabs*.

Next, the cold reservoir is considered. As discussed earlier, Kirchhoff's law (Equation 2.14) states that high emissivity also leads to high absorptivity. Therefore, the same metal velvet sample is mounted inside a liquid nitrogen cooled cryostat (*Oxford Instruments*, Barrington, New Jersey, USA) in order to absorb incoming thermal radiation. This sample inside the cryostat serves as a cold reservoir. Inside the cryostat, the sample is in a vacuum chamber, which is cooled with  $N_2$ . The sample temperature can be tuned continuously down to



77 K. Thermally highly conductive silver paint is used to mount the sample in the cryostat. The cryostat is then sealed with a germanium window (Ge) (*Thorlabs GmbH*, Newton, New Jersey, USA), which is transmissive in the infrared in a wavelength range of 7 to 12  $\mu\text{m}$  (see [Figure 3.3](#)). Therefore, it is suitable when cooling down samples from room temperature, since the thermal emission of such samples peaks within this range (cf. [Figure 3.1](#)).

### 3.1.4 Cooling Power

In order to reach a notable cooling effect, the parameters given in the Stefan-Boltzmann law ([Equation 2.10](#)) for the thermal emission power have to be optimized. The power is linearly dependent on the surface area and emissivity. Since a bulk sample would provide a larger volume for conductive heat transfer within the sample, a thin film was chosen.

Considering the surface area and the emissivity of metal velvet, the respective total emission powers can be calculated in accordance with [Equation 2.10](#). The results are

$$P(295 \text{ K}) = 169 \text{ mW} \quad (3.1)$$

$$P(77 \text{ K}) = 785 \text{ } \mu\text{W}. \quad (3.2)$$

Again, it is clearly visible that the net energy transfer takes place from the room temperature sample to the cold sample. The power emitted by the hot sample is almost four orders of magnitude higher than the power emitted by the cold sample. Thus, the metal velvet film should enable a significant cooling effect.

## 3.2 Directing Thermal Radiation

With the emitting hot sample and the absorbing cold reservoir defined, the final aspect concerns the view factor for exchanging thermal radiation. The perceived hemisphere of a sample dictates the potential surfaces to exchange energy with. In order to enhance the radiative cooling pathway and implement a spatially structured cooling, the view factor is shaped.

### 3.2.1 Manipulating the View Factor

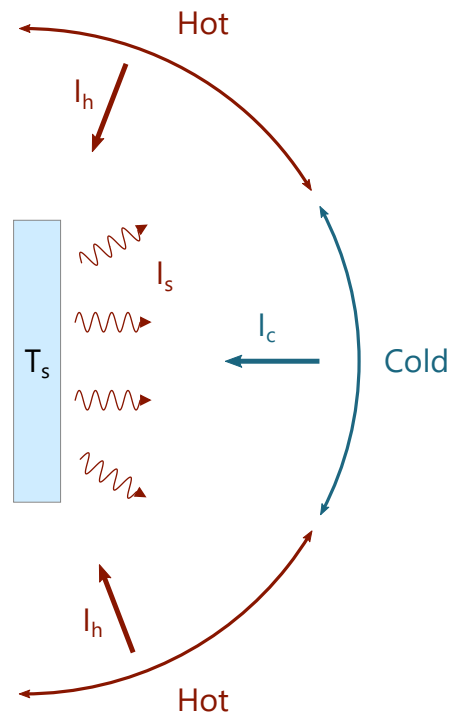


**Figure 3.4: Tunable view factor of the sample.** The sample always emits radiation  $I_s$  according to its own temperature  $T_s$ . The sections of the view factor that surround the sample can be varied in temperature and, therefore, emit onto the sample with radiation originating from hot sections  $I_h$  or cold sections  $I_c$ . This enables an enhanced cooling effect or creates a thermal pattern within the sample.

Figure 3.4 shows the sample and its perceived hemisphere. The sample at  $T_s$  will emit thermal radiation equally at intensity  $I_s$  in all directions. However, in return the radiation incident on the sample depends on the view factor. Thus, the parameter to be tackled is the perceived hemisphere of the sample which may consist of different temperature regions. In the model shown in Figure 3.4 the hemisphere consists of alternating hot and cold sections, emitting thermal radiation with higher intensity  $I_h$  for the hot sections and lower intensity  $I_c$  for the cold sections. Redirecting thermal radiation allows varying the fraction of the view factor perceived as hot or cold by the sample. The aim is to enhance radiative cooling by focusing the thermal radiation onto the cold reservoir.

## 3.2.2 Enhancing the View Factor by Optics

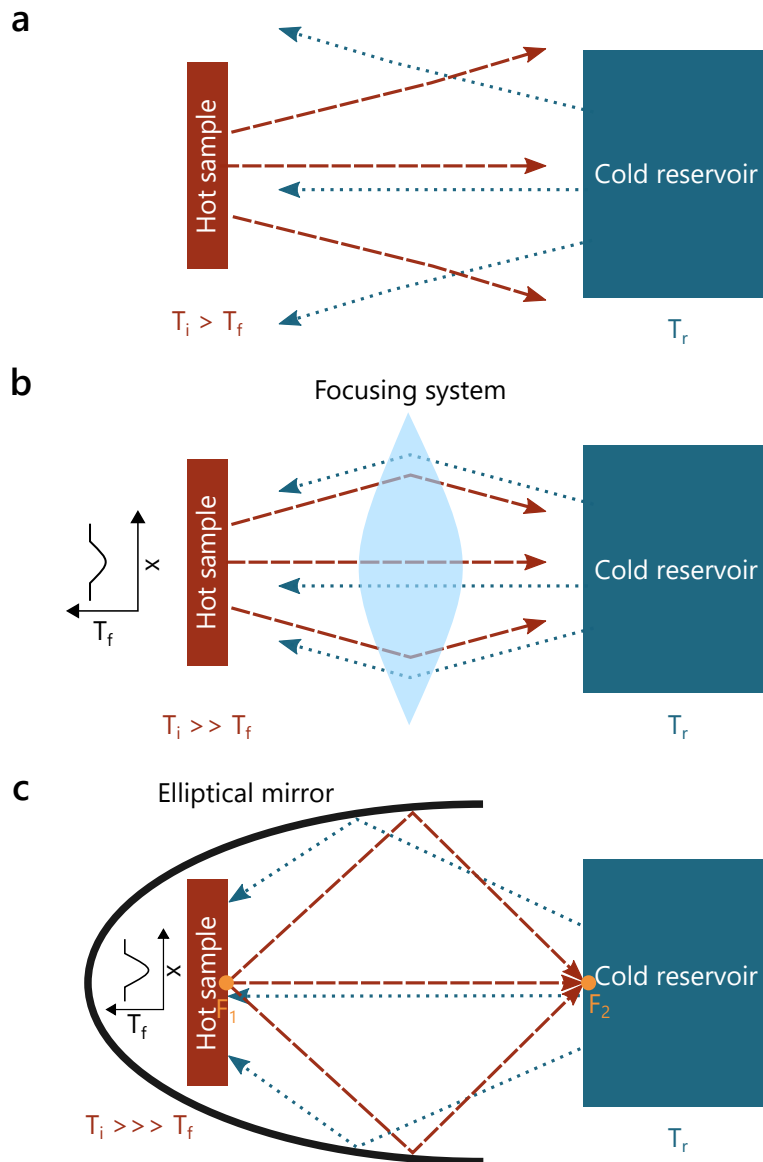


**Figure 3.5: Concepts of enhancing the thermal exchange of two bodies.** (a) A hot sample at initial temperature  $T_i$  exchanges thermal radiation omni-directional with a cold reservoir at temperature  $T_r$ . Over time, the hot sample's temperature will slightly decrease to  $T_f$ . (b) When introducing an optical focusing system, thermal radiation can be directed from the hot sample to the cold reservoir. The hot sample's final temperature  $T_f$  is lower than its initial temperature  $T_i$  and a laterally dependent temperature profile is introduced across the sample. (c) An elliptical mirror captures the maximum emitted radiation at  $F_1$  and focuses it onto a second focal point  $F_2$ . The cooling in the sample is expected to be enhanced, with  $T_f$  being significantly lower than  $T_i$  and the temperature profile will be more pronounced.

In order to manipulate the view factor and create a cooling pattern on the sample surface, three scenarios are considered and depicted in Figure 3.5. Without any optical element, the hot sample and the cold reservoir will exchange thermal energy omni-directionally, with the

net energy going from hot to cold (Figure 3.5 a). The hot sample has an initial temperature  $T_i$  and the cold reservoir is at  $T_r$ . By applying an optical element in form of a lens (Figure 3.5 b), this heat exchange is partially directed and the view factor is enhanced. The hot sample will thereby decrease its temperature to a lower final temperature  $T_f$  and a lateral temperature profile will be observed on the sample. First approaches were in fact tested using a lens with a focal length of 4 cm. However, this configuration only covers a minor portion of the view factor and thereby does not fully exploit the potential to redirect thermal radiation. Although slight differences in temperature between the focal point and an outside point in the sample were detectable, the cooling was not significant. To direct the maximum amount of thermal radiation emitted by the hot sample onto the cold reservoir, the view factor needs to be maximized. Rather than using refractive optics such as lenses, reflective optics in form of an elliptical mirror appear to be the optimal configuration. All radiation emitted in the first focal point  $F_1$  is collected in a second focal point  $F_2$ . This is depicted in Figure 3.5 c and thus selected as the optical element “connecting” the hot sample to the cold reservoir.

### Elliptical Mirror

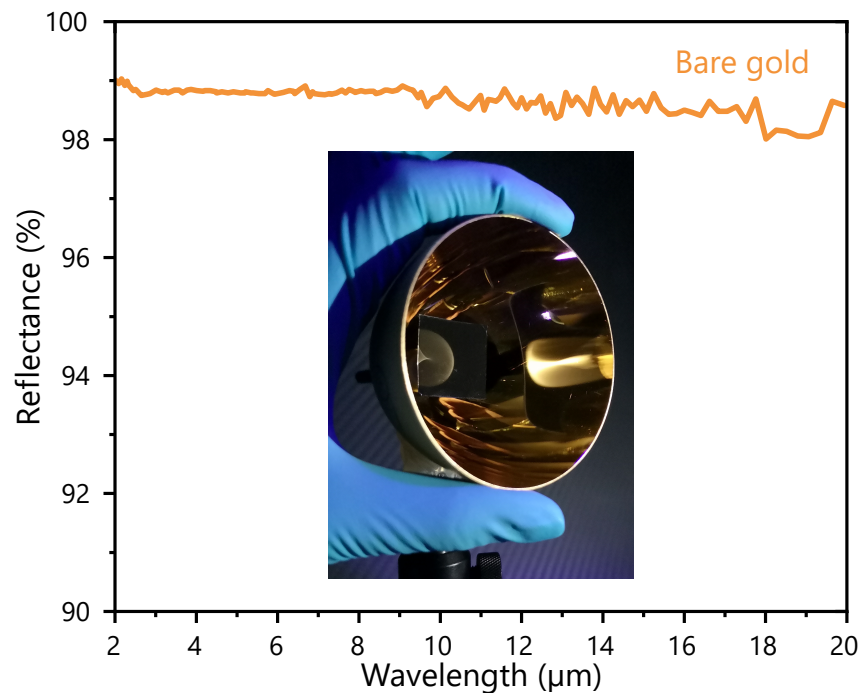


**Figure 3.6: Reflectance of the bare Au elliptical mirror.** A photograph of the mirror is included. This data is kindly provided by *Optiforms*. [Retrieved from Reference [212]].

The elliptical mirror (type E120-100, *Optiforms*, Temecula, California, USA) applied in the setup presented in this work has a diameter of 7.07 cm and the distance between the focal points is 10.16 cm. The entire mirror has a bare gold (Au) coating. The reflectivity data is

plotted in Figure 3.6 and is evidently above 98 % for the entire wavelength range from 2 to 20  $\mu\text{m}$  and thus optimized for the previously determined peak emission of  $\lambda_{\text{max}}(295\text{ K}) = 9.6\ \mu\text{m}$ . Therefore, this coating is highly suitable, also for slightly longer wavelengths, since the emission peak will red-shift as the sample cools down.

### 3.2.3 Quantification of the View Factor Enhancement

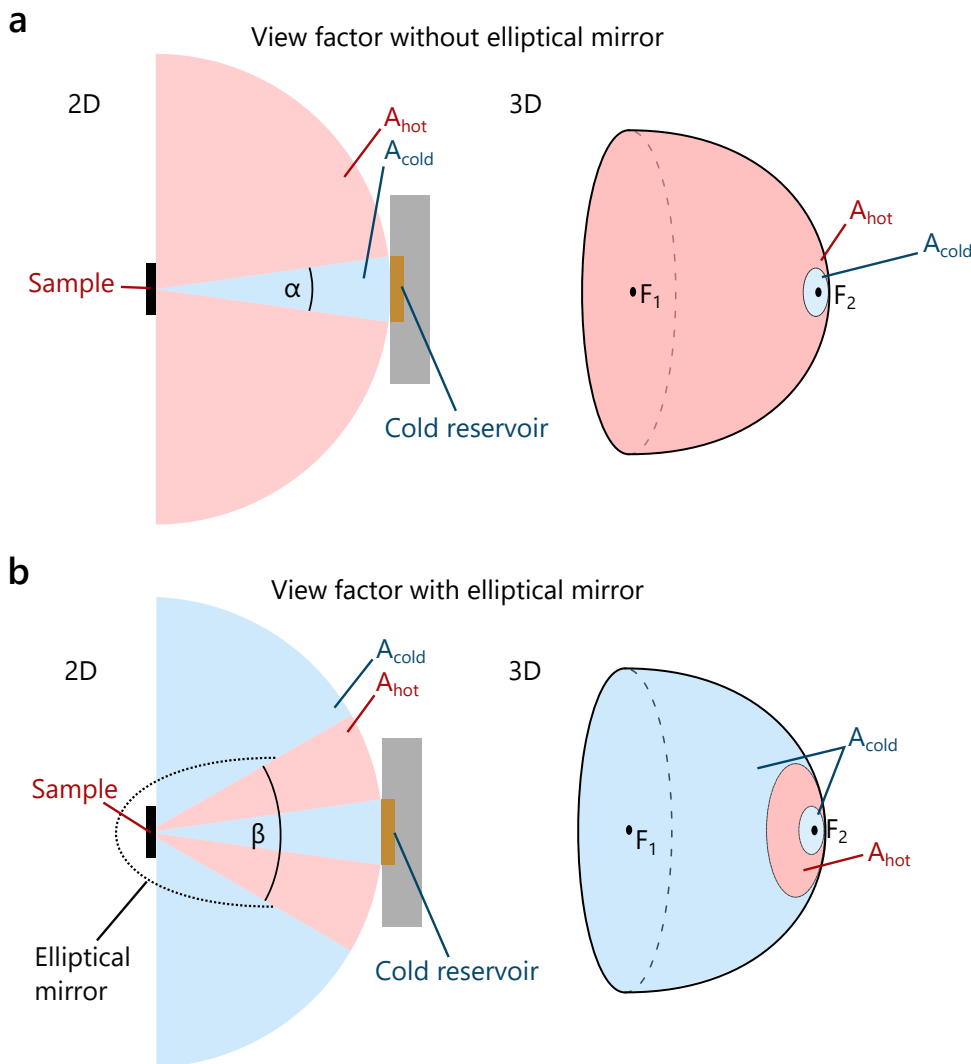


**Figure 3.7: Illustrating the view factor.** Hot and cold view factor sectors as perceived by the sample are shown. On the left hand side the 2D view is presented while on the right hand side a 3D schematic is shown. **(a)** View factor without an elliptical mirror. Only radiation within the opening angle  $\alpha$  is emitted onto the cold reservoir. **(b)** View factor with an elliptical mirror. All radiation except for the emission angle  $\beta - \alpha$  is directed onto the cold reservoir. [Adapted from Reference [213]].

In order to quantify the significance of the elliptical mirror enhancing the view factor, the perceived hemisphere of the sample is calculated. Figure 3.7 illustrates the different view factors of the sample with and without the elliptical mirror. Without the elliptical mirror,

the sample merely “sees” the cold reservoir with an opening angle  $\alpha$ . The 3D illustration in [Figure 3.7a](#) shows how small this area is compared to the entire hemisphere. When introducing the elliptical mirror ([Figure 3.7b](#)), the situation changes drastically. Almost all radiation emitted from the sample is collected and directed to the cryostat window. The only radiation that is still emitted to a room temperature surface is the radiation exiting the mirror and not directly hitting the cold reservoir. This can be quantified by  $\beta - \alpha$ . Due to the close proximity of the back side of the sample to the mirror, most of the radiation emitted at the backside of the sample will be blocked by the sample itself and is therefore not further considered.

When considering the distance  $r = 10.16$  cm between the focal points  $F_1$  and  $F_2$ , it is possible to calculate the surface area of the projected hemisphere with radius  $r$  around the point  $F_1$  in the center of the sample surface. From this, the parts of the hemisphere perceived as hot and cold by the sample can be quantified. The results of these calculations are presented in [Table 3.1](#).

**Table 3.1: Surface areas of the hot and cold hemisphere sectors.** Comparison of the view factor  $F_v$  with and without the elliptical mirror.

	Without mirror	With mirror
$A_{\text{cold}} \text{ (cm}^2\text{)}$	5.07	467.88
$A_{\text{hot}} \text{ (cm}^2\text{)}$	643.52	180.71
$F_{v,c} = \frac{A_{\text{cold}}}{A_{\text{cold}} + A_{\text{hot}}}$	0.78 %	72.14 %

This cold view factor  $F_{v,c}$  can be increased significantly when applying an elliptical mirror. The cold view factor is defined as the fraction of the hemisphere which by the sample is perceived to be cold. In fact, this 92-fold increase of  $F_{v,c}$  enables a significant radiative cooling, as shown later in [Section 3.5](#). Moreover, this underlines why for example a simple lens would not suffice for a measurable cooling effect.

### 3.3 Experimental Setup

Next, the individual components are brought together to introduce the overall radiative cooling setup. A schematic can be seen in [Figure 3.8](#). The elliptical mirror has two foci at  $F_1$  and  $F_2$ . In the first focal point  $F_1$ , the hot emissive sample is mounted on an acrylic handle which can be positioned in the mirror via a hole in the back. The surface of the cold reservoir is placed in the second focal point  $F_2$ . Therefore, the hot sample is exposed to a temperature landscape which is dominated by the cold reservoir in  $F_2$ .

Due to the direction of net energy transfer, thermal radiation will be collected mainly from  $F_1$  and focused on the cold reservoir in  $F_2$ . This geometry leads to a spatially dependent

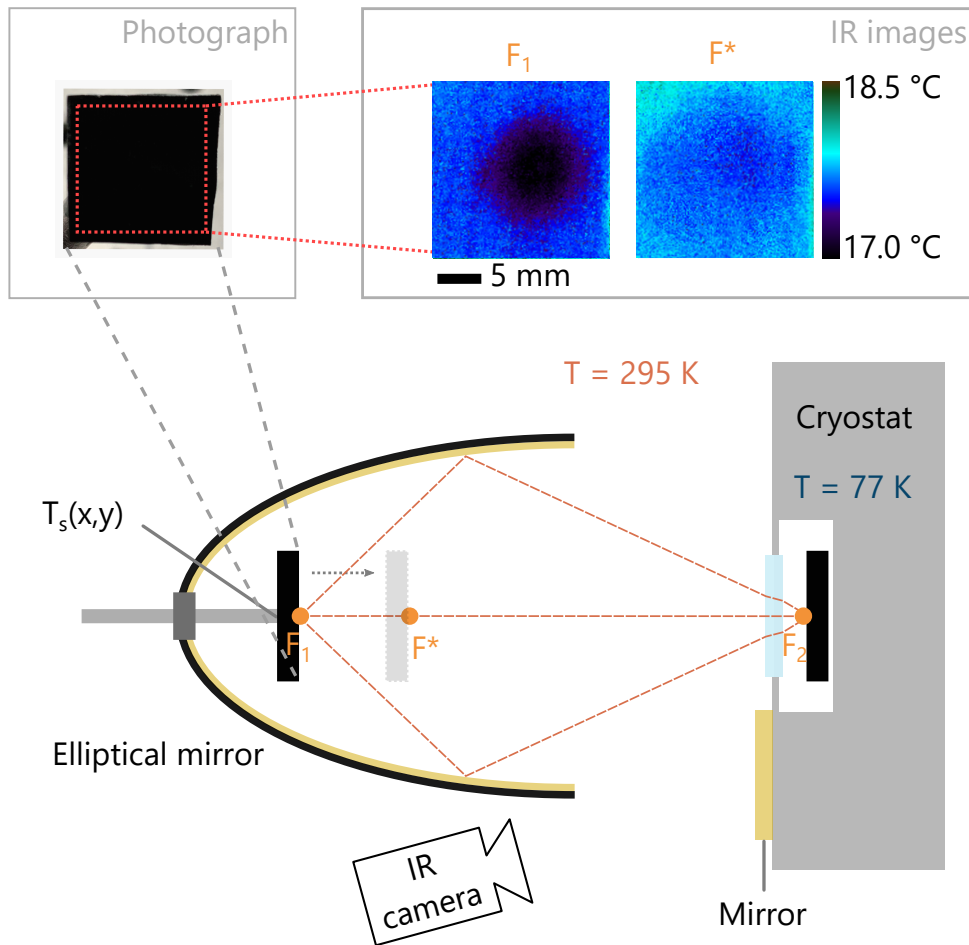


**Figure 3.8: Schematic of the spatially structured radiative cooling setup.** An elliptical mirror focuses the thermal radiation originating from the sample in the focal point  $F_1$  onto the cold reservoir located at the second focal point  $F_2$ . An IR camera images the temperature distribution  $T_s(x, y)$  within the sample. Above the schematic, a photograph of the sample is shown. IR images of the sample placed in the focal point of the mirror  $F_1$  and outside the focal point at a position  $F^*$  are shown on the top right. [Adapted from Reference [213]].

cooling pattern  $T_s(x, y)$  evolving within the hot sample. An IR camera is used to monitor the temperature distribution of the sample surface via the reflection of a flat gold mirror. This additional mirror is outside of the cryostat and at room temperature.

Above the schematic in Figure 3.8, a photograph of the sample is provided. It resembles a black smooth film because of its high absorptivity in the visible range. On the right hand side images of the same sample taken with the IR camera are included. Firstly, an IR image of the sample placed at the focal point  $F_1$  is shown. It can be clearly seen that a temperature profile arises within the sample surface. The central point is coldest and the sample is warmer towards its edge. This cooling profile is the result of radiative heat exchange of the room temperature sample and the cold reservoir. In a control experiment, a second image of the sample is shown when it is moved towards the cryostat and outside of the focal point to an

arbitrary point on the optical axis  $F^*$ . The cold point vanishes and becomes more diffuse. At  $F^*$  only a small fraction of the radiation is directed onto the cold reservoir.

### Thermal Camera



**Figure 3.9: Exemplary IR camera image.** Image of the surrounding of the Nano Institute taken with the thermal camera. Each color is related to a specific temperature by the color bar.

To enable spatially resolved temperature measurements, a long wave infrared (IR) thermal camera (model A655sc, FLIR, Wilsonville, Oregon, USA) is used. The contactless measurement simultaneously enables spatially resolved and minimally invasive temperature measurements since the IR camera at room temperature does not influence the cooling process. The camera measures the incident infrared radiation. With thermal detectors, namely microbolometers consisting of semiconductors, the camera detects the incoming wavelengths and can thereby determine the maximum of the emission curve according to Wien's law (Equation 2.9). From this the camera can directly determine the temperature of an object. Within a single frame, the camera provides a resolution of 30 mK while the overall temperature accuracy is 2 K. Therefore, control thermocouples placed around the elliptical mirror detect the room temperature for the calibration of the camera. Figure 3.9 shows an exemplary image taken by the IR camera.

## 3.4 Creating a Lateral Temperature Profile

The first lateral temperature profiles on a metal velvet sample and therefore the proof of principle of the structured cooling are already shown in Figure 3.8. To examine the effect of thermal conduction and convection limiting the cooling process in depth, the temperature of



the cold reservoir is altered. In this experiment, the cryostat temperature is cooled down gradually and the lateral temperature profile of a borosilicate glass sample is studied. For enhanced clarity of the process description, the sample temperature will be discussed in Celsius and the cryostat temperature in Kelvin.

### 3.4.1 Central Minimum

For a better visualization of the temperature pattern, a borosilicate glass substrate coated in black paint is used due to its lower thermal conductivity compared to the metal velvet sample. The results are presented in Figure 3.10.

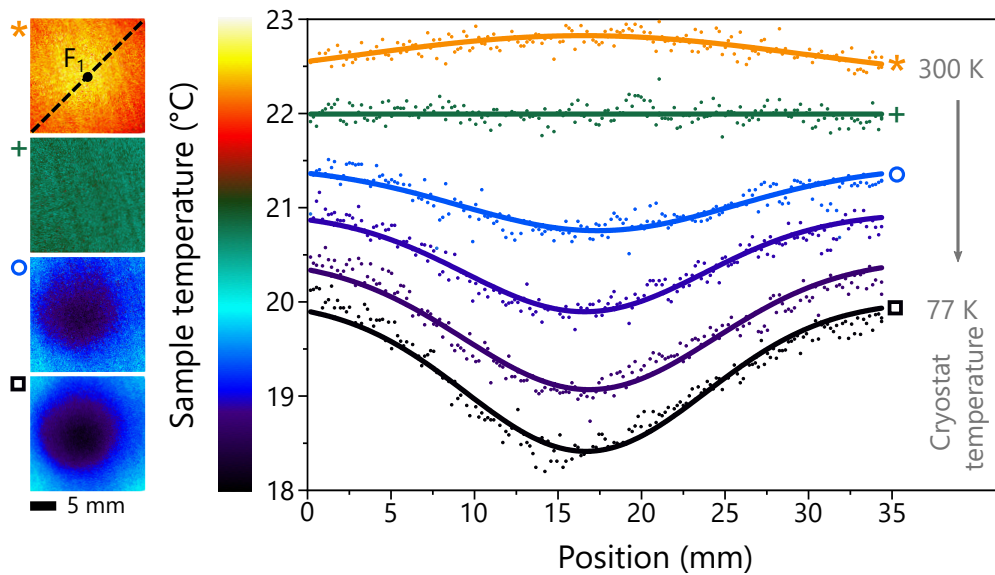


**Figure 3.10: Lateral temperature profile for different cryostat temperatures.** Four exemplary IR images of the borosilicate glass sample can be correlated to the curves via symbols. The dashed line across the first image indicates the extraction position of the temperature profiles. As the cryostat temperature is decreased, the overall sample temperature is reduced and the profile becomes more pronounced. Each color is related to a specific temperature by the color bar. [Adapted from Reference [213]].

A temperature profile diagonally across the sample is evaluated. This is indicated as a dashed line on the first IR image shown in Figure 3.10. The temperature along this cross section is shown in the graphs for different cryostat temperatures. During the experiment, the sample is placed in the focal point  $F_1$  and the temperature of the cryostat is cooled down from 300 K to 77 K over 45 min. The evolution of the lateral temperature distribution  $T_s(x, y)$  is shown with IR images for different cryostat temperatures. At the beginning of the experiment, the cryostat is heated to 300 K, thus slightly above room temperature (295 K). In this case, the direction of radiative heat transfer is reversed. Thus, the temperature profile shows a slight peak in the central position, i.e., the focal point. At this point, the sample is locally heated radiatively. The view factor contains a central hot region instead of a cold one. Therefore,

the dominating radiative heat transfer takes place from  $F_2$  (cryostat) to  $F_1$  (sample). Due to thermal conduction, this heat generated in the focal point is also transferred to the outer parts of the sample and the entire sample temperature rises.

Once the cryostat has reached room temperature, the thermal distribution within the sample is homogeneous and there is no thermal pattern visible, as shown in the second exemplary IR image. The corresponding profile is absolutely flat. The view factor only contains sections of room temperature and is therefore in thermal equilibrium with the environment. As the cryostat starts cooling down below room temperature, the main direction of heat transfer changes and the sample in the focal point  $F_1$  is cooled down. A dip starts to appear in the lateral profiles and a radial thermal pattern  $T_s(x, y)$  emerges. This dip in temperature becomes more pronounced as the temperature of the cold reservoir decreases. For any point on the sample other than the focal point  $F_1$ , the view factor is perceived slightly differently. The portion perceived as cold by the sample is decreased and only close to the focal point it is still significant. In addition to the radiative cooling, the size of the cold spot on the sample is also influenced by conduction and convection processes which counteract the cooling process of the sample. Spherical or chromatic aberrations will also play a role in determining the size of the focal point. At this point it is worth mentioning that the images were taken immediately when the cryostat reached the described temperature. Usually, the entire system requires time to react on a decreased cryostat temperature, i.e., time to reach a thermal equilibrium while the cryostat temperature should be kept constant. However, the focus of this first measurement series lies on the lateral temperature profiles. The cooling dynamics over time are covered in the following section.

Prior to studying the dynamics, the temperature profiles of two different materials are investigated. Different materials also possess different emissive properties, which need to be accounted for. The two investigated samples – coated borosilicate glass and the metal velvet film – are presented in [Figure 3.11](#). Now, in these experiments the cryostat temperature was kept at a constant value of 77 K and the system was given the time to reach a thermal equilibrium. As previously discussed and expected, each sample shows a clear central minimum in the temperature maps of the IR images. In order to compare both samples, a Gaussian fit was applied to the obtained temperature profiles and the respective full width at half maximum (FWHM) extracted for each sample. The coated borosilicate glass behaves significantly different from the metal velvet. The lateral temperature profile of the coated borosilicate glass is shown in [Figure 3.11 a](#), with a FWHM = 18.66 mm. The respective FWHM for the metal velvet film amounts to 6.07 mm and the lateral profile is shown in [Figure 3.11 b](#). Most significantly, the FWHM for the metal velvet film is by a factor of three smaller than for the other sample. The back of the thin metal velvet film consists of an aluminum substrate. This sample exhibits a thermal conductivity of about  $\kappa_{\text{alu}} = 200 \text{ W m}^{-1} \text{ K}$ .<sup>214</sup> This is a large

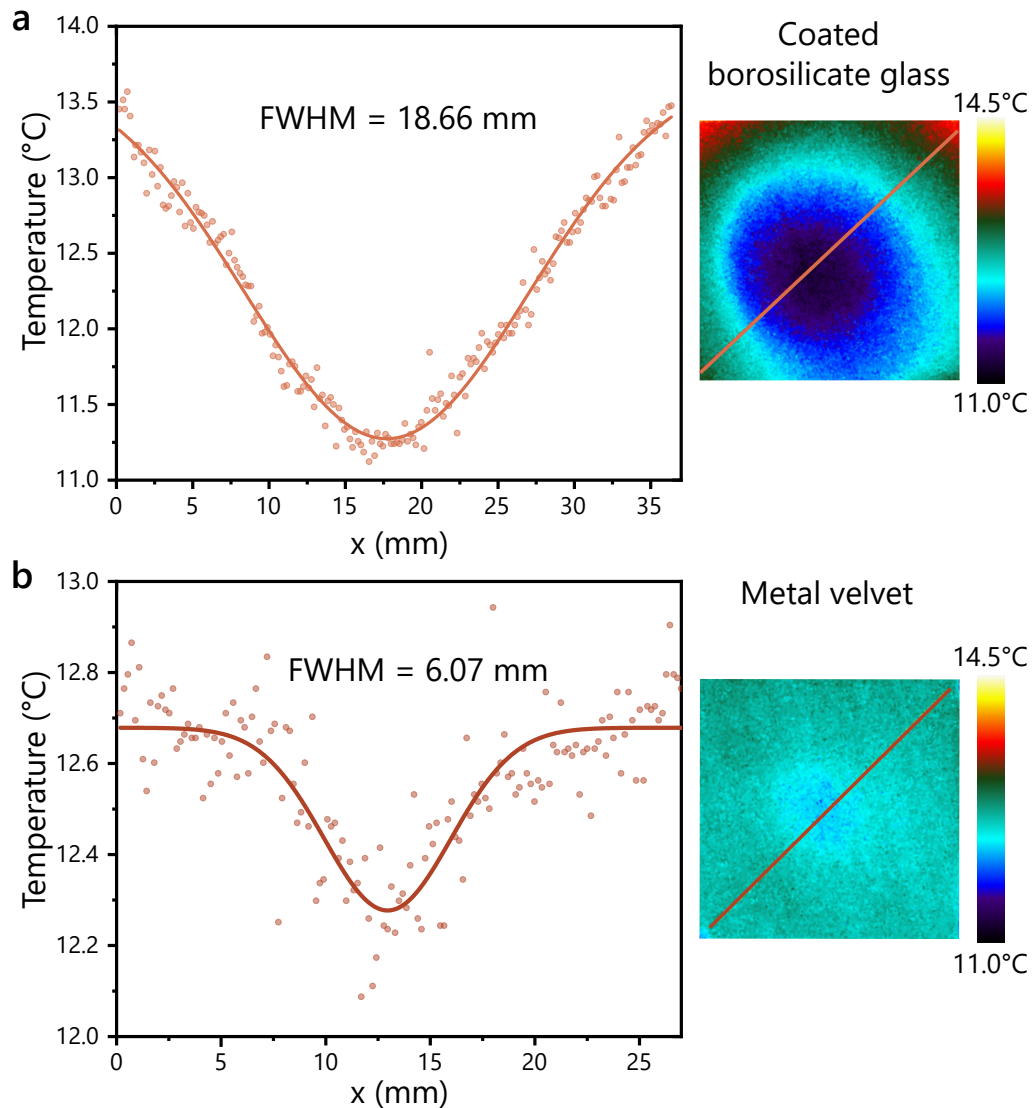


**Figure 3.11: Temperature profiles of coated borosilicate glass and metal velvet.** (a) IR image of the coated borosilicate glass sample including the line along which the temperature profile is investigated. Temperature differences up to approximately 2.4 °C are achieved within the sample. The FWHM of the Gaussian fit is 18.66 mm. (b) Analogously for the metal velvet sample, a temperature difference of approximately 0.6 °C and a FWHM of 6.07 mm are obtained.

thermal conductivity value compared to the one of the coated borosilicate glass which has a conductivity of approximately  $\kappa_{\text{glass}} = 1.15 \text{ W m}^{-1} \text{ K}$ .<sup>215</sup> Therefore, in the metal velvet sample the warmer regions outside the focal point transfer the heat to the central focal point more efficiently while the sample is radiatively cooled down. This explains the different FWHM values which have been obtained for these samples.

Furthermore, the absolute temperature values and gradients within the sample can be compared. Even though the metal velvet sample is expected to exhibit the highest emissivity, the coated borosilicate glass reaches a lower absolute temperature in the central focal point of approximately 11 °C. The maximum temperature difference for metal velvet is at  $\Delta T =$

0.6 °C and for the borosilicate glass significantly higher at  $\Delta T = 2.4$  °C. For each curve the maximum temperature gradient is extracted, resulting in  $\Delta T = 0.08$  °C mm<sup>-1</sup> and  $\Delta T = 0.18$  °C mm<sup>-1</sup> for the metal velvet and the borosilicate glass, respectively. This is a clear depiction of the influence of the conductive properties on the overall cooling dynamics. Thus, while the metal velvet sample may reach a lower average temperature, the borosilicate glass reaches a lower central temperature due to the significantly lower thermal conductivity. Additionally, the overall sample size plays a role for the cooling pattern, especially for samples with high thermal conductivities. If the sample is smaller and entirely placed in the focal point, the impact of thermal conductivity and convection is decreased and lower minimum temperatures could be reached.

### 3.4.2 Shaping the Thermal Pattern

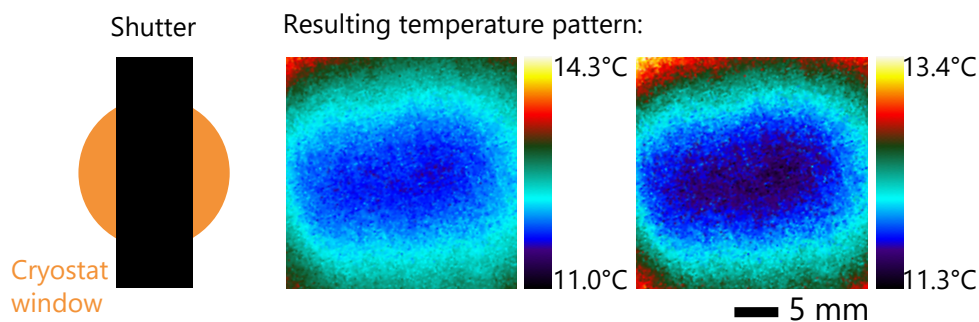


**Figure 3.12: Advanced cooling pattern.** The view factor is shaped with shutters and thereby an advanced cooling pattern is achieved. The central part of the cryostat window is covered with a rectangle, as shown schematically. Resulting cooling pattern on the borosilicate glass sample measured with the IR camera are shown with two different temperature scales.

In a first attempt to further shape and tune the cooling pattern, shutters were added to the radiative cooling setup in front of the cryostat window in order to alter the view factor. The sample in this case is the borosilicate glass. As depicted in [Figure 3.12](#), it can be seen that creating a pattern is indeed possible simply by blocking parts of the cryostat window. Here, the central section of the cryostat window and therefore the cold reservoir is blocked. This results in a longitudinally stretched cooling pattern, which is no longer radially symmetrical. The temperature difference presented is in the same order as in the previous experiment with the borosilicate glass.

Moreover, in a similar fashion, an iris was placed in front of the cryostat window and the impact on the cooling pattern was investigated. The results are shown in [Figure 3.13](#). In [Figure 3.13 a](#), a series of images is taken as the iris closes successively. The cold central spot clearly vanishes but the general shape of the cooling pattern remains radially symmetric. However, again, a significant amount of the solid angle is blocked by the iris. Therefore, the overall cooling power decreases. Interestingly, [Figure 3.13 b](#) shows an unplanned measure-

ment, where the iris was not placed exactly in the center of the cryostat window. It clearly generates an interesting pattern and suggests the possibility to elaborate thermal patterning with appropriate shutters and optics. In future measurements, samples with lower thermal conductivities would render pattern shaping with higher absolute differences possible.

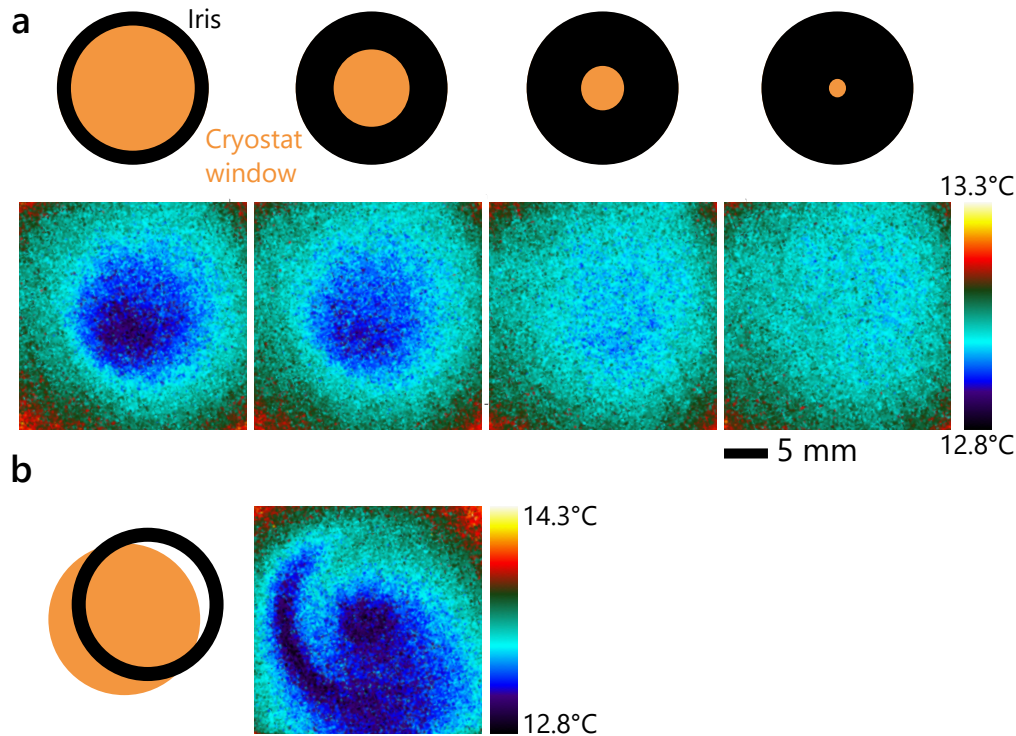


**Figure 3.13: Decreasing the cold reservoir diameter.** (a) An iris is placed directly in front of the cryostat Ge window of the cryostat. It is closed successively and the corresponding IR images of the borosilicate glass sample are provided. (b) The iris is placed off-center in front of the cryostat window.

However, the small temperature differences presented in the color bars in [Figure 3.12](#) and [Figure 3.13](#) should be considered. In future measurements, samples with lower thermal conductivities would render pattern shaping with higher absolute differences possible, and thus enhance the potential for thermal structuring, also on smaller scales.

### 3.5 Radiative Cooling Dynamics

Next, the dynamics of this cooling mechanism are investigated. The sample is macroscopic and therefore the cooling process is expected to take place on a long time scale on the order of minutes. As described previously, the sample is placed in the focal point  $F_1$  while the second focal point  $F_2$  is positioned on the cold reservoir (see [Figure 3.8](#)). Around the elliptical mirror, especially between the mirror and the cryostat, several thermocouples are placed in order to simultaneously monitor the temperature of the surrounding air. Due to the minuscule

size of these thermocouples, their effect on the view factor can be neglected. Firstly, the metal velvet sample is investigated and later the concept is extended to a biological sample, namely a plant leaf.

### 3.5.1 Metal Velvet Sample

Prior to each of these cooling dynamics experiments, the metal velvet sample is heated radiatively to 40 °C using a heating foil. This is done in order to discriminate between the three pathways of heat transfer – convection, conduction and radiation – as introduced in [Subsection 2.1.1](#). The convection and conduction pathways obey Newton’s law of cooling and resemble a mono-exponential temperature decay process. The radiative cooling, however, is best described by the Stefan-Boltzmann law (see [Equation 2.10](#)) and is therefore expected to deviate from a mono-exponential decay. Especially for higher temperature differences between the sample and the cold reservoir, due to the  $T^4$  dependence, the total cooling rate will be increased. By previously heating the sample, we disentangle the efficiency of the radiative cooling process and the usual Newton cooling. The results for the cooling of the metal velvet film are presented in [Figure 3.14](#). The gray curve is the monitored room temperature measured by a control thermocouple. The other three curves present the temperature decrease in the focal point of the sample for different configurations.

Firstly, the radiative cooling of the metal velvet sample was measured with the setup as described before. This measurement with the strongest temperature decay is presented by the blue curve in [Figure 3.14](#). The cryostat was cooled down to 77 K. After 1250 s, the center of the metal velvet sample reaches approximately 12 °C, roughly 10 °C below the measured room temperature. At this point, the radiative cooling process approaches an equilibrium as the temperature stabilizes due to competing effects which heat up the sample. On the one hand, thermal conduction within all components touching the sample warm up the sample. To minimize undesired warming of the sample via thermal conduction, i.e., to thermally isolate the sample, materials with low thermal conductivities are chosen for the sample base and the sample mounts. Convection additionally plays a major role. The entire air around the experimental setup is at room temperature and since the sample is not positioned in a vacuum, convection heats the sample simultaneously. Lastly, while the radiative component is responsible for the cooling of the sample, the view factor also contains regions which are perceived by the sample to be at room temperature (cf. [Figure 3.7b](#)). Radiation originating from these regions also competes with the cooling process. Even though the view factor was enhanced by a factor of 92 when introducing the elliptical mirror, still 28 % of the temperature landscape is perceived at room temperature (cf. [Table 3.1](#)). Summing up, this enhanced radiative cooling pathway leads to an accelerated cooling process, resulting in a temperature

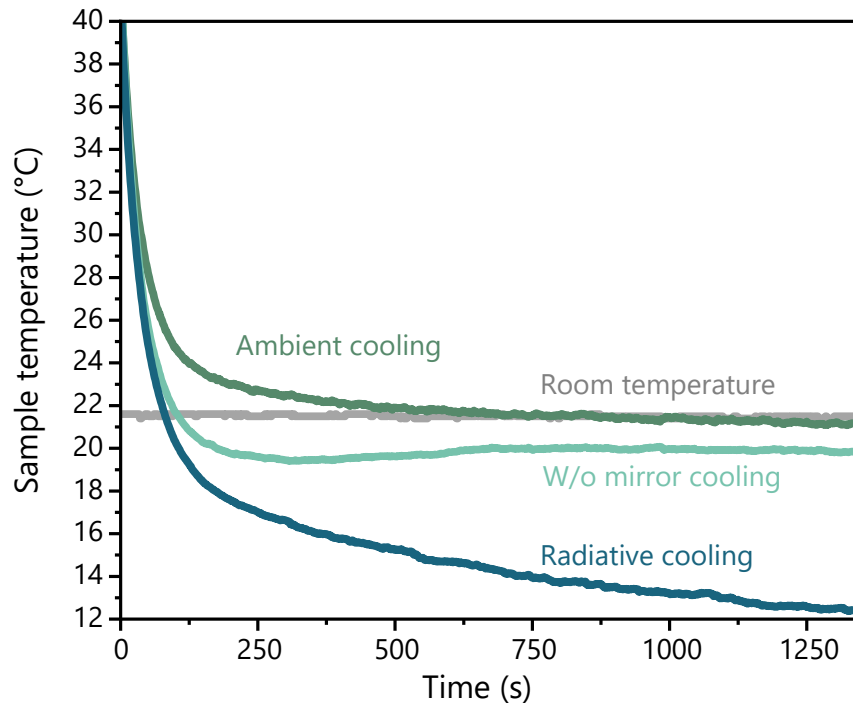


**Figure 3.14: Cooling dynamics of the metal velvet sample.** Three measurements of the metal velvet sample are performed. In all cases the sample is initially heated to 40 °C. The temperature is recorded with the IR camera at the focal point  $F_1$  in the center of the sample. First, the sample is cooled with the elliptical mirror present (blue), then the elliptical mirror is removed and the identical region of interest (ROI) is measured (turquoise curve) and finally the cold reservoir is heated to room temperature to measure the ambient cooling dynamics (green curve). The room temperature is monitored as a reference (gray curve). [Adapted from Reference [213]].

10 °C below ambient. As mentioned in the previous section, smaller samples are expected to reach even lower temperatures.

Secondly, in order to separate the individual pathways of heat transfer, the elliptical mirror is removed while the cryostat is still running and keeping the cold reservoir at 77 K. In other words, the view factor is now decreased by a factor of 92 (cf. Figure 3.7 a) and only 0.78 % of the sample's view factor consists of cold area (cf. Table 3.1). The black body radiation of the sample can now propagate freely within the room. Again, the same sample is heated to 40 °C and the consecutive temperature decay is monitored (turquoise curve in Figure 3.14). A cardboard box resembling the shape of the elliptical mirror is placed around the sample in order to maintain similar convective conditions. The resulting cooling trace shows that the preheated sample cools down slightly below room temperature to approximately 20 °C. The cooling is now partially due to the radiative component and residual convection effects from the cold reservoir. This underlines the significance of the elliptical mirror.

Lastly, the same sample was heated to 40 °C once more and this time the temperature decay is measured without the mirror and without the cold reservoir, i.e., the cryostat was switched off. This measurement is labeled ambient cooling and is shown by the green curve in Figure 3.14.

The curve shows an exponential temperature decay and finally reaches room temperature. Theoretically, in this cooling process, conduction and convection are expected to dominate and therefore the sample would cool mono-exponentially over time in accordance with Newton's law of cooling (cf. [Subsection 2.1.1](#)).

Additionally, it is necessary to consider the temperature dependence of the emission power and peak wavelength  $\lambda_{\max}$  (cf. [Equation 2.10](#) and [Equation 2.9](#), respectively). The power emitted by the sample decreases significantly with decreasing temperature due to the  $T^4$  dependence. For a temperature decrease from 40 °C to 10 °C, the emitted power decreases by 71 mW, which represents a decrease of 36 %. The peak emission wavelength  $\lambda_{\max}$  red-shifts with decreasing temperature, thus the transmissivity of the cryostat window decreases. These effects are two additional reasons to explain why the cooling becomes less efficient, as the sample gets colder.

For a quantitative discussion, the radiative cooling (blue) and the ambient cooling (green) are fitted and compared. First, looking at the ambient cooling, the coefficient of determination  $R^2$  of 0.97 for a mono-exponential fit is substantially high and therefore confirms the cooling process obeying Newton's law. The cooling rate extracted from the fit is  $\kappa_{ac} = 17.5 \text{ mK s}^{-1}$ . The radiative cooling curve is fitted by the same approach and yields a coefficient of determination  $R^2$  of only 0.91, indicating the expected deviation from a mono-exponential process. The calculated cooling rate yields  $\kappa_{rc} = 26.4 \text{ mK s}^{-1}$ . When comparing both rates, it becomes clear that applying radiative cooling with the elliptical mirror significantly enhances the overall cooling process. By the results presented in [Figure 3.14](#), it is thereby possible to disentangle conduction, convection as well as the radiative pathway and compare radiative cooling to ambient cooling. The effect of the elliptical mirror and the enhanced view factor is clearly demonstrated.

### 3.5.2 Biological Sample

As a first application, the possibility to radiatively cool biological samples was tested on a *Dracaena marginata* leaf. The leaf was cut to fit the sample holder and then mounted inside the elliptical mirror (see [Figure 3.15 a](#)). The sample was cooled with the radiative cooling setup with the cold reservoir temperature at 77 K. As investigated in literature,<sup>8,9</sup> plants exhibit strong thermal emissions and can even be identified by their IR spectra.<sup>7</sup> In [Figure 3.15 b](#), the cooling dynamics for the leaf are presented for the entire sample as well as the focal point  $F_1$ . Initially, the sample is at room temperature and when unblocking the cold reservoir, the cooling process sets in immediately. Within 1200 s the center cools down to 10 °C while the average temperature of the whole sample reaches 12 °C. Due to its high emissivity but low thermal conductivity, this sample is ideal for generating a lateral cooling pattern. Between



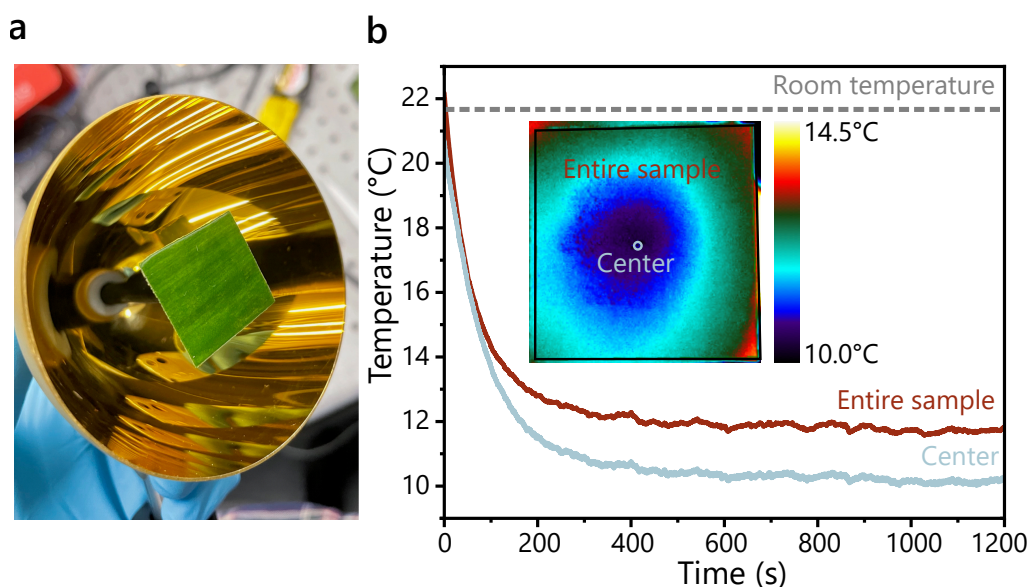


**Figure 3.15: Cooling dynamics of a biological sample.** (a) A photograph of the plant leaf inside the elliptical mirror is shown. (b) The cooling dynamics of the entire sample (average temperature of sample surface) as well as the central focal point are shown. The evaluated ROIs can be seen in an exemplary IR image.

the central point and the edges there is a temperature difference of 3 °C and the FWHM of the temperature profile amounts to 17.04 mm. A typical thermal conductivity for plants is on the order of  $1 \cdot 10^{-1} \text{ W m}^{-1} \text{ }^\circ\text{C}$ .<sup>216</sup> Low conductivities like this enable higher temperature gradients and more effective cooling. This setup can be adapted to induce a temperature gradient in live biological samples, e.g., cell cultures.

## 3.6 Radiative Supercooling

When substances cool down and surpass the temperature of their freezing point, they can perform a phase transition, depending on their pressure. Specific heat capacities determine the energy required for a phase transition to take place. However, considering isobaric conditions, phase transitions do not always occur when the temperature of a substance passes the freezing or the boiling point. The process in which a substance is cooled down to its phase transition temperature and below, without the phase transition taking place, is called supercooling.

### 3.6.1 Supercooling: Cooling Liquids Below Their Freezing Point

Water, for example, can be cooled below its freezing point without changing its state of matter from the unordered liquid phase into an ordered solid crystal phase. This supercooled

state, however, is only metastable, as it is only possible due to the lack of kinetic energy.<sup>217</sup> At this point any impulse can provide the system with the necessary free energy for a cluster of molecules in the liquid phase to overcome the nucleation barrier and perform a phase transition immediately.

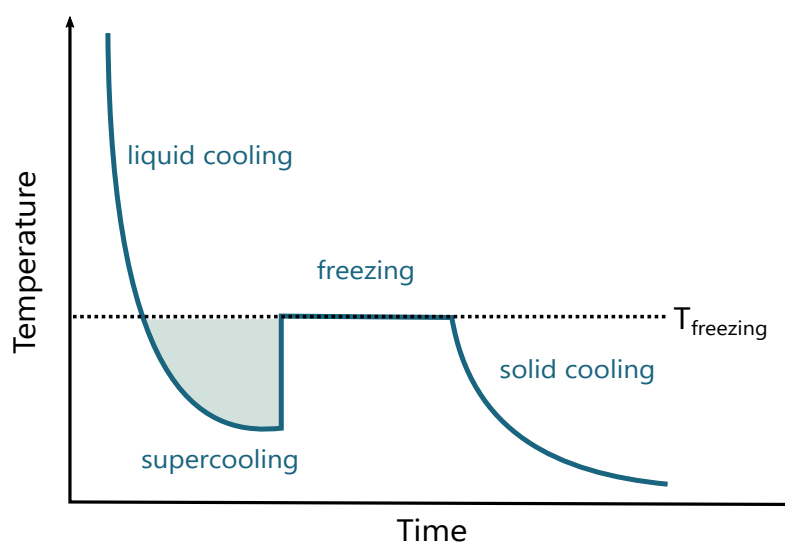


**Figure 3.16: Schematic supercooling of a liquid.** The graph sketches the temperature of a liquid that is cooled down below its freezing point and then freezes. Supercooling is the cooling process below the freezing point, before the phase transition occurs. The freezing is indicated by a sudden increase in temperature. After the phase transition is performed at a constant temperature, the solid continues to cool down.

Figure 3.16 visualizes this process for a liquid which is cooled down. First, the temperature of the liquid decreases over time. The freezing point of a liquid is a commonly known material constant. However, it is not common knowledge that this is usually referring to the heterogeneous freezing point. The heterogeneous freezing or nucleation point is when crystals within a liquid can begin to nucleate while the homogeneous freezing point is the temperature when the liquid has to freeze.<sup>218,219</sup> The difference between these two points defines the possible supercooling range. In Figure 3.16 the phase transition is indicated by the steep and sudden rise in temperature. Due to the freezing, the sample warms up. It may seem counterintuitive but freezing is an exothermic process. The particles have excess energy when transitioning from the unordered liquid phase into the ordered solid phase which is released in the form of heat. From there it can be further cooled down, however, the cooling rate in the solid phase may vary from the cooling rate before the phase transition.

In nature, supercooling may occur in plants<sup>220</sup> or animals<sup>221</sup> inhabiting regions of extremely low temperatures. Such supercooling is for example highly desirable in the preservation of biological tissue, as the formation of ice crystals in water can be harmful for cell tissue. Supercooling has only recently been developed into a method that can allow a prolonged preservation of human organs for donations,<sup>222</sup> for example for livers up to 27 hours.<sup>223,224</sup>

Another field where this is highly useful concerns the preservation of food<sup>225</sup> and other biological samples, like water based samples<sup>217</sup> or lipid based particles.<sup>226</sup> As indicated above, conventional cooling may lead to the formation of ice crystals in the sample which in turn may lead to a quality loss. Finally, for the field of thermal batteries<sup>227</sup> and phase-change materials<sup>228–230</sup> supercooling is of high interest.

Since any disturbance to the system can initiate spontaneous crystallization, highly quiescent experimental conditions are absolutely crucial to achieve the supercooling effect.<sup>226</sup> Standard cooling approaches via thermoelectric devices, liquid or gaseous cooling agents or simple ventilation are not necessarily ideal, since in these approaches cooling is always achieved via direct contact to the sample. Compared to those techniques, radiative supercooling introduces a contactless pathway to cool down samples and, therefore, seems to be an ideal candidate to enable supercooling applications. To demonstrate this idea, radiative supercooling of hexadecane ( $C_{16}H_{34}$ ) is performed. Hexadecane has a melting temperature at 18 °C and is therefore ideally suited for the temperature range the here developed setup operates at.

### 3.6.2 Microfluidic Chips

For the supercooling application, a microfluidic chip was designed and built with support from Stefan Niedermaier. In an acrylic glass sample of 24 mm x 24 mm with a thickness of 4 mm, five holes shaped like the 5-face of a dice were drilled. A schematic of the chip can be seen in [Figure 3.17 a](#) and a photograph in [Figure 3.17 b](#). This configuration is chosen to compare a central chamber in the focal point with chambers slightly outside the focal point. On one side of the acrylic glass, a 170  $\mu\text{m}$  thick borosilicate glass substrate (VWR, Radnor, Pennsylvania, USA) was glued. The five chambers were then filled with liquid hexadecane. Hexadecane was purchased (*Sigma Aldrich*, St. Louis, Missouri, USA) and used without any further purification. To ensure that the volume of the hexadecane will still fit in the chamber when in the solid state, the sample was frozen and excess hexadecane was removed. The final volume of hexadecane is 30  $\mu\text{L}$  per chamber. The chip was then sealed with a second 170  $\mu\text{m}$  glass substrate. The glass substrate at the back of the chip is coated with black paint for higher contrast. The chip is mounted in the radiative cooling setup in a fashion that the central chamber is placed in the focal point of the elliptical mirror (position 1) while the four chambers on the outside are slightly out of focus (position 2). This provides the possibility to investigate the structured cooling effect on supercooling of fluids. The sample's initial temperature is at room temperature and as for the previous samples, the temperature is measured using the IR camera.

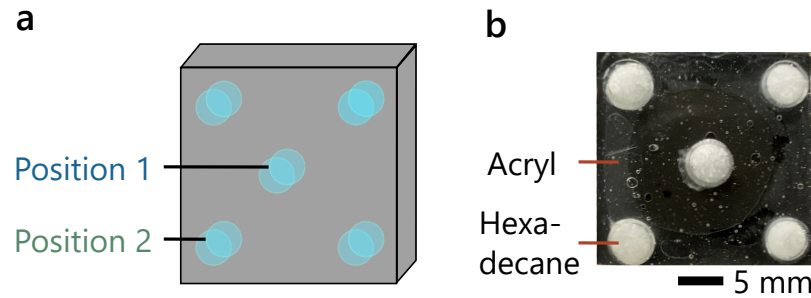


**Figure 3.17: Home-built microfluidic chip.** (a) Schematic of the chip with 5 microfluidic chambers arranged like the 5-face of a dice. (b) Photograph of the microfluidic chip with the hexadecane in the solid (opaque) state. [Adapted from Reference [213]].

### 3.6.3 Supercooling Dynamics

Firstly, the temperature evolution of position 1 is shown in Figure 3.18 a. In position 1 it is evident that after  $\sim 180$  s of cooling, the melting point of  $T = 18^\circ\text{C}$  of hexadecane is reached. As anticipated, no phase transition is seen and the cooling of the sample progresses further. Once the sample reaches  $12.2^\circ\text{C}$ , a sudden jump in the temperature to  $14.6^\circ\text{C}$  within about only 1 s is clearly visible and also highlighted in the inset. This is an indicator of spontaneous crystallization. The solidification of hexadecane is also clearly visible by naked eye, since hexadecane turns opaque in the solid phase (as visible in Figure 3.17 b), while it is transparent in the liquid phase. Immediately after the crystallization, the temperature of the solid hexadecane continues to decrease, down to a value of  $\sim 11^\circ\text{C}$  which is reached 2000 s after starting the measurement. Three exemplary images from the IR camera are shown. The black circle in the first image indicates the investigated hexadecane chamber and therefore the region of interest. The three symbols next to the graph indicate at which times the IR images have been obtained. First, after 720 s, the coldest point of the sample is the center and the hexadecane in position 1 is cooled in the liquid phase. After 1266 s hexadecane transitioned from a liquid into a crystalline phase and a sharp increase in temperature is measured in position 1. Lastly, after 1354 s, the sample is cooled down mostly homogeneously and the hexadecane in the chamber in position 1 continues to cool in the solid phase.

In position 2, supercooling and the corresponding phase transition are also observed, as shown in Figure 3.18 b. This position is, as mentioned before, outside the direct focal point of the elliptical mirror. As discussed in Section 3.4, the cooling effect is therefore impaired but still present. The supercooling dynamics in position 2 behave similar to position 1. The notable difference is, however, the cooling rate and the time of the phase transition. The chamber in position 2 indicates a phase transition at about 1500 s after the cooling started, thereby being slower than the same process at position 1. Again, when  $12.2^\circ\text{C}$  is reached, the phase transition occurs. Similarly, the temperature jumps to  $14.6^\circ\text{C}$  and then cools down again. As before, the inset shows the precise moment of this phase transition. It can be seen

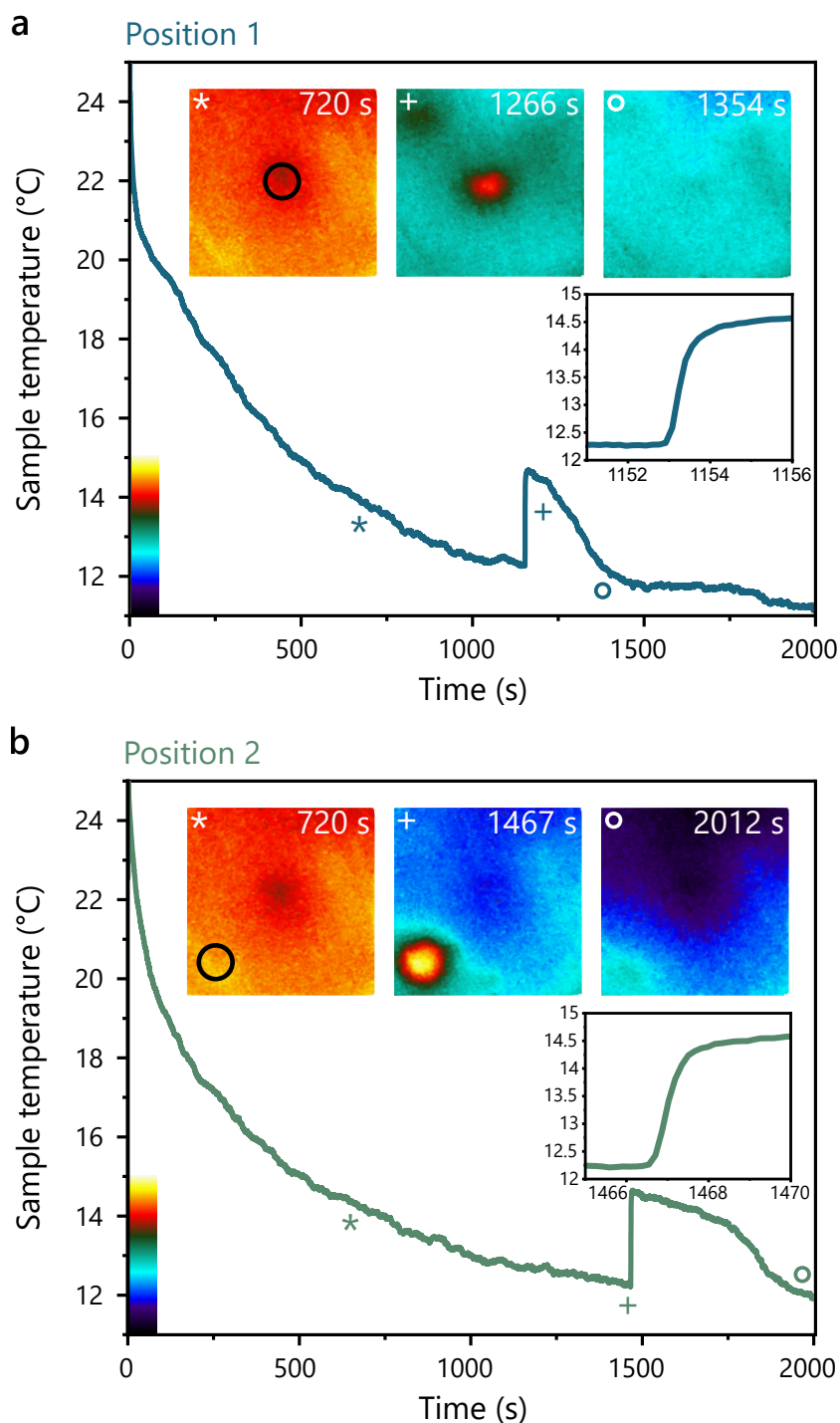


**Figure 3.18: Radiative supercooling of hexadecane.** (a) Temperature against time illustrating the cooling dynamics of position 1. IR images are shown for three different frames. A black circle indicates the investigated chamber. The images are correlated to the cooling curve via symbols. The phase transition is seen in the IR images by the sudden heating up of the chamber. An inset shows the phase transition in detail. The color bar next to the y-axis is used for the temperature mapping of the IR images. (b) Identical data for position 2. [Adapted from Reference [213]].

clearly that this process takes about 1 s, while the cooling down takes place on the order of minutes. IR images of different time points are shown above the graph. This time the relevant chamber is outside the focal point, indicated by a black circle in the first image. After 720 s, position 2 has cooled down significantly even though it is not directly in the focal point  $F_1$ . Cooling takes place in the liquid phase until the phase transition after 1467 s, which is seen by the sudden increase in temperature. The sample then cools down in the solid phase until the temperature distribution on the sample surface is homogeneous.

The temperature values of the phase transition in the measurements agree very well with previously reported values for supercooling hexadecane. As discussed above, supercooling can only take place until the sample has reached its homogeneous nucleation temperature. According to Abramov *et al.*,<sup>231</sup> for hexadecane this homogeneous freezing temperature is at  $(12.9 \pm 0.5)^\circ\text{C}$  and the heterogeneous liquid to solid phase transition at  $(15.66 \pm 0.32)^\circ\text{C}$ .<sup>231</sup> Both values are in very good agreement with the data presented in Figure 3.18.

### Quantitative Fitting

Comparing the two positions from a quantitative point of view yields more information about the cooling dynamics. Both curves were fitted with a bi-exponential fit, given by

$$T(t) = a_1 \cdot e^{-\kappa_1 t} + a_2 \cdot e^{-\kappa_2 t} + c. \quad (3.3)$$

to account for the conductive and convective pathways as well as the deviation due to the radiative component. The results of the fits (red curves) are plotted in Figure 3.19 together with the experimental data (blue and green dots) for the cooling curves of both positions. It should be noted that the phase transition jumps were excluded in the fitting procedure.

The fitting parameters obtained from Figure 3.19 are summarized in Table 3.2. The applied function, as given in Equation 3.3, contains two scaling factors,  $a_1$  and  $a_2$ . In Table 3.2 it can

**Table 3.2: Fit parameters of the supercooling dynamics in hexadecane.** The fit parameters are obtained from the bi-exponential fits applied in Figure 3.19.

	Position 1	Position 2
$a_1$	2.97	4.21
$a_2$	10.50	8.57
$\kappa_1$ (mK s <sup>-1</sup> )	138.0	24.1
$\kappa_2$ (mK s <sup>-1</sup> )	19.5	1.9
$c$	11.0	11.8
$R^2$	0.999	0.999

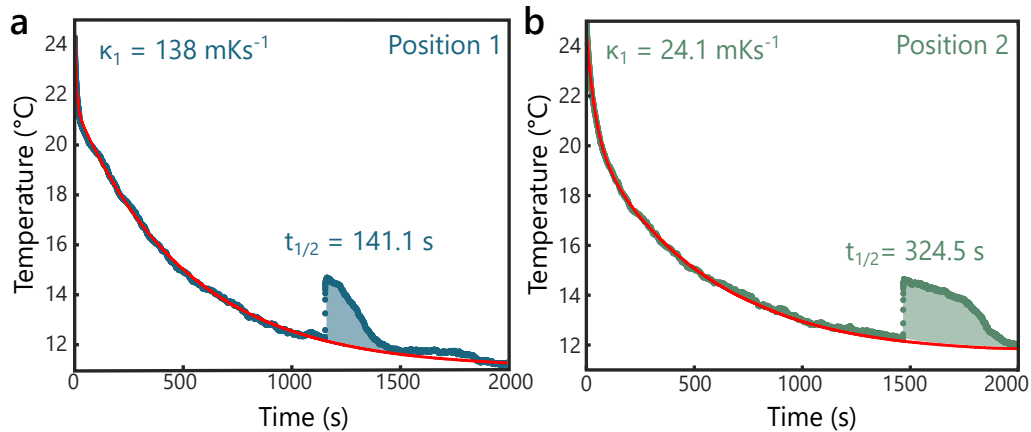


**Figure 3.19: Bi-exponential fitting of the hexadecane cooling process.** (a) Temperature curve (blue dots) including bi-exponential fit of position 1 (red curve). The cooling rate  $\kappa_1$  as well as the half-life of the supercooling peak (shaded area) are shown. (b) The identical information is provided for position 2, where the data points are given by the green dots. [Adapted from Reference [213]].

be seen that these factors are very similar for both fits respectively, and most significantly, on the same order of magnitude. The slow rate  $\kappa_2$  deviates slightly for both curves. The constant  $c$  added in the end is also almost identical. However, the most significant fit parameter is  $\kappa_1$ . This describes the fast rate of the cooling and lies at  $138 \text{ mK s}^{-1}$  for the central position 1. For position 2, however, this cooling rate is significantly reduced to  $24.1 \text{ mK s}^{-1}$ . Initially, since the cooling begins at room temperature, the effect of conduction and convection is zero due to the thermal equilibrium. At this time, only the radiative pathway is significant. Visually, this is seen in Figure 3.19 a, as the initial cooling is substantially steeper in position 1 than in position 2, which is shown in Figure 3.19 b. This first drop dominates the fitting rate  $\kappa_1$  for position 1. As the sample cools down, the conductive as well as the convective pathway gain in significance and the individual pathways cannot be separated as clearly anymore. From this it can be concluded that the central position exhibits a faster initial cooling rate by a factor of five. In order to be able to compare the rates as above, it is crucial that the other fit parameters are of similar value. Lastly, the high  $R^2$  value for both fits of almost 1 confirms the applicability of this bi-exponential fit.

**Table 3.3: Half-life of the supercooling peak in hexadecane.** The half-lives for both positions are calculated from the supercooling peaks in Figure 3.19.

	Position 1	Position 2
Half-life (s)	141.1	324.5

Finally, the half-lives for both supercooling peaks are investigated. These peaks are shaded areas in Figure 3.19 and given in Table 3.3. The half-lives are calculated by considering half

of the time interval it takes for the sample to cool down back to the temperature value it had exactly before the sudden phase transition.

In conclusion, the presented results show the applicability of the setup to supercool liquid samples using the presented radiative cooling setup. The conditions are perfectly quiescent and no external stress on the sample can cause spontaneous crystallization. The structuring of the microfluidic chip allows to compare the chamber in the central focal point to another chamber slightly outside the focal point of the elliptical mirror. Thereby it is possible to compare the cooling dynamics of the two chambers. The cooling is always a competition between radiative heat transfer on one hand and thermal conduction on the other hand while convection from the room temperature air is constantly heating the sample back up. Overall, the difference in the cooling dynamics highlights the effect of the radiative transfer.



# 4 Temperature Sensing With Twisted Light

*This chapter presents the design, setup and application of an orbital angular momentum interferometer for refractive index measurements of a liquid sample. First, the main components and the experimental realization are elaborated in detail. Contactless high-resolution temperature measurements are demonstrated with this novel method. The direct relationship of the refractive index and temperature, called the thermo-optic coefficient, is determined experimentally and correlated to literature values. This applied concept is then extended beyond temperature measurements. The refractive index of a solution is not only temperature-dependent but exhibits a concentration dependence at the same time. This opens up the possibility to use the OAM interferometer as a concentration sensor. Such measurements are performed for sodium chloride and glucose solutions, yielding a high resolution and agreeing with literature.*

## 4.1 Setup of an Orbital Angular Momentum Interferometer

Figure 4.1 depicts a schematic of the OAM interferometer to provide an overview. The broad concept is explained here and individual components are discussed in depth subsequently. The interferometer is placed on an air-balanced laser table (*Melles Griot*, Carlsbad, California, USA). The spiral phase plate (SPP), as well as the cylindrical lens (CL), are the two essential components distinguishing OAM interferometry from conventional interferometry (cf. Figure 2.11). A 532 nm continuous wave laser emits a fundamental Gaussian mode. Next, a

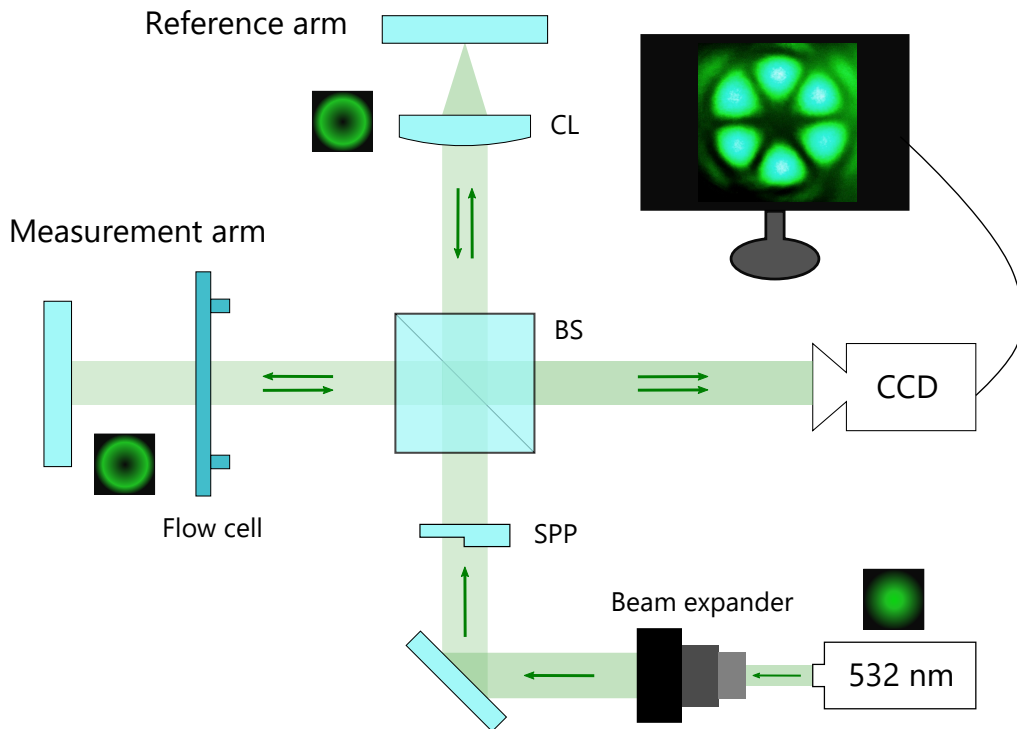


**Figure 4.1: Schematic of the interferometer setup.** In comparison to the basic Michelson interferometer (Figure 2.11), additional components in form of a spiral phase plate (SPP) and a cylindrical lens (CL) are added. The beam expander is crucial in order to fully illuminate the SPP for generating LG modes. The reference arm is guided through a CL, which inverts the helicity of the OAM beam. In the other arm, a flow cell containing the liquid sample is placed. A representative experimental interference pattern detected by a CCD camera is shown in the upper right. [Adapted from Reference [232]].

beam expander enlarges the beam diameter. The SPP transforms the initial Gaussian mode into a Laguerre Gaussian (LG) mode, giving rise to the beam's OAM. The LG beam is then split into two beams by a beam splitter. These beams make up the two so-called arms of the interferometer – the reference and the measurement arm. The reference arm contains a cylindrical lens which focuses the beam on the end mirror. This enables turning the helicity of the beam. The liquid sample is placed in a flow cell which is positioned in the measurement arm for refractive index measurements. Both beams are reflected off end mirrors and are brought into interference through spatial overlap in the beam splitter. Finally, a CCD camera detects the resulting interference pattern, which is processed by a home-built evaluation software.

#### 4.1.1 Light Source and Basic Optical Components

The light source is a water-cooled laser 10 W (Verdi V10, Coherent, Santa Clara, California, USA) which emits a continuous wave with a wavelength of  $\lambda = 532$  nm. All measurements are performed with 50 mW output power. Generally, the laser emits a linearly polarized

Gaussian TEM<sub>00</sub> mode, as derived in Subsection 2.2.3. A pinhole and a lens (*Thorlabs GmbH*, Newton, New Jersey, USA) are used for mode cleaning to filter out higher order modes before the beam enters the interferometer. Standard laser mirrors (*Thorlabs*), optimized for  $\lambda = 532\text{ nm}$ , guide the beam. Before entering the interferometer, the beam diameter is widened by a beam expander (*Thorlabs*) in order to fully illuminate the SPP, which helps to achieve a clean LG mode after passing the SPP. The interferometer itself is encapsulated in an acrylic glass box in order to minimize air fluctuations and, therefore, improve thermal stability. A 50-50 beam splitter (*Thorlabs*) separates the beam into two beams of equal intensity. The end mirrors allow for precise adjustments to overlap the individual beams. After being combined again in the beam splitter, the beams are guided to a *Canon Mark IV* CCD Camera (*Ōta*, Japan). Additional gray filters optimize the intensity incident on the camera.

### 4.1.2 Spiral Phase Plates

The spiral phase plate is the heart of the setup, since it transforms the incoming Gaussian mode into the LG mode and gives rise to the OAM of the beam. As mentioned earlier, LG and OAM beams refer to the same beam in this work. The SPPs discussed in this work consist of fused silica glass and are kindly provided by Dr. Michael Fedoruk (*Vortex Photonics*, Munich, Germany).

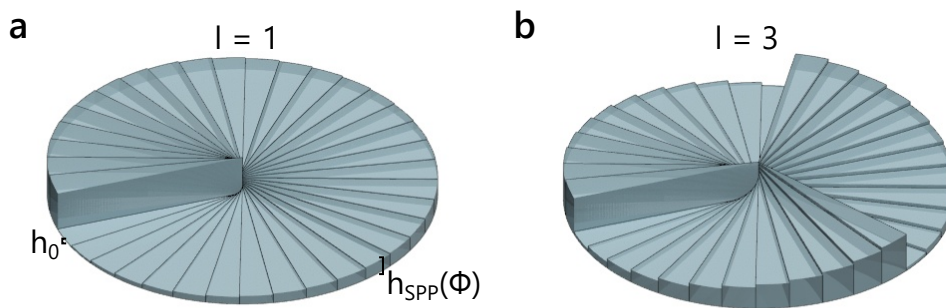


**Figure 4.2: Spiral phase plate.** A Gaussian mode passing through an SPP is transformed into an LG mode, containing OAM. **(a)** The SPP has a single shifting section, generating OAM beams with  $l = 1$ . The minimum height  $h_0$  and the total height  $h_{\text{SPP}}(\phi)$  are indicated. **(b)** The SPP has three shifting sections and thus creates OAM beams with a topological charge  $l = 3$ .

SPPs can be visualized as a spiral stair case with small steps arranged in a circular manner. Figure 4.2 a shows a schematic of an SPP generating OAM beams with a topological charge  $l = 1$ . The minimum height of the SPP is  $h_0$  and the total height is given by  $h_{\text{SPP}}(\phi) = h_0 + h_s(\phi)$ , where  $\phi$  is the azimuthal angle. Depending on the lateral position where the beam passes through the SPP, the beam transverses a varying thickness of glass and is therefore delayed differently. Across the azimuthal angle  $\phi$ , a phase shift  $\Phi(\phi, \lambda)$  with respect to the initial mode ranging from 0 to  $2\pi$  is induced in the beam. Thus, each SPP is designed and

fabricated to generate OAM beams for exactly one specific incident wavelength  $\lambda$ . Above a threshold of 32 individual steps, an SPP has a conversion efficiency comparable to a continuous smooth surface.<sup>138,140</sup> The SPPs used in this work have 64 steps and are thus treated as a continuous spiral (cf. Figure 2.17). The phase shift  $\Phi(\phi, \lambda)$  induced by an SPP with  $l = 1$ , as a function of the azimuthal angle  $\phi$  and the wavelength  $\lambda$ , is given by

$$\Phi(\phi, \lambda) = \frac{2\pi}{\lambda} \left( \frac{\phi}{2\pi} h_{s,\max}(n_{\text{SPP}} - n_0) + h_{s,\max}n_0 + h_0n_{\text{SPP}} \right), \quad (4.1)$$

where  $n_{\text{SPP}}$  is the refractive index of the SPP and  $n_0$  is the refractive index of the surrounding medium.  $h_{s,\max} = h_s(2\pi) = h_{\text{SPP}}(2\pi) - h_0$  is the maximum height of the SPP without the base  $h_0$ .

In Figure 4.2b, the SPP has three individual shifting sections, generating an OAM beam with a topological charge  $l = 3$ . For SPPs generating higher topological charges, the number of shifting sections needs to be taken into account and the azimuthal angle  $\phi$  has to be exchanged by  $\phi = \phi_1 \cdot l \pmod{2\pi}$ .

### 4.1.3 Turning Helicity

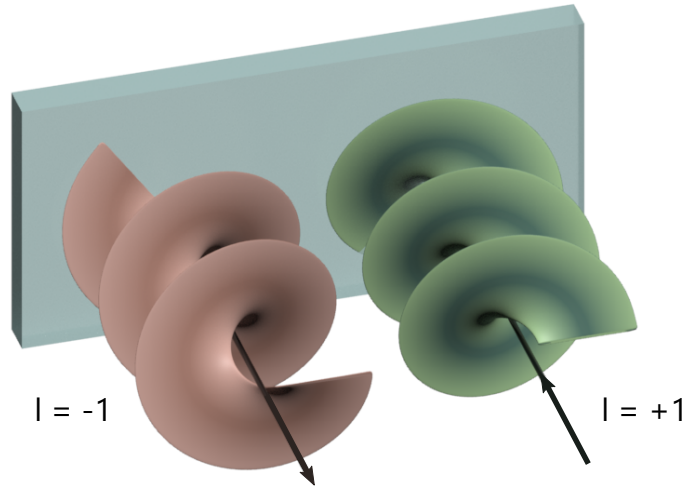


**Figure 4.3: Turning the helicity of an OAM beam.** The optical system, consisting of a CL and a mirror, turns the helicity. An incoming OAM beam with  $l = +1$  is transformed into an OAM beam with  $l = -1$ .

As discussed in Subsection 2.2.3, OAM beams have a specific direction the helix is spiraling around. In order to generate a specific interference pattern, it is necessary to interfere two OAM beams with opposing helicity. The helicity of an OAM beam can be inverted by multiple approaches, for example by using a Dove prism<sup>233</sup> or a CL and a mirror.<sup>205,232,234</sup> A CL mirror system is chosen in this work, i.e., a mirror is placed in the focal point of the CL.

This combination of CL and mirror transforms every point of a 2D image to its mirror point in a Cartesian coordinate system in 2D, i.e., point symmetry is applied. Therefore, in general this configuration inverts the helicity of incoming OAM beams. [Figure 4.3](#) indicates the flip in helicity for the OAM beam going through a CL mirror system. An incoming beam with topological charge  $l = +1$  (green) will be returned as an OAM beam with topological charge  $l = -1$  (red).

## 4.2 Determination of the Interference Pattern Rotation

The two OAM beams with opposing helicity give rise to the aforementioned interference pattern. Upon a change in the optical path in the interferometer, this interference pattern experiences a rotation around the azimuthal angle, which is explained in detail here. This rotation can be quantified and then provides insights on the changes in the measurement arm. It is assumed that no phase change is introduced to the beam of the reference arm, so all phase shifts can be directly related to a change in the measurement arm and the sample which is placed there.

### 4.2.1 Daisy Flower Interference Pattern

The interference pattern created by two interfering OAM beams with opposing helicity resembles a daisy flower (cf. [Subsection 2.2.4](#)). More specifically, this pattern results from the azimuthally alternating constructive and destructive interference of the helical beams. The number of flower petals in the interference pattern is twice the topological charge  $l$ . An increase in the phase singularity in the center is also observed for higher  $l$ . [Figure 4.4](#) shows various experimentally obtained OAM beam modes along with the corresponding interference patterns and compares them to respective simulations. Four different SPPs are presented and a schematic drawing of the respective SPP is always depicted on top. The experiments agree very well with the simulated data.

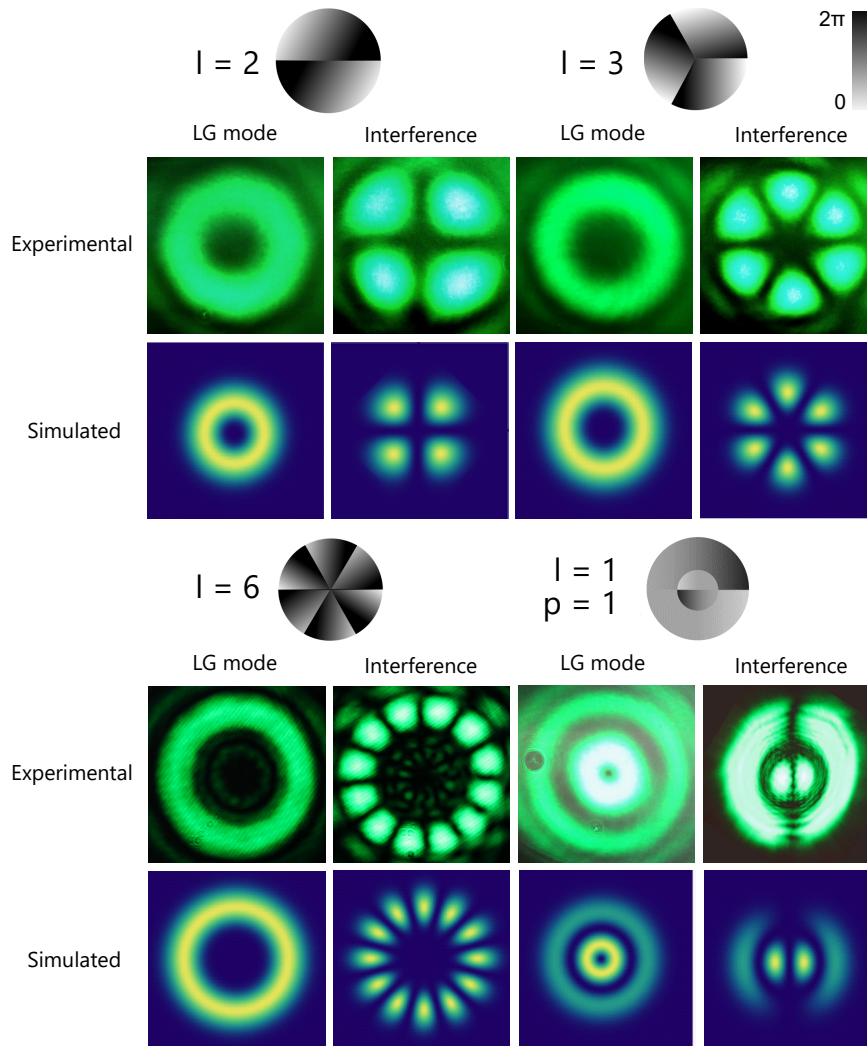


**Figure 4.4: OAM beams and interference patterns for various SPPs.** Beams with different topological charges  $l$  and radial mode indices  $p$  are shown. The LG mode of a single beam is shown with the corresponding interference pattern to the right of it. The upper row shows the experimentally obtained images and simulations are shown below.  $p = 0$  for all modes unless specified otherwise. [Adapted from Reference [133]].

For an enhanced visualization of the interference of two OAM beams, [Figure 4.5](#) shows 3D models of such OAM beams with opposing helicity and how they interfere with each other. The beams are shown for four different points in time. In this case, the green beam is fixed in space and the red beam is shifted along the optical axis. As one of the OAM beams experiences a phase shift, the point of constructive interference of the two beams rotates around the azimuthal angle. This type of phase shift is precisely induced by a change in the measurement arm. Since only the parts of constructive interference are visible in the interference pattern, the flower petals in the interference pattern appear to rotate around the azimuthal angle over time.

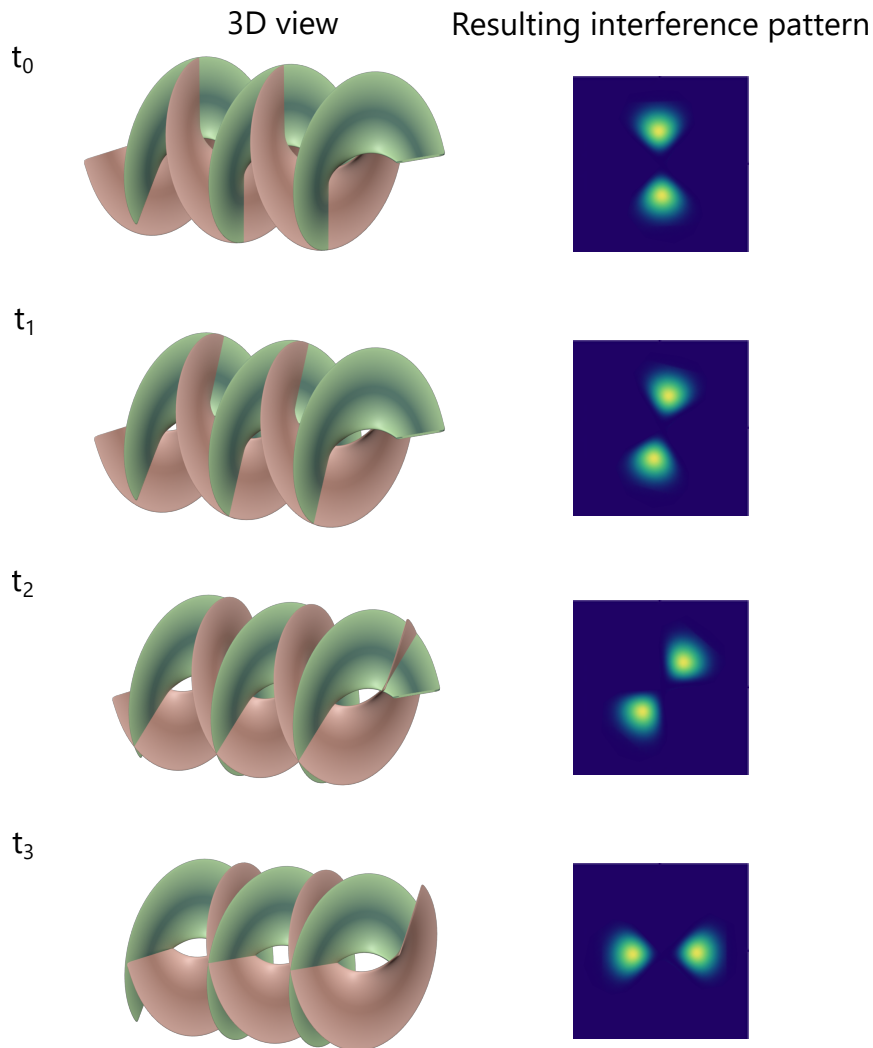


**Figure 4.5: Phase shifts leading to an interference pattern rotation.** When one of the OAM beams experiences a phase shift over time, the position of constructive interference is turned, causing an apparent rotation of the interference pattern. 3D models of the two interfering beams are shown on the left and the resulting interference pattern on the right, for four different points in time.

## 4.2.2 Evaluation Software

In order to analyze this rotation, it is necessary to quantify the movement of the petals. The CCD camera records videos of the rotating interference pattern. A home-built evaluation software was developed to automatically quantify the rotation angle for each frame individually. This was mainly developed by Lucas Fochler and can be reviewed in detail in [Reference \[133\]](#). The program is written in C++ and largely based on the *OpenCV* package.

The individual steps of the evaluation process are depicted in [Figure 4.6](#). Firstly, an image frame from the measured video ([Figure 4.6 a](#)) is segmented with an user-defined threshold ([Figure 4.6 b](#)). This is done in order to filter out noise to obtain clear, distinguishable intensity maxima. For each of the obtained maxima, the “center of mass” is determined. This approach

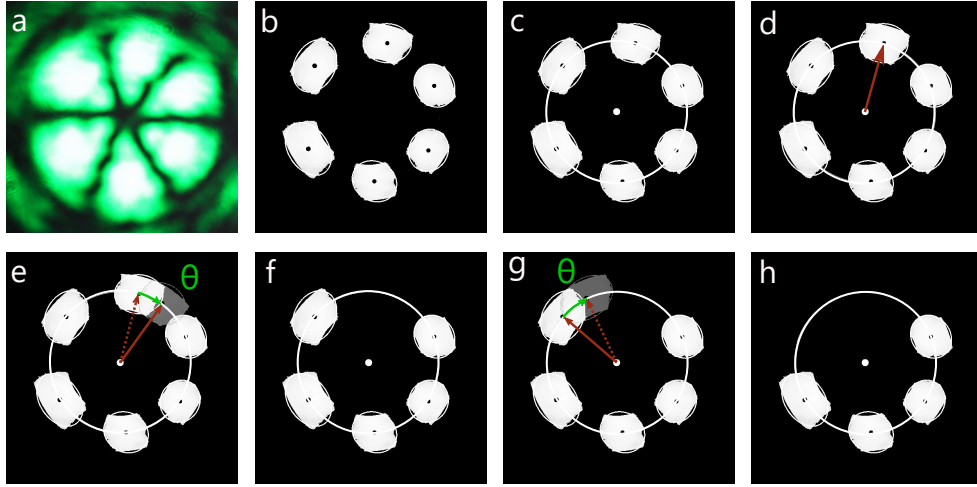


**Figure 4.6: Evaluation software calculating the rotation angle for each acquisition frame.** (a) Example frame from the acquired video. (b) The original image is segmented according to a threshold value and is translated into a black and white image since only the intensity is relevant. (c) From the thereby determined maxima of intensity, the overall center of the interference pattern is calculated and a circle is plotted around it. (d) From the center, a vector is determined pointing to the center of mass of the maximum with the absolute highest intensity value. (e) The rotation of this vector is determined to the subsequent frame. (f) This maximum is not considered anymore and eliminated. (g) Again, the maximum with the absolute highest intensity value is considered and in the same way as before the rotation angle is calculated. (h) The maximum is eliminated and the process is repeated until all maxima are considered and their rotation angle are calculated. All obtained angles are averaged and this value represents the rotation angle for this frame.

is chosen as not every petal will have identical dimensions. In Figure 4.6 c it can be seen that the next step includes the calculation of the center of these individual centers of mass. By averaging the distance of the individual maxima to the obtained common center, a radius value can be calculated. A circle with the respective center and radius is added next in the evaluation of this frame. Next, a vector pointing to the center of mass with the highest intensity in the frame is extracted (Figure 4.6 d). This is repeated for the subsequent frame and in Figure 4.6 e the definition of the angle in between the two vectors of subsequent frames is indicated. It is quantified using vector calculus. Figure 4.6 f depicts that this center of mass is “removed” after the angle is determined. The same process is repeated for the petal with the next highest intensity until the rotation angle for all maxima is calculated (Figure 4.6 g and Figure 4.6 h). From the angles obtained individually for each intensity maximum, an average is retrieved, thereby leading to a very robust determination of the overall change in rotation angle  $\Delta\theta_{\text{rot}}$  of the entire interference pattern. The frame rate of the acquisition limits the temporal resolution. If the interference pattern is rotated by an angle of  $\frac{360^\circ}{2l}$ , it will be identical to an interference pattern that was not rotated at all. If this is the case, the rotation angle  $\theta_{\text{rot}}$  cannot be determined. Therefore, the rotation angle  $\theta_{\text{rot}}$  needs to be  $< \frac{360^\circ}{2l}$  between two consecutive images. In this work, the camera operates at a frame rate of 25 fps, and refractive index changes in the sample are only introduced slowly over long



timescales in the measurements. Therefore, the above mentioned effect can be ruled out to play a role in the measurements.

### 4.2.3 Resolution Limit

The limiting factor to the resolution of the interferometer is the noise. Changes smaller than the rotation angle  $\Delta\theta_{\text{rot}}$  the interferometer experiences when no measurement is running, cannot be resolved. Therefore, it is necessary to address and determine the fluctuations within the signal to quantify the highest possible resolution. In order to determine the noise level, the measurement was started without any sample present. Figure 4.7 shows the rotation angle measured over time. The measurement is conducted with a frame rate of 25 fps and a over a total time of 5 min. It is clearly evident that the fluctuations take place on two different time scales – a slow one on the order of minutes and a fast one on the order of the acquisition frame rate.

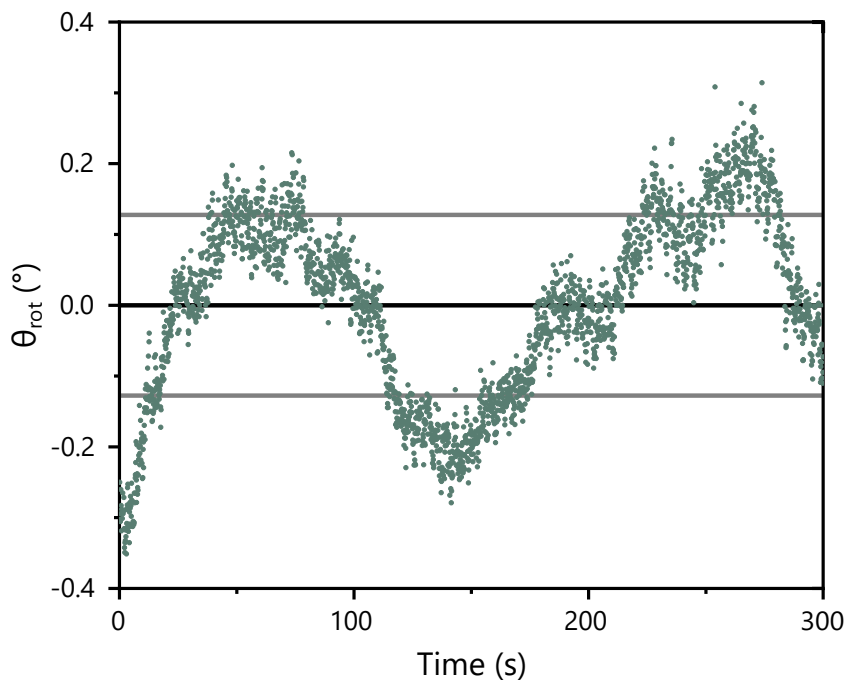


**Figure 4.7: Fluctuations of the rotation angle over time.** The rotation angle is determined for every frame, which were acquired at a frame rate of 25 fps, for a measurement time of 5 min. Each point represents an individual frame. The average angle over time is defined as  $\theta_{\text{rot}} = 0^\circ$ . From this average, the standard deviation (gray lines) amounts to  $0.128^\circ$ . [Adapted from Reference [232]].

From Figure 4.7 the standard deviation of the slow fluctuation component of the signal is calculated at  $\sigma_{\text{slow}} = 0.128^\circ$  (gray bars) with respect to the average angle set to zero. The slow component on the order of minutes is most likely to originate from environmental influences in the laboratory, due to temperature and flow fluctuations in air. The laminar flow hood

embodying the laser table has a temperature accuracy of  $0.1\text{ }^{\circ}\text{C}$ . As seen later in Section 4.3, the interferometer is orders of magnitude more sensitive to changes in temperature.

To visualize the faster time scale more clearly, it is separated from the slow time scale by considering the relative fluctuation taking place from frame to frame in Figure 4.8. These values were acquired by subtracting the rotation angle values from the preceding frame. This fast component results from noise in the image acquisition itself. The standard deviation of this component is  $\sigma_{\text{fast}} = 0.031^{\circ}$  and therefore, an order of magnitude smaller than for the slow component  $\sigma_{\text{slow}}$ .

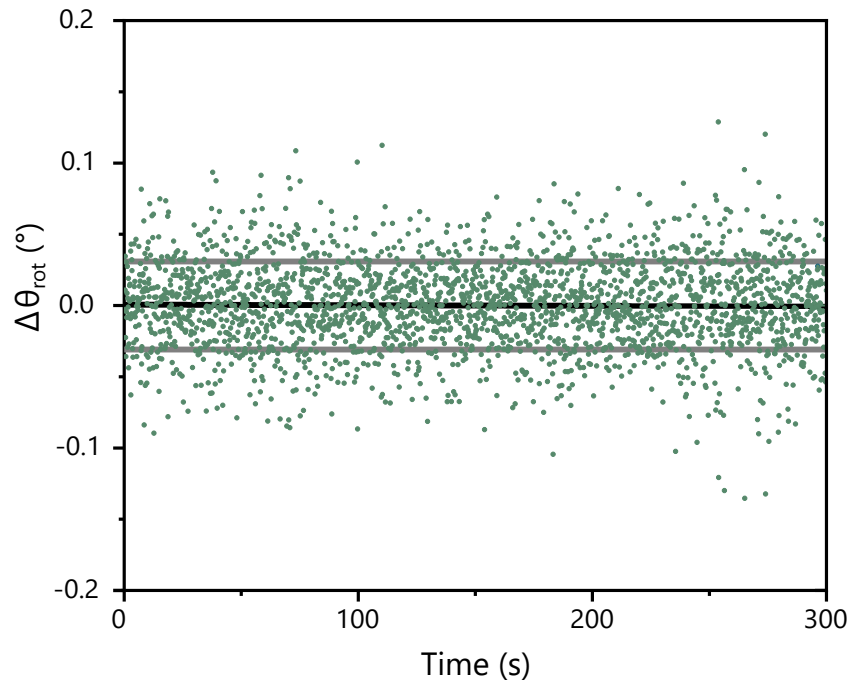


**Figure 4.8: Fluctuations of the rotation angle from frame to frame.** The difference in the rotation from frame to frame from Figure 4.7 is given. Each rotation angle is subtracted from the subsequent measurement point to acquire the change in the rotation angle. Again, the average angle over time is defined as  $\theta_{\text{rot}} = 0^{\circ}$ . From this average, the standard deviation (gray lines) is  $\sigma_{\text{fast}} = 0.031^{\circ}$ . [Adapted from Reference [232]].

For the purpose of gaining more insight on the significance of the fluctuations, the data presented in Figure 4.7 is Fourier transformed, yielding a spectrum with peaks at three distinct frequencies (see Figure 4.9). The CCD camera's acquisition rate of  $0.04\text{ Hz}$  can be seen in the shoulder of the peak at  $0.006\text{ Hz}$ . According to Sampaio *et al.*,<sup>235</sup>  $0.2\text{ Hz}$  is the lowest natural building frequency, matching our data very well. The specific building properties strongly impact such vibrational frequencies, as well as other environmental factors, such as wind. Considering the number of stories of the Nano Institute, in which the experiments were conducted, the measured frequencies match theoretical predictions. Also, buildings with fewer stories usually span a wider range of frequencies,<sup>236</sup> therefore, the last visible peak at  $0.51\text{ Hz}$  may also be regarded as a building vibration.

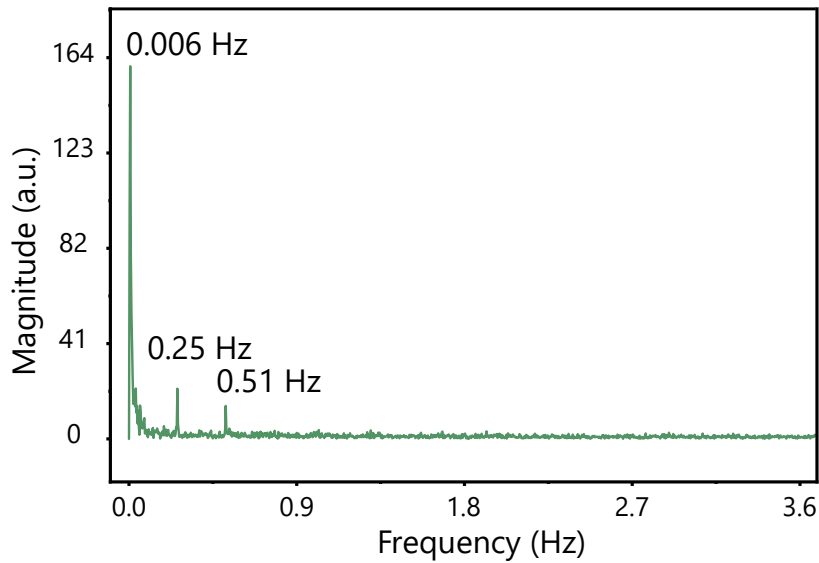


**Figure 4.9: Fourier transformation of the rotation angle fluctuation.** A Fourier transformation of the data presented in Figure 4.7 results in the shown Fourier spectrum. Three peaks at 0.006 Hz, 0.25 Hz and 0.51 Hz can be clearly identified. [Adapted from Reference [232]].

The maximum angular resolution of  $\sigma_{\text{slow}} = 0.128^\circ$  is determined by the standard deviation of the signal in Figure 4.7 from the fluctuations perceived with this interferometer. According to Equation 2.19, this corresponds to a resolution of  $2.84 \cdot 10^{-7}$  RIU (refractive index units). In the following sections, this will be considered as the resolution limit of the OAM interferometer.

### 4.3 Measuring Temperature With Twisted Light

On hot summer days, the air above hot objects, such as cars, in the Sun becomes blurry. This effect is referred to as a heat haze and is caused by the impact of temperature on the refractive index of air. Precisely this effect yields the possibility to measure temperature changes with an OAM interferometer. The change in refractive index causes a phase shift in the OAM beam and thereby causes a rotation of the interference pattern. Thus, temperature can be measured and monitored with the interferometer.

#### 4.3.1 Measurement Conditions

##### Flow Cell and Sample

A liquid flow cell (*Suprasil*<sup>®</sup> glass, *Starna GmbH*, type 45-Q-2, Pfungstadt, Germany) is mounted in the measurement arm of the interferometer, to provide a reservoir for the liquid sample. *Suprasil*<sup>®</sup> glass is chosen, since this is transparent for the laser wavelength at

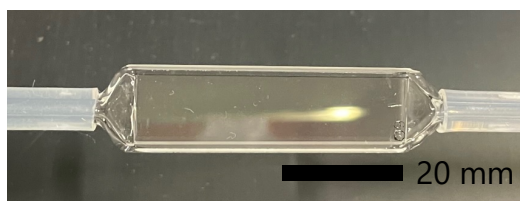


**Figure 4.10: Flow cell for liquid samples.** A quartz glass flow cell (*Suprasil*®) with a channel thickness of 2 mm is used. The flow cell is 45 mm long.

532 nm. This specific glass has a relatively high thermal conductivity and a negligible thermal expansion coefficient. The channel thickness of the flow cell is 2 mm, its width is 12.5 mm and it is 45 mm long. The glass thickness amounts to 1.25 mm. It was placed slightly tilted in the beam path to avoid back reflections disturbing the interference pattern. [Figure 4.1](#) indicates the position of the flow cell and a photograph of the flow cell is provided in [Figure 4.10](#).

The sample, double distilled water (ddH<sub>2</sub>O) (purifying system *Milli-Q*®, VWR, Radnor, Pennsylvania, USA), containing less than 5 parts per billion foreign matter) is first heated up externally to 27 °C in a sonication bath. The heated water is then injected into the flow cell through microfluidic channels and observed while cooling down back to room temperature. During the measurement, the channels are sealed and no flow is present in the flow cell.

### Data Acquisition

An SPP to generate OAM beams with a topological charge of  $l = 3$  is chosen. Heating up a sample externally and then letting it cool down to room temperature is beneficial, since this natural cooling provides stable, slow and small changes in temperature, without requiring any disturbing components such as pumps or temperature controllers.

While the sample temperature decreases, the refractive index of the medium changes. As a result a phase shift is introduced in the measurement arm, causing the interference pattern of the two helical beams to rotate. From this rotation, it is possible to draw back conclusions about the change in refractive index  $\Delta n$  ([Equation 2.19](#)). It is necessary to measure and monitor the temperature of the sample simultaneously, in order to determine a specific change in temperature and relate this to the rotation angle  $\theta_{\text{rot}}$ . For this endeavor, the identical IR camera as described in [Chapter 3](#) conducts the temperature control measurements. The above described flow cell is chosen due to its large surface area, which provides a significant measurement surface for the IR camera. *Suprasil*® glass is not ideally transmissive in the mid-IR region, which is the wavelength range of thermal emission of objects around room temperature. The temperature measured by the IR camera is mainly expected to stem from the glass surface of the flow cell, which is warmed up by the sample. The glass wall of

the flow cell exhibits a low thickness and a relatively high thermal conduction coefficient. Thus, it is justified to assume that even if the absolute temperature values are not exact, the measured change in temperature can be used as a control measure. However, it should be kept in mind that the IR camera is not the ideal method to measure the temperature of solutions.

Figure 4.11 shows the positioning of the IR camera in the interferometer measurement arm. The IR camera is placed diagonally on top of the beam for simultaneous measurements. An example IR image from the flow cell is provided. In this image, the laser is turned on. It is apparent that the laser itself, due to the low operating power, does not heat up the water at the measurement position, which is crucial in these temperature measurements. The flow cell with the connecting channel on the left can be clearly seen. The region of interest (ROI) indicates the OAM beam position on the flow cell. From this image it is evident that the temperature is hottest in the center of the flow cell, where the warm ddH<sub>2</sub>O is injected. However, since the interferometer and the IR camera measure the same position, this inhomogeneous temperature distribution does not affect the measurement.

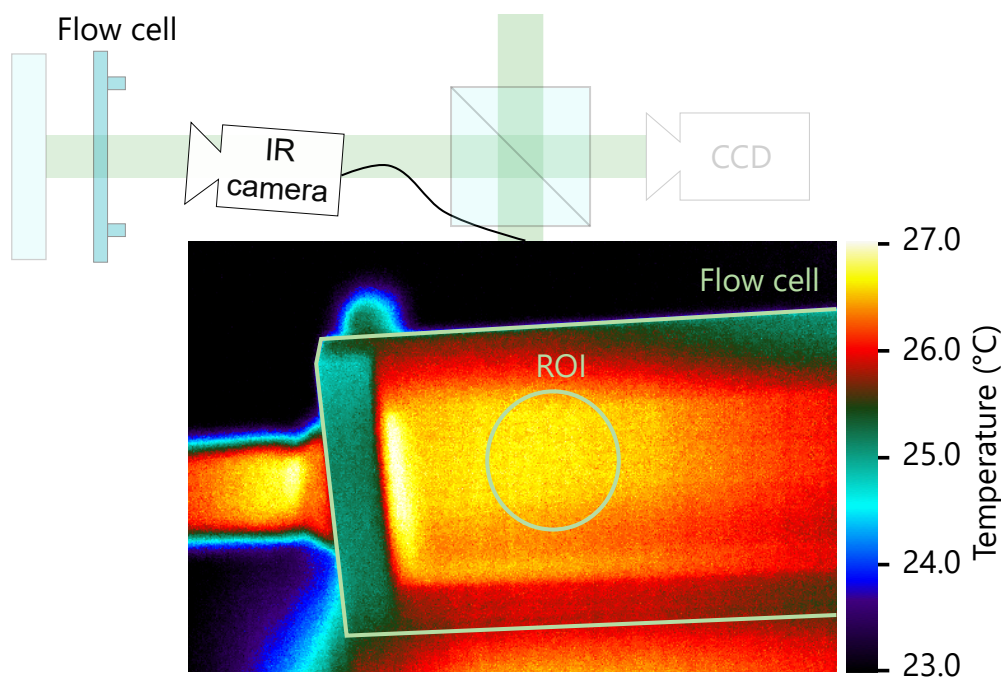


**Figure 4.11: Temperature sensing of the flow cell with IR camera.** The position of the IR camera within the interferometer is depicted on the upper left hand corner. An exemplary IR image is shown, with an indication of the edge of the flow cell and the ROI, which is the measurement position of the laser of the OAM beam. The color bar correlates the specific temperatures. [Adapted from Reference [232]].

### 4.3.2 Temperature Sensing Results

Figure 4.12 a shows the resulting temperature curve measured by the IR camera, as well as the rotation angle of the interference pattern over time. Both data sets are plotted against the same  $x$ -axis which allows relating the temperature axis to the rotation axis. The change in the rotation angle  $\Delta\theta_{\text{rot}}$  is directly proportional to the change in refractive index  $\Delta n$  (Equation 2.19). Furthermore, the change in refractive index can be directly correlated to a change in temperature and a linear dependence can be presumed. This can be deduced from the significant overlap of the two curves and literature.<sup>237</sup> Thus, the measured rotation angle translates into the change in temperature. When plotting both curves together, the proportionality factor relating the rotation angle to the change in temperature can be defined. For the ddH<sub>2</sub>O sample, the optical path through the sample of 4 mm (the beam passes twice through the flow cell) and the SPP with  $l = 3$ , a temperature change of 1 °C results in a rotation angle change of approximately  $\Delta\theta_{\text{rot}} = 136.5^\circ$ . When converting the measured change in rotation angle  $\Delta\theta_{\text{rot}}$  into a change in refractive index using Equation 2.19, the change of refractive index per change in temperature is  $\frac{\Delta n}{\Delta T} = -3.0 \cdot 10^{-4} \text{ RIU } ^\circ\text{C}^{-1}$ .

Both the measured rotation angle and the temperature simultaneously follow a smooth mono-exponential decay. This decay of the temperature of the ddH<sub>2</sub>O sample confirms the expected Newton cooling process (Subsection 2.1.1). Notably, the rotation angle curve is extremely smooth, indicating a steady and robust measurement. As mentioned earlier, the glass flow cell is not the ideal thermal emitter and thus the camera actually measures the warming of the glass surface, due to the injected ddH<sub>2</sub>O sample. Therefore, the measurement conditions are not ideal for the camera and the measured temperature signal  $T$  comprises higher uncertainty than the rotation angle  $\theta_{\text{rot}}$  measurement. A flow cell with a small thickness was chosen to obtain more accurate temperature measurements. For thicker flow cells, the control measurement would become unreliable since the IR camera measures surface temperatures only. Thus, in this measurement specifically, a trade-off between measurement accuracy of the interferometer and the calibration measurement via the IR camera has to be considered.

To effectively determine the temperature resolution of the interferometer, an inset of 10 seconds of this graph is highlighted in Figure 4.12 b. When considering the resolution limit of the rotation angle  $\Delta\theta_{\text{rot}} = 0.128^\circ$  as determined in Subsection 4.2.3, the resulting temperature resolution for ddH<sub>2</sub>O is 890  $\mu\text{K}$ . At this point it is worth mentioning that this resolution is achieved with real-life laboratory conditions, without any specific vacuum appliances. The change in rotation angle  $\Delta\theta_{\text{rot}}$  is directly proportional to the thickness of the flow cell, i.e., the beam path through the sample, as elaborated in Equation 2.19. Thus, by increasing the channel thickness, higher resolutions are possible. The current resolution, however, presents a realistic laboratory measurement that can be implemented into various setups. To compare

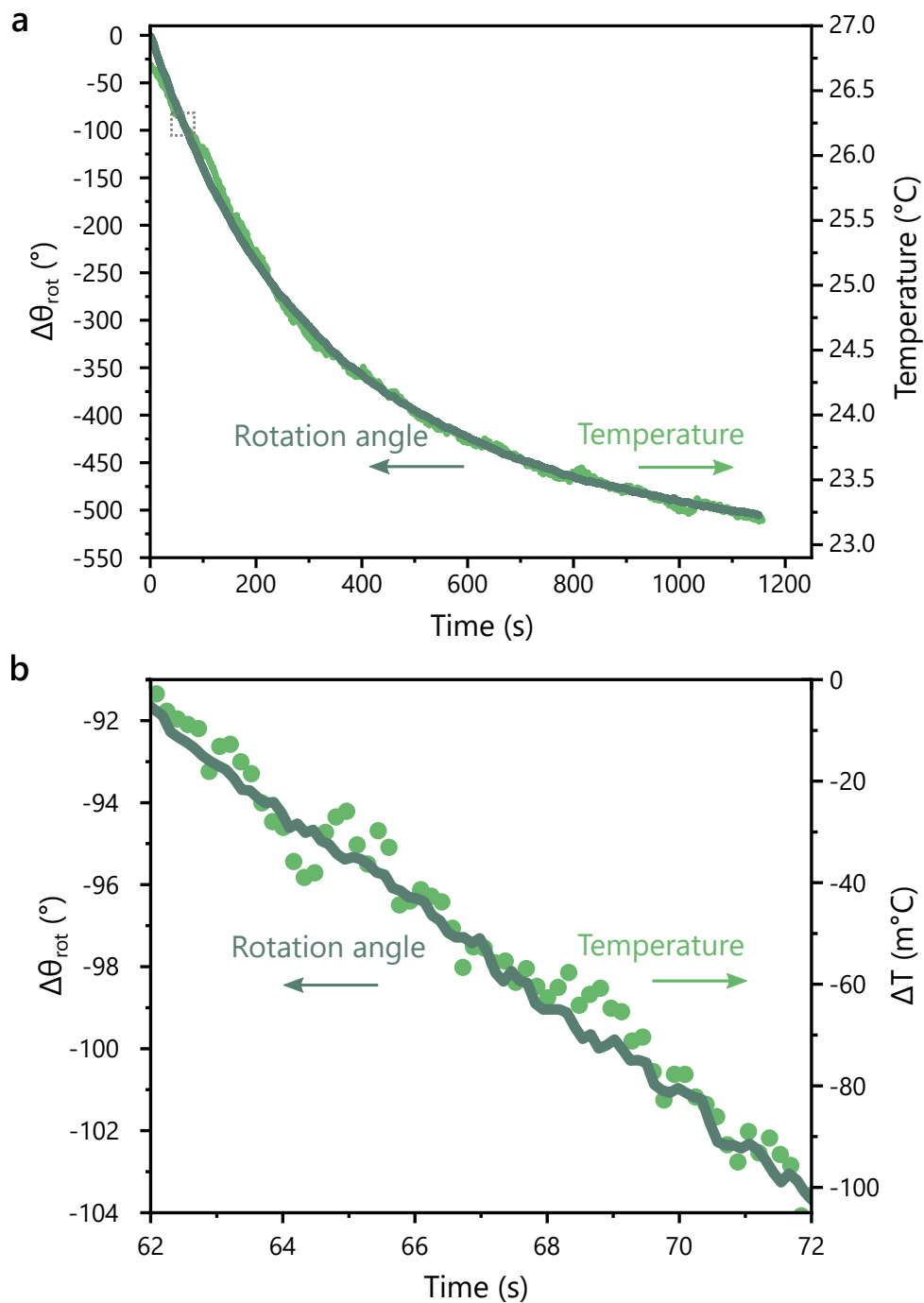


**Figure 4.12: Acquired temperature data.** Measured rotation angle change  $\Delta\theta_{\text{rot}}$  and temperature over time as a sample of ddH<sub>2</sub>O cools down. (a) The dark green curve shows the measured rotation angle change and the light green curve the temperature obtained by the IR camera. The gray box indicates the range which is shown in (b) enlarged. [Adapted from Reference [232]].

the results to literature values, a useful measure is the thermo-optic coefficient  $\frac{dn}{dT}$  for ddH<sub>2</sub>O, which is independent of the path length. An approximation for this value is already given above by the proportionality factor scaling both data sets. For a more precise mathematical analysis, the data sets are investigated in detail.

### 4.3.3 Determination of the Thermo-Optic Coefficient

The thermo-optic coefficient  $\frac{dn}{dT}$  describes the change in the refractive index relative to a change in temperature for a material. It has been determined for many different materials and studied in great depth and, therefore, a large literature knowledge foundation is present. In order to validate our measurements and method, the thermo-optic coefficient is calculated for the obtained experimental data presented above and compared to the literature.

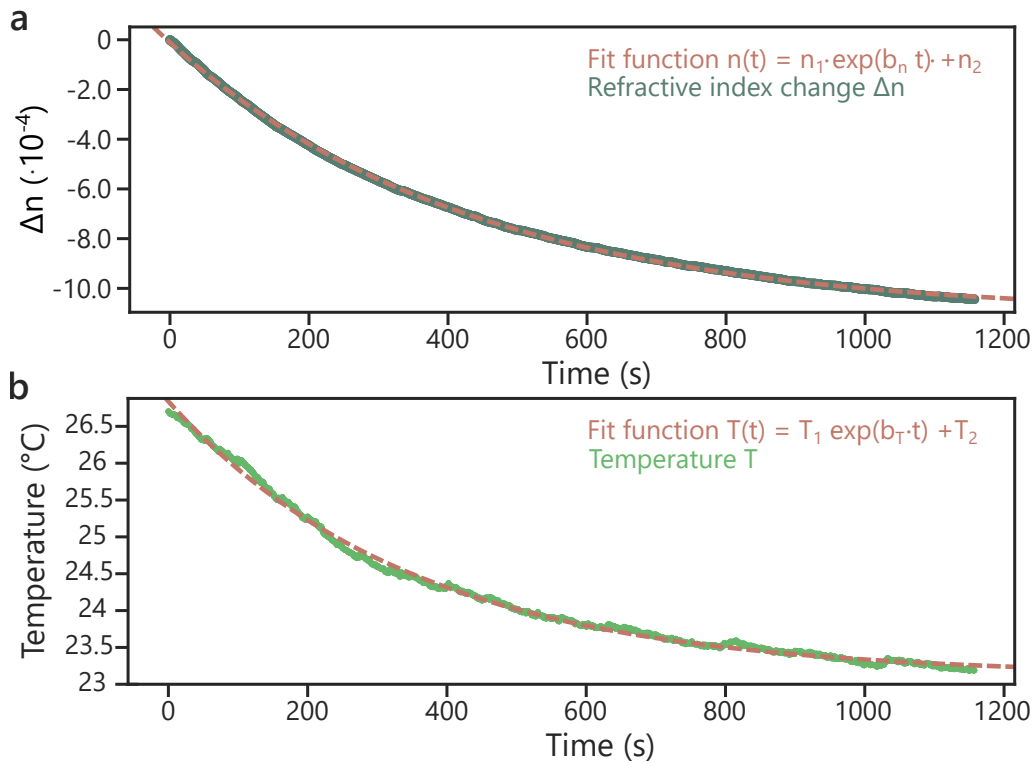


**Figure 4.13: Mono-exponential fits of change in refractive index and temperature data.** (a) The change in refractive index determined from the rotation angle of the interference pattern from the temperature measurement is fitted with a mono-exponential fit. (b) The same is performed for the temperature measurement from the IR camera.

To perform the calculation of the thermo-optic coefficient  $\frac{dn}{dT}$ , the data shown in Figure 4.12 is converted into the change in refractive index  $\Delta n$  (via Equation 2.19).  $\Delta n$  and the temperature are plotted over time in Figure 4.13 and fitted mono-exponentially. The fits for the change in refractive index and temperature achieve  $R^2$  coefficients of 0.9996 and 0.9971, respectively, and thus validate the mono-exponential approach.



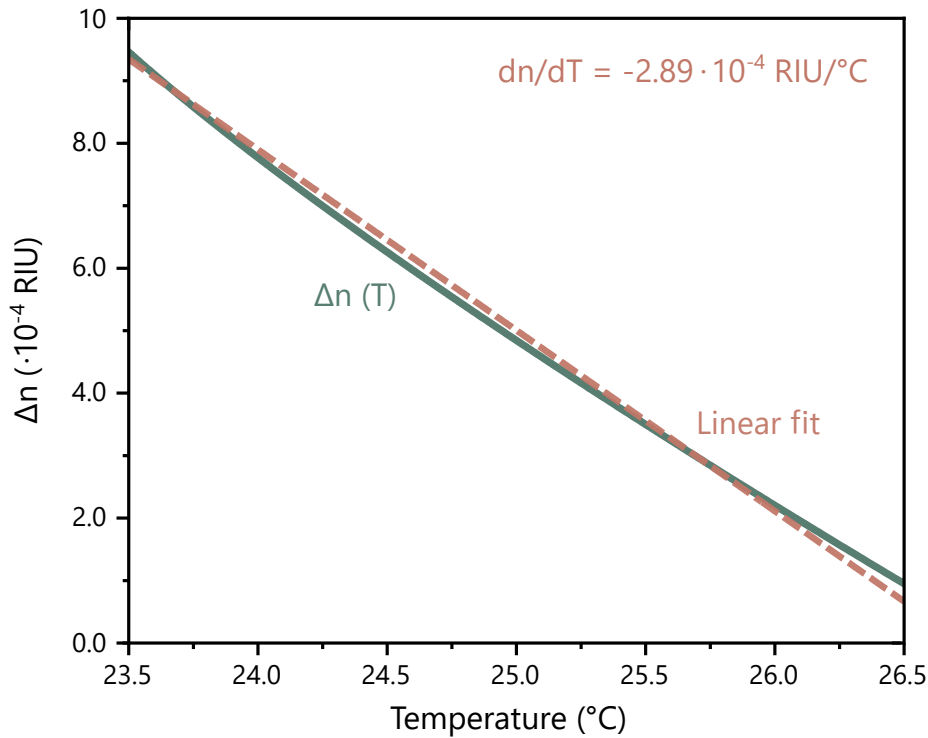


**Figure 4.14: Change in refractive index against temperature.** The values obtained for  $\Delta n$  and  $T$  from the fits in Figure 4.13 can be approximated linearly within the measurement range. The slope of a linear fit is the calculated thermo-optic coefficient for this range. [Adapted from Reference [232]].

Combining both fitted curves from Figure 4.13 allows a representation of the data as shown in Figure 4.14 where the calculated  $\Delta n$  is plotted against the temperature  $T$ . The refractive index  $n$  can only be plotted in terms of a change, since the absolute values cannot be determined by the interferometer. By plotting  $\Delta n$  against  $T$ , the curve  $\Delta n(T)$  can be seen as slightly curved, but within the given measurement range the relationship between  $\Delta n$  and  $T$  can be fitted linearly (dashed line). Thereby, the change in refractive index per unit change in temperature  $\frac{dn}{dT}$ , namely the thermo-optic coefficient can be calculated from the slope of the linear fit.

**Table 4.1: Literature values of the thermo-optic coefficient of ddH<sub>2</sub>O.** The calculated thermo-optic coefficient is compared to four literature values.

	This work	Subedi <i>et al.</i> <sup>237</sup>	Schiebener <i>et al.</i> <sup>238</sup>	Domenegueti <i>et al.</i> <sup>239</sup>	Kim <i>et al.</i> <sup>240</sup>
$\frac{dn}{dT} (10^{-4} \text{RIU}/^\circ\text{C})$	-2.89	-1.85	-2.0	-2.0	-0.8

The resulting calculated thermo-optic coefficient for ddH<sub>2</sub>O is  $\frac{dn}{dT} = -2.89 \cdot 10^{-4} \text{RIU}/^\circ\text{C}$ . This result is compared to literature values in Table 4.1. Importantly, all values are on the same order of magnitude. In all other works, the refractive index was measured by changing the temperature with a lower precision of up to 1 °C (Kim *et al.*<sup>240</sup>). Additionally, other wavelengths were used to measure (Kim *et al.*,<sup>240</sup> Schiebener *et al.*<sup>238</sup>) different temperature

ranges (Domenegueti *et al.*<sup>239</sup>). These varied measurement conditions lead to a variation of  $\approx 1 \cdot 10^4$  RIU/°C within literature already. For Schiebener *et al.*<sup>238</sup> the result is given as a typical result from 12 different literature values. Additionally, one might question the thermo-optic coefficient of the flow cell and, therefore, the impact on the measurement. According to the manufacturer (Starna) the Suprasil® glass has a thermo-optic coefficient ranging from  $9.6 \cdot 10^{-6}$  to  $14.9 \cdot 10^{-6}$  RIU/°C, depending on the temperature range and the wavelength. This is two orders of magnitude below the thermo-optic coefficient of ddH<sub>2</sub>O and, therefore, can be neglected.

To sum up the results presented in this section, the OAM interferometer provides a novel contactless method to detect temperature with  $\mu$ K resolution. By further improving the setup, for example simply by increasing the flow cell thickness, it is possible to enhance the resolution. If a rotation angle resolution of  $0.002^\circ$  as proposed by Verma *et al.*<sup>234</sup> would be achieved, the smallest resolvable temperature would be  $14 \mu$ K. Typically, measurements with mK or even  $\mu$ K accuracy require complicated and costly equipment. IR cameras can measure contactless in mK ranges, however, in order to reliably measure liquids, intricate and costly flow cells with NaCl windows<sup>241</sup> are required, due their IR transmissivity. Furthermore, IR cameras only measure surface temperatures and the OAM interferometer can measure in transmission. In conclusion, the OAM interferometer presented in this thesis provides a robust and elegant method for temperature measurements of transmissive, liquid samples in a contactless manner.

## 4.4 Beyond Temperature: Concentration Measurements

The refractive index of liquids depends on several factors, most importantly on the temperature and concentration.<sup>240,242,243</sup> As the OAM interferometer has proven to be highly sensitive to changes of temperature of a liquid, the principle was extended to measure concentration changes of ionic and non-ionic solutions. The strong advantage of doing this with an interferometer is that this measurement is absolutely non-invasive. From the temperature measurements it is evident that the interferometer beam itself does not warm up the sample. Therefore, when leaving the sample at room temperature, the impact of temperature on the overall change of the refractive index can be ruled out. When changing the concentration of a sample, it can thus be measured by the OAM interferometer due to the thereby induced change in the refractive index causing a rotation of the interference pattern. To ensure the change of concentration does not cause a significant change in temperature, as it may due to the enthalpy of the dissolution of salts, the IR camera was once again used to monitor the temperature in a test experiment and showed that the temperature remained constant for such low concentration changes.

The concentrations of two solutions – aqueous sodium chloride (NaCl) and glucose ( $C_6H_{12}O_6$ ) – are measured. They are chosen because they have different ionic characters, which often dictates the method of choice for concentration measurements, e.g., via electrical conductivity for ions. Moreover, the individual particles are extremely small, making it difficult to determine their concentration via absorption measurements. For all concentration measurements, a flow cell (*Hellma GmbH*, Müllheim, Germany) with a channel thickness and width of 2 mm is used in order to ensure a laminar flow and keep disturbances at a minimum.

#### 4.4.1 Sodium Chloride

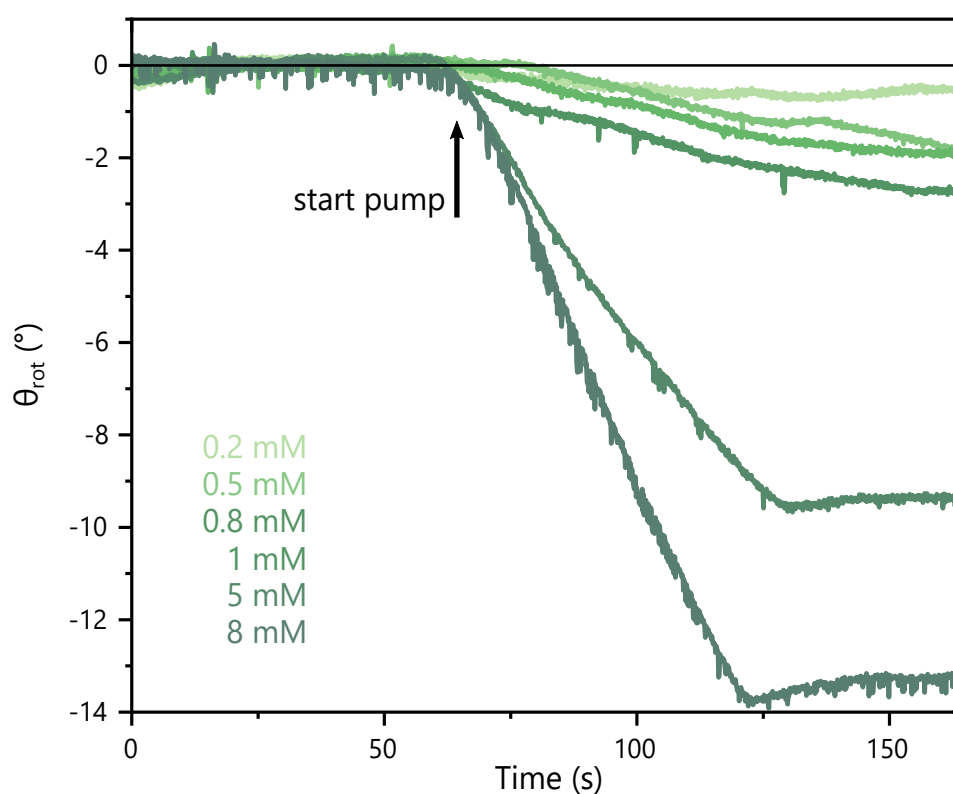


**Figure 4.15: NaCl concentration measurements.** The rotation angle  $\theta_{\text{rot}}$  of the interference pattern versus time is shown for samples with different concentrations ranging from 0.2 to 8 mM. The colors identify the corresponding traces. The arrow indicates the point in time when the syringe pump is started. [Adapted from Reference [232]].

First, the NaCl sample is considered. A dilution series is prepared for NaCl ranging from 200  $\mu\text{M}$  to 10 mM. Pure NaCl (*Sigma Aldrich*) is used without further purification and dissolved in ddH<sub>2</sub>O. Before each measurement, the flow cell is filled with pure ddH<sub>2</sub>O. A syringe pump (*TSE Systems*, Bad Homburg vor der Höhe, Germany) pumps the solution through the flow cell to induce a complete fluid exchange. A rate of 0.9 mL/min ensures laminar flow and minimal disturbances. This avoids the formation of air bubbles and enables a stable series of measurements. An SPP with a topological charge of  $l = 6$  was used.

Figure 4.15 provides the results for the NaCl concentration measurements. The video acquisition starts 1 minute before the syringe pump. In this time before the pump is started, a constant rotation angle  $\theta_{\text{rot}}$  is measured to define the starting point  $\theta_{\text{rot,start}}$ . The plots are shifted such that  $\theta_{\text{rot,start}} = 0^\circ$  for all concentration traces. The initiation of the syringe pump is indicated with an arrow. The slow exchange of the content of the flow cell causes a gradual increase of the NaCl concentration, which can be seen in the rotation of the interference pattern. The higher the final concentration, the steeper the slope of the curve, because the amount of ions present in the flow cell increases faster compared to samples with lower concentrations. After the fluid exchange is completed, the pattern stops rotating and therefore the rotation angle reaches a new, stable plateau. This angle is again measured for 1 min to obtain a new stable plateau value, which is averaged to determine the final interference pattern rotation angle  $\theta_{\text{rot,final}}$ . By subtracting the second plateau value from the first, the change in the rotation angle  $\Delta\theta_{\text{rot}} = \theta_{\text{rot,final}} - \theta_{\text{rot,start}}$  is determined. Concentrations in the mM range are clearly detectable while a 200  $\mu\text{M}$  concentration translates to a rotational angle change of  $\Delta\theta_{\text{rot}} 0.54^\circ$ , which is still explicitly distinguishable but approaching the noise level.

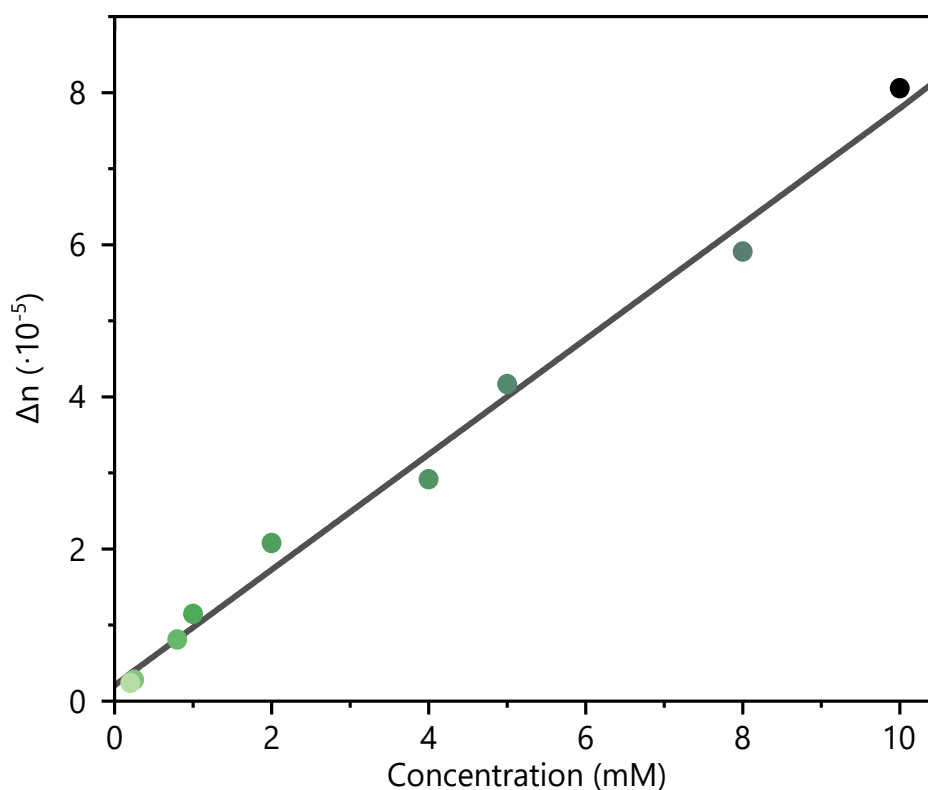


**Figure 4.16: Refractive index dependence on concentration of NaCl.** The determined refractive index change  $\Delta n$  is linearly dependent on the concentration of the NaCl solutions, as confirmed by the applied fit. [Adapted from Reference [232]].

Next, the impact of the NaCl concentration on the refractive index is investigated. Figure 4.16 shows the results. Every performed concentration measurement represents one data point.

More measurement points are found in Figure 4.16 than traces in Figure 4.15, since only a selection of the raw data was presented there for enhanced clarity. The translation of the rotation angle values  $\Delta\theta_{\text{rot}}$  to change in refractive index  $\Delta n$  is performed via Equation 2.19. A linear fit is applied and matches the data, as theoretically predicted.<sup>242,243</sup> Summing up the measurement series for NaCl, it is clearly evident that this interferometer can measure concentration changes below  $10^{-5}$  RIU.

#### 4.4.2 Glucose

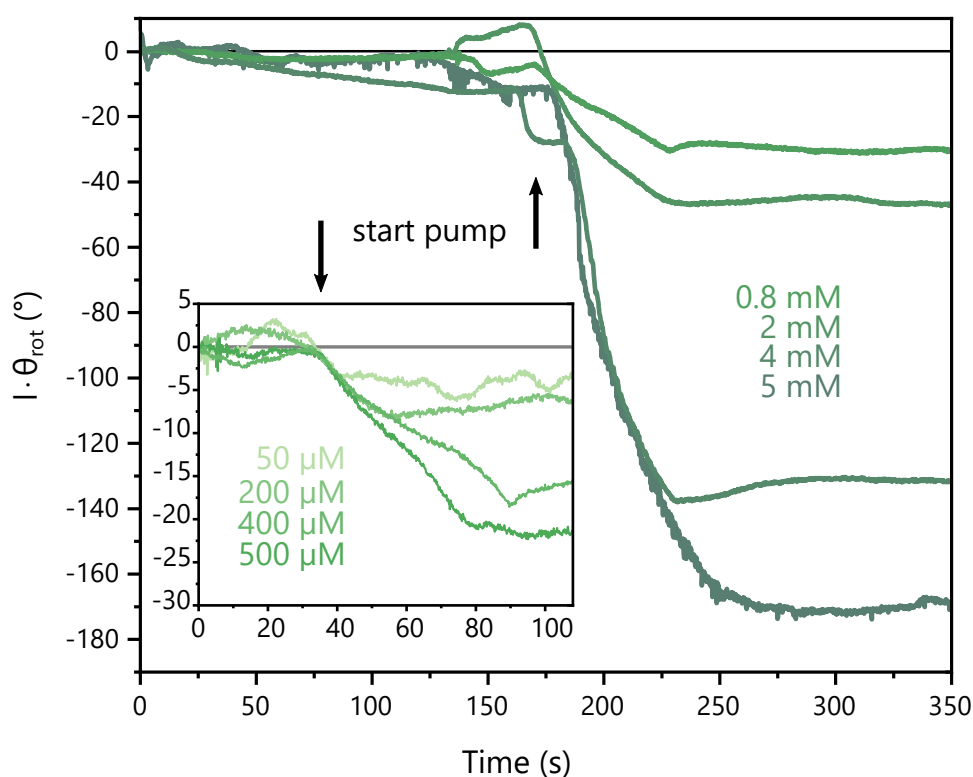


**Figure 4.17: Glucose concentration measurements.** The product of the rotation angle  $\theta_{\text{rot}}$  of the interference pattern and the topological charge  $l$  versus time is shown for samples with different concentrations ranging from 0.8 to 5 mM. An inset shows the concentration values from 50 to 500  $\mu\text{M}$ . The colors identify the corresponding traces. The point in time when the syringe pump is started is indicated. [Adapted from Reference [232]].

Secondly, the glucose solutions are investigated. Glucose is a scientifically highly relevant molecule to measure, as patients suffering from diabetes mellitus have a constant need for monitoring their glucose levels. This illness is a global epidemic and estimated to affect almost 700 million people by 2045.<sup>244</sup> Currently, the blood glucose levels are measured invasively by taking a blood sample or implanting a sensor. Recently, approaches using the ocular fluid<sup>245</sup> have been investigated.

A second dilution series is prepared for glucose, ranging from 50  $\mu\text{M}$  to 5 mM. ddH<sub>2</sub>O and pure D-glucose (*Sigma Aldrich*) are used without further purification. Glucose (C<sub>6</sub>H<sub>12</sub>O<sub>6</sub>) has a significantly higher molar mass (180.156 g mol<sup>-1</sup>) than NaCl (58.44 g mol<sup>-1</sup>), therefore, the dilution series is prepared using lower concentration values. The measurement protocol is identical to the NaCl measurements described above. The resulting rotation angle traces over time are presented in [Figure 4.17](#).

In this measurement series, SPPs with  $l = 3$  and  $l = 6$  were used in order to optimize the balance of gaining a high rotation (for a smaller topological charge  $l$ ) and maintaining a larger number of maxima in order for the evaluation program to calculate a stable mean value for the rotation. Therefore, the y-axis in this figure is now given as the product  $l \cdot \theta_{\text{rot}}$ , to compare measurements performed with different SPPs. The equivalence of using different SPPs is thereby emphasized. The same trend as observed in the NaCl measurements is visible for glucose. The smallest glucose concentration value of 50  $\mu\text{M}$  causes a rotation angle of  $\Delta\theta_{\text{rot}} = 0.55^\circ$ . Again, this is well above the resolution limit of the interferometer, but as seen in [Figure 4.17](#), the measurement becomes more noisy.

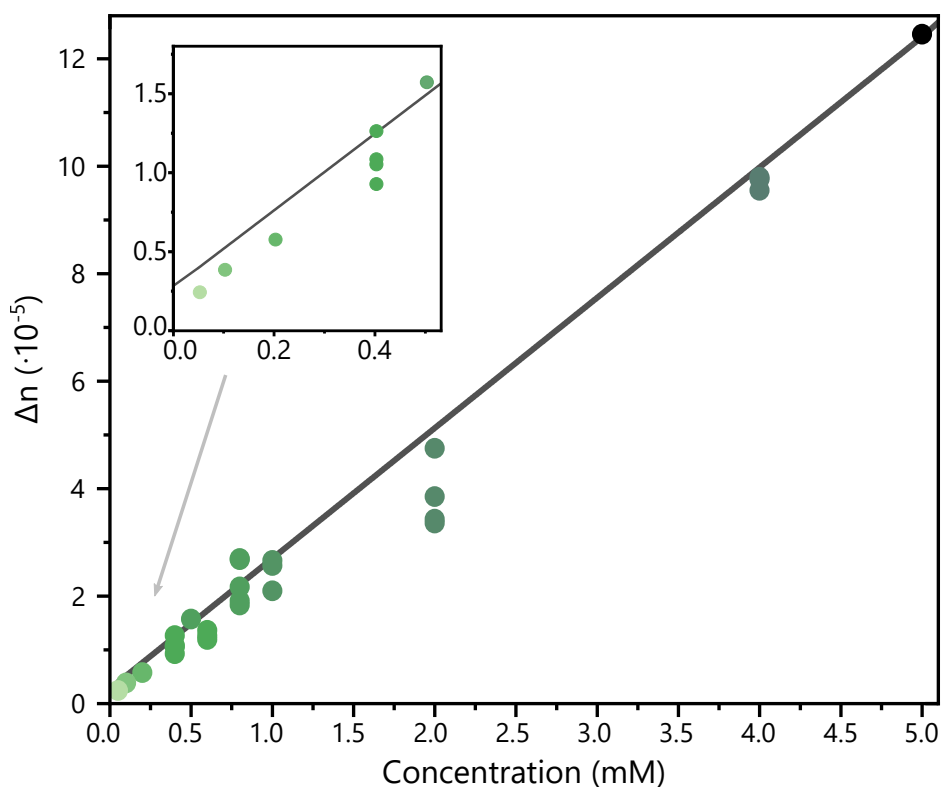


**Figure 4.18: Refractive index dependence on concentration for glucose.** The determined refractive index change  $\Delta n$  is linearly dependent on the concentration of the glucose solution, as confirmed by the applied fit. Smaller  $\Delta n$  values are highlighted in an inset. Multiple data points are acquired for identical concentrations to confirm the reproducibility of the experiment. [Adapted from [Reference \[232\]](#)].

Again, Equation 2.19 was applied to translate the change of refractive index  $\Delta n$  from the measured change in rotation angle  $\Delta\theta_{\text{rot}}$ . These results are shown in Figure 4.18. The linear relationship is unambiguous and indicated by the fit. For the smallest concentration value of  $50\ \mu\text{M}$ , the measured change of the refractive index is  $\Delta n = 2.44 \cdot 10^{-6}$  RIU. Several values following the linear trend in this region confirm the resolution of the interferometer in this case on the order of  $10^{-6}$  RIU. Multiple measurements were repeated up to four times to investigate the reproducibility of the experiment. As evident from Figure 4.18, the individual points for a single concentration reproduce similar  $\Delta n$  values.

#### 4.4.3 Comparison to Literature Values

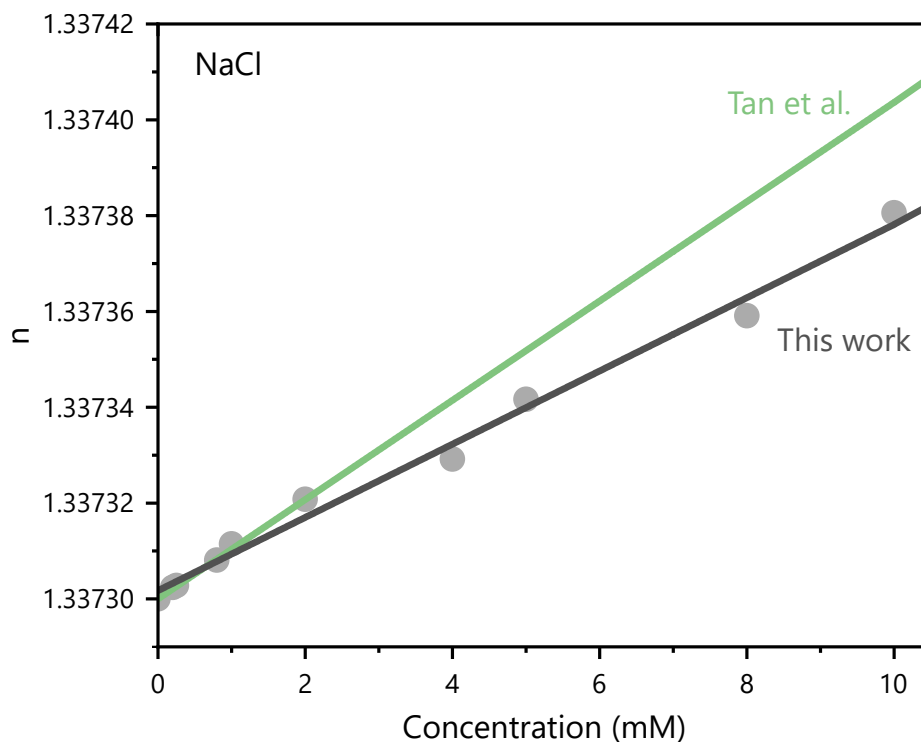


**Figure 4.19: NaCl literature comparison.** The obtained changes in refractive index (Figure 4.16) are plotted again but as absolute  $n$  values. A constant of  $n = 1.3373$  (obtained from Reference [242]) was added for this purpose. Tan *et al.*<sup>242</sup> provide an empirical formula for the dependence of the refractive index  $n$  on concentration for NaCl. Their data is obtained for higher concentration values by a refractometer and extrapolated to the range relevant for this work for comparability. [Adapted from Reference [232]].

The results shown in Figure 4.16 are plotted once again in Figure 4.19. The data points are shown for each measured NaCl concentration along with the earlier described linear fit. Here, instead of  $\Delta n$ , an absolute value for  $n = 1.3373$ , obtained from Tan *et al.*<sup>242</sup> was added to the measured  $\Delta n$  values. Tan *et al.*<sup>242</sup> also measured the refractive index dependence on NaCl concentration and determined an empirical correlation. In this work the authors used

a refractometer with a light source of 589.3 nm to measure NaCl concentrations ranging from 170.6 to 4265.0 mM (1 to 25 w%). This is a similar wavelength as used in this work (532 nm), but the concentration range is significantly higher. The NaCl solutions were prepared in single distilled water, not ddH<sub>2</sub>O as it is the case in this work. Their refractometer claims an accuracy of 0.0001 RIU, which is two orders of magnitude below the here measured resolution. Thus, the measurement parameters vary slightly. The linear trend obtained in these higher concentration ranges was extrapolated to fit our range and is plotted in Figure 4.19. Evidently, the linear correlations obtained once by refractometry and once by OAM interferometry show significant overlap and confirm the validity of OAM interferometry for concentration measurements in the  $\mu\text{M}$  range.

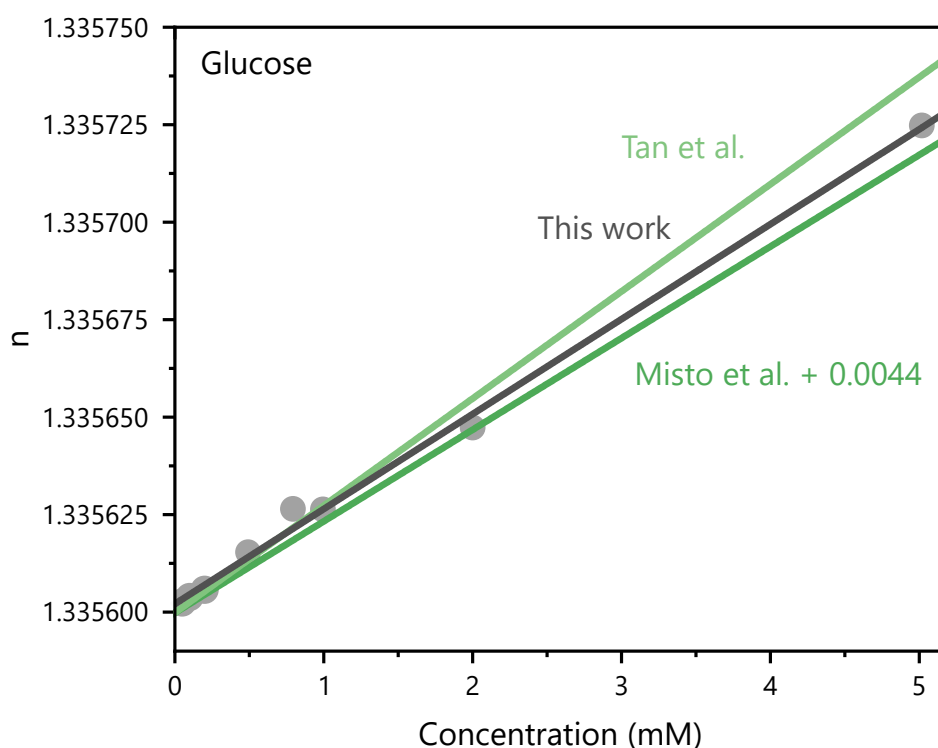


**Figure 4.20: Glucose literature comparison.** The obtained changes in refractive index (Figure 4.18) are plotted again but as absolute  $n$  values. A constant of  $n = 1.3356$  (obtained from Reference [242]) was added for this purpose. Tan *et al.*<sup>242</sup> and Misto *et al.*<sup>243</sup> provide an empirical formula for the dependence of the refractive index  $n$  on concentration for glucose. Their data is obtained by refractometers for higher concentration values and extrapolated to the range relevant for this work for comparability. [Adapted from Reference [232]].

The experimentally obtained trend for the refractive index dependence on the glucose concentrations is also compared to literature values. Here, References [242, 243] provide experimentally measured values, determined by a refractometer. Tan *et al.*<sup>242</sup> measured concentrations in a range of 55.34 to 2767.0 mM (1 to 50 w%) and Misto *et al.*<sup>243</sup> measured a range of 276.7 to 2136 mM (5 to 40 w%). Their empirical formulae are extrapolated to the measurement



range applied in this work and the result is shown in Figure 4.20. For the fit in Misto *et al.*,<sup>243</sup> a constant of 0.0044 is added, since their work measures at a different wavelength of  $\lambda = 525$  nm and at a higher sample temperature of 28 °C. The gray dots show the experimentally obtained measurement data of this work. In both literature works, glucose is dissolved in distilled water, which again may account for the slight deviations. The linear fit determined in this work lies in the middle of both literature values and therefore in a reasonable range, thus confirming the validity of the OAM interferometer for concentration measurements of glucose solutions in the  $\mu\text{M}$  range.

Lastly, the sensitivity of the OAM interferometer is compared to another basic, non-invasive optical technique for concentration measurements. Absorbance measurements (UV-Vis, Cary 3000, Agilent Technologies, Santa Clara, California, USA) were performed by Sebastian Rieger for NaCl and glucose solutions. Samples with various concentrations in the range of 31.25  $\mu\text{M}$  to 100 mM were prepared for NaCl and glucose. The resulting measured optical densities are plotted in Figure 4.21. For both data sets, the optical density (OD) values were extracted at the OD peak at  $\lambda = 200$  nm which was the most prominent feature in the OD spectra for both samples. These results clearly indicate that only concentrations larger than 10 mM can be detected using this method. A real differentiation from the background is only possible at concentration values above 10 mM, which is three orders of magnitude less accurate than the results obtained with the OAM interferometer.

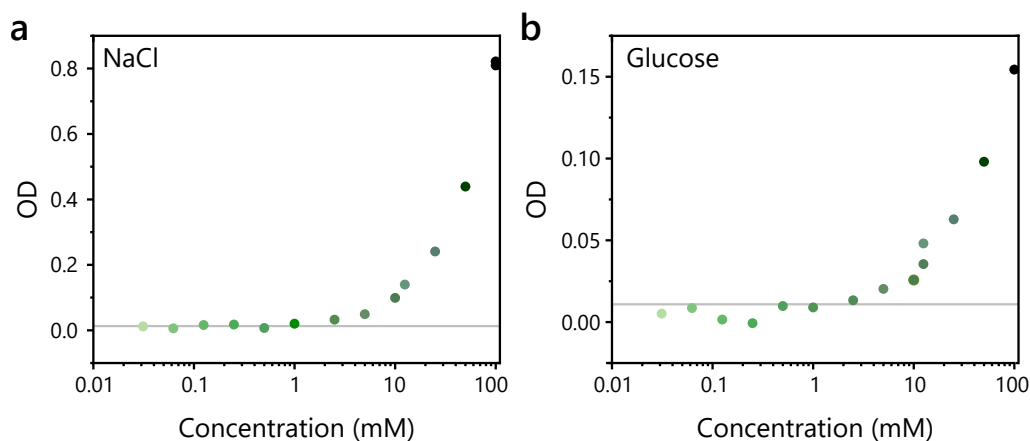


**Figure 4.21: Optical absorbance measurements.** (a) The optical density (OD) at the 200 nm absorption peak of the dilution series of NaCl solutions is shown. The gray line is a guide to the eye and indicates the baseline. (b) The identical measurement is performed for the glucose dilution series. [Adapted from Reference [232]].

Summing up the results of the concentration measurements, the lowest measured concentrations were 200  $\mu\text{M}$  for NaCl and 50  $\mu\text{M}$  for glucose, each corresponding to a change of the refractive index  $\Delta n$  in the range of  $10^{-6}$  RIU. When considering the resolution limit of the interferometer itself ( $\Delta n(0.128^\circ) = 2.87 \cdot 10^{-7}$  RIU), the smallest measurable concentrations

can be calculated at 37  $\mu\text{M}$  for NaCl and 11  $\mu\text{M}$  for glucose. Coming back to the example of glucose measurements for diabetes, the glucose concentration in ocular fluids lies at 300  $\mu\text{M}$  for elevated glucose levels and 160  $\mu\text{M}$  for healthy patients.<sup>246</sup> Therefore, the measurement resolution currently achieved by the OAM interferometer lies well within the necessary range for such applications. This proves the high applicability of the setup in biological sensing or screening. Conventional concentration measurement methods are often invasive, i.e., they require sample preparation, such as fluorescent labeling,<sup>247</sup> or are dependent on the ionic character of the analyte or the absorption cross-section. Notably, the OAM interferometer presented in this work operates non-invasively and provides high resolution concentration measurements regardless of the analyte character. A few experimental methods, including refractometers, with overall higher or similar resolutions do exist,<sup>84,248–261</sup> however, most of them require more complicated signal detection and processing. Especially, they rely on more restrictive measurement conditions such as high-vacuum or more costly components, such as spectrometers. One drawback that should be considered is the non-specificity of the measurement in OAM interferometry. Currently, only one type of analyte can be measured at once and the interferometer has to be calibrated for each sample. If more than one analyte would be present at once, the change in signal could not be allocated to a specific analyte distinctly. This method measures changes in concentrations with high resolutions, without determining the reason for the change. In pharmaceutical or industrial applications, this could be highly applicable for the control of production lines.<sup>262,263</sup> If the composition of the solution is known and a quality or purity control is desirable, the OAM interferometer can provide very high resolutions. All in all this method offers an extremely high concentration resolution for individual analytes, under ambient conditions and thereby proves to be highly applicable for lab-on-a-chip or other measurement applications.

## 4.5 Benchmarking the OAM Interferometer

When doing high-precision metrology with interferometers, the resolution of the respective setup is always one of the most crucial parameters. Therefore, much work has been invested into determining theoretical limits and then also in optimizing the experimental setup to approach these limits practically. In order to put the resolution of the built OAM interferometer into perspective, it is also necessary to compare the setup with other interferometers.

During the course of this research, very helpful input from Prof. Dr. Ernst Göbel and Dr. René Schödel from the *Physikalisch Technische Bundesanstalt (PTB)* and Dr. Wolfgang Holzapfel from *Heidenhain GmbH* was received on the topic of resolution limitations of interferometers and the significance of OAM interferometry in this regard. These insights along with further literature are presented in this final section to benchmark the OAM interferometer.

### 4.5.1 Shot Noise and Phase Noise

Theoretically, the upper limit for imaging resolution is often given by shot noise. Shot noise was discovered by Walter Schottky in 1918<sup>264</sup> and originates from the intrinsic quantization of charges or particles.<sup>265,266</sup> When considering the light emitted from a laser in the particle picture, the individual photons are emitted spontaneously. Over enough time, the laser output will appear at a constant power (number of photons per time) with a constant phase distribution. However, when looking at only a small number of photons, fluctuations are greater and a certain bias may be present. Due to the wave-particle duality in photons,<sup>122</sup> two pictures can be applied. When considering light as waves, the magnitude of the fluctuations is related linearly to the mean energy. On the other hand, when looking at photons as individual light particles, the fluctuations are related to the square root of the mean energy. At optical frequencies, however, the particle nature dominates.<sup>266</sup> Various approaches have successfully surpassed the shot noise limit, for example by using squeezed light,<sup>267,268</sup> Förster Resonance Energy Transfer (FRET)<sup>269</sup> or quantum plasmonic sensing.<sup>270</sup>

As the OAM beam highly depends on the azimuthal phase structure, also considering phase noise is crucial. This phase noise was quantified by Dr. Wolfgang Holzapfel. According to his calculations, the phase noise of an interferometer using OAM beams is always greater than the one of an interferometer using standard Gaussian light modes. This uncertainty stems from averaging slightly varied phases, due to the spatial phase distribution, of the beam over the widths of individual photodetectors. The initial Gaussian mode already has a phase noise and when transforming it into an LG mode with an SPP, further sources for errors are introduced and the quality of the beam may suffer.

Since the interferometer in this work is not placed inside a vacuum chamber, shot noise and phase noise lie significantly below the current resolution limit. The measured noise in [Subsection 4.2.3](#) is above the threshold where shot and phase noise are significant. Currently, the noise originates mainly from macroscopic variations in the air and surrounding environment temperature as well as building vibrations. If the interferometer is optimized further by eliminating these noise sources, shot noise and phase noise would certainly become more relevant when considering the actual interferometer resolution. The above mentioned options which surpass the shot noise limit, for example using squeezed light, are challenging to apply to OAM interferometry, however, possible<sup>271</sup> and thus may evolve to further improve the resolution limit. As mentioned in [Subsection 2.2.3](#), certain approaches using deep learning for phase correction in coherent beam combining (CBC)<sup>169</sup> have made it possible to eliminate phase noise altogether, yielding a much higher resolution potential also for OAM interferometry.

**Table 4.2: Comparison of the OAM interferometer and best in class interferometers.** Here, the OAM interferometer presented in this work and other best in class interferometers are compared based on several aspects of the measurement.

<b>This work</b>	<b>Best in class</b>
Resolution $10^{-7}$ RIU	Resolution $10^{-9}$ RIU
Single wavelength	White light
Low lateral resolution	2D scanning
No vacuum conditions	Usually in vacuum
Simplicity	Complex components

### 4.5.2 Interferometer Comparison

In order to benchmark the OAM interferometer presented in this work, Table 4.2 outlines some distinct features compared to the interferometers with the highest resolutions presented in literature. The resolution on the order of  $10^{-7}$  RIU is significant, however, other interferometric approaches have higher resolutions, up to the order of  $10^{-9}$  RIU<sup>272</sup> when measuring water vapor or  $10^{-8}$  RIU by considering the evanescent field in wave guides.<sup>250</sup> Additionally, the SPPs are always specifically designed and fabricated for a single wavelength, thus methods like the “coincidence criteria”, in which various wavelengths are applied to validate length measurements,<sup>273</sup> are not applicable. OAM beams can also be generated using spatial light modulators, which may circumvent this limitation. Furthermore, the potential to scan in 2D using OAM beams is challenging in the setup described in this work. Since in this work, the beam is generated using SPPs, the sample and not the beam would be required to move laterally. Currently, the OAM beam has a diameter of approximately 2 mm, which does not provide a significant lateral resolution. Focusing the beam down by introducing objective lenses would further increase the applicability of OAM interferometry. This would open the possibility, for example, for optical topography determination on the picometer scale.

However, the OAM interferometer shows great benefits in terms of simplicity and applicability. Most of the methods achieving higher resolutions require precisely controlled high vacuum conditions. External factors highly dictate the resolution or applicability of interferometers in general. For example, local fluctuations of the surrounding air limit the possibility to measure length differences under atmospheric conditions.<sup>274</sup> The claimed resolution of the OAM interferometer is currently achieved in ambient air, providing high applicability to samples which may not sustain a vacuum. This highlights the simplicity. The resolution still has great potential to be improved further when, e.g., applying vacuum conditions to the OAM interferometer. Furthermore, as described thoroughly in this chapter, the components required to build the OAM interferometer are easily implemented and could even be

combined with other setups. More advanced interferometry methods often require a combination of several experimental techniques, specialized equipment, sensors and especially computational power. Since most approaches are unique to a certain application, expertise with each setup is required to actually achieve such high resolutions. The current resolution is determined by the standard deviation of the fluctuations presented in Figure 4.7. When applying a modulation to compensate for the slow fluctuations, the resolution would only be limited by the faster fluctuation component. In this case, the standard deviation of  $0.031^\circ$  presented in Figure 4.8 would be considered, and taking Equation 2.19 into account the overall resolution could be improved to  $6.87 \cdot 10^{-8}$  RIU.

Overall, OAM interferometry can be benchmarked as a novel approach to interferometry. During the course of this thesis, OAM interferometers has significantly gained in interest, and a handful of recent publications is provided in References [87, 234, 275, 276]. This thesis extended this principle further and applied it to temperature and concentration measurements of liquid samples. Especially in fluids, the measurement of temperature is not trivial, due to possibly inhomogeneous temperature distributions. Most flow cell materials, such as quartz glass, are not IR transmissive. Therefore, direct temperature measurements with IR cameras are challenging. After a calibration, like performed in this work, the interferometer can be used to measure the temperature of liquid samples non-invasively and contactless. Concentration measurements are usually specific to the nature of the analyte. Here, it is possible to determine concentrations with high accuracy, without depending on the ionic properties or the absorption cross section of the analyte or the solvent. The resolution limit and data presented in this thesis stem from measurements over long times at ambient laboratory conditions and, therefore, the values correspond to realistic resolutions with reasonable expenditure required. Thus, the OAM interferometer may find application in lab-on-a-chip approaches or situations where the precise *in situ* monitoring of the temperature or a concentration of a solution is required, for example in pharmaceutical manufacturing.<sup>262</sup>



# 5

## Conclusion

*In this thesis, temperature manipulation by directing thermal radiation and an alternative method for contactless temperature measurements are devised. Directing thermal radiation to obtain structured cooling as well as orbital angular momentum interferometry for high-precision temperature measurement add novel and versatile concepts to the toolbox of radiative temperature manipulation and measurement. Both methods enable the contactless realization and measurement of temperature gradients in situ. In order to conclude this work, the acquired results are summarized and set into context. The two approaches exploiting the relationship of temperature and radiation  $h\nu \leftrightarrow T$  are concluded individually.*

## Directing Thermal Radiation for Spatially Structured Cooling

In the first part of this thesis, a novel method for thermal pattern generation was devised and practically implemented. Commonly, when thermal gradients are generated, the central point is heated and the surroundings are colder. With this method, by using an elliptical mirror to direct the natural black body radiation away from a body onto a cold reservoir, it is possible to generate thermal patterns with a cold central region. This work was inspired by the emerging and rapidly growing field of ambient radiative cooling, where the vast coldness of the universe is harvested for temperature control on Earth.

The same concept is applied here and brought it into the laboratory in order to better understand and exploit the process of radiative cooling. Especially the usage of geometrical optics to enhance the view factor was investigated and it turned out to be a key factor in rendering such cooling effective. Temperature differences of 12 °C were reached in a room temperature surrounding, without positioning the sample in a vacuum. This means during the cooling process, the radiative pathway was constantly competing against the heating of the sample which was driven by convection inside the laboratory and by conduction within the sample and the sample holder. The demonstrated applications include the possibility of radiative supercooling as well as the local temperature manipulation of a biological sample. Plant leaves are efficient black body emitters in the transparency window of the atmosphere.

During the course of this thesis, the concept of ambient radiative cooling and our proposed enhancement of the view factor have been brought together for the first time. Since then it has evolved and was coined concentrated radiative cooling (CRC).<sup>277,278</sup> By directing radiation for spatially structured cooling, the radiative pathway proved to be efficient, even under ambient conditions. The potential applications are manifold and encompass multiple disciplines. This novel non-invasive approach for structured cooling can be used to control chemical reactions, to manipulate biological samples, and to improve the performance of physical devices.

## Temperature Measurements With Twisted Light

While the most common contactless thermometers detect an object's IR radiation, only few alternative contactless methods exist that may be employed when thermal imaging may not be applicable. The impact of temperature on optical properties was exploited for a novel optical detection of temperature changes.

An interferometer using orbital angular momentum (OAM) beams instead of standard Gaussian modes was built, which introduced a new degree of freedom. Photons with angular momenta of multiple  $\hbar$ , are exploited to measure minuscule phase changes. The



setup employs OAM beams with opposing helicity resulting in an interference pattern in the form of a daisy flower. Most significantly, this interference pattern rotates around the azimuthal axis when a phase change is introduced in one of the interferometer arms. Liquid samples in flow cells are placed in the measurement arm to induce such phase changes. This is the unique characteristic exploited in this work to measure changes in the refractive index. Accordingly, the temperature-dependence of the refractive index of these liquids causes a rotation of the interference pattern. By simultaneously monitoring the temperature of a microfluidic cell filled with ddH<sub>2</sub>O with an IR camera, the change in rotation angle  $\Delta\theta_{\text{rot}}$  of the interference pattern is directly linked to a change in temperature. Changes in the refractive index are determined with precision on the order of  $10^{-7}$  RIU. This translates into a temperature resolution of 890  $\mu\text{K}$ . In order to investigate this change in refractive index per change in temperature, the resulting thermo-optic coefficient was compared to literature values. It is on the same order of magnitude and comparable to previously determined thermo-optic coefficients.

The dependence of the refractive index on concentration provides the basis for extending the OAM interferometer to concentration measurements. Concentrations are often determined by ionic conductivity measurements, absorption spectroscopy or using markers specific to the molecule to be measured or by methods requiring invasive labeling, such as fluorescence or plasmonics. By determining the concentration via the change in refractive index, concentration is measured independent of the absorption cross-section, the ionic character of the analyte or any specific binding characteristics. The resolution on the order of  $10^{-7}$  RIU translates into concentration measurements in the range of several  $\mu\text{M}$  ( $10^{-4}$  w%) precision. The measured refractive index dependence on the concentration of the solution is compared to extrapolated literature values and shows great overlap. Thereby, the OAM interferometer is validated as a versatile method to perform high-precision, contactless, label-free *in situ* concentration measurements, independent of the analyte.

The interest in OAM interferometry has risen significantly in the past years, leading to various application of such beams in interferometry. The resolution of the setup can be enhanced even further by stabilizing measurement conditions, such as by placing the setup in a vacuum or by using novel coherent beam combining methods. Overall, this type of orbital angular momentum interference applied to liquid samples yields a novel, robust, and easily implementable method for high-precision *in situ* monitoring of the temperature and concentration in microfluidic samples.



# References

- [1] National Aeronautics and Space Administration (NASA) History. *A Meeting with the Universe: The Sun and Us*. 2022. url: [history.nasa.gov/EP-177/ch3-1.html#:~:text=Without%20the%20Sun's%20heat%20and,oxygen%20for%20life%20on%20Earth](https://history.nasa.gov/EP-177/ch3-1.html#:~:text=Without%20the%20Sun's%20heat%20and,oxygen%20for%20life%20on%20Earth). (visited on 07/22/2022) (cited on page 1).
- [2] P. Xu, L. Wang, Y. Liu, W. Chen, and P. Huang. "The record-breaking heat wave of June 2019 in Central Europe". In: *Atmospheric Science Letters* 21.4 (2020), e964. doi: 10.1002/asl.964 (cited on page 1).
- [3] G. A. Meehl and C. Tebaldi. "More intense, more frequent, and longer lasting heat waves in the 21st century". In: *Science* 305.5686 (2004), pp. 994–997. doi: 10.1126/science.1098704 (cited on pages 1, 20).
- [4] M. N. Bahadori. "Passive cooling systems in Iranian architecture". In: *Scientific American* 238.2 (1978), pp. 144–155 (cited on page 1).
- [5] A. P. Raman, M. A. Anoma, L. Zhu, E. Rephaeli, and S. Fan. "Passive radiative cooling below ambient air temperature under direct sunlight". In: *Nature* 515.7528 (2014), pp. 540–544. doi: 10.1038/nature13883 (cited on pages 1, 16, 20).
- [6] Z. Chen, L. Zhu, A. P. Raman, and S. Fan. "Radiative cooling to deep sub-freezing temperatures through a 24-h day–night cycle". In: *Nature communications* 7.1 (2016), pp. 1–5. doi: 10.1038/ncomms13729 (cited on pages 2, 20).
- [7] S. Ullah, M. Schlerf, A. K. Skidmore, and C. Hecker. "Identifying plant species using mid-wave infrared (2.5–6  $\mu\text{m}$ ) and thermal infrared (8–14  $\mu\text{m}$ ) emissivity spectra". In: *Remote Sensing of Environment* 118 (2012), pp. 95–102. doi: 10.1016/j.rse.2011.11.008 (cited on pages 2, 54).
- [8] M. R. Pandya, D. B. Shah, H. J. Trivedi, M. M. Lunagaria, V. Pandey, S. Panigrahy, and J. S. Parihar. "Field measurements of plant emissivity spectra: An experimental study on remote sensing of vegetation in the thermal infrared region". In: *Journal of the Indian Society of Remote Sensing* 41.4 (2013), pp. 787–796. doi: 10.1007/s12524-013-0283-2 (cited on pages 2, 54).
- [9] B. R. Da Luz and J. K. Crowley. "Spectral reflectance and emissivity features of broad leaf plants: Prospects for remote sensing in the thermal infrared (8.0–14.0  $\mu\text{m}$ )". In: *Remote Sensing Of Environment* 109.4 (2007), pp. 393–405. doi: 10.1016/j.rse.2007.01.008 (cited on pages 2, 54).
- [10] C. Kittel and H. Kroemer. *Thermal physics*. American Association of Physics Teachers, 1998 (cited on page 6).
- [11] H. B. Callen. *Thermodynamics and an Introduction to Thermostatistics*. American Association of Physics Teachers, 1998 (cited on page 6).
- [12] B. M. Askerov and S. Figarova. *Thermodynamics, Gibbs method and statistical physics of electron gases*. Vol. 57. Springer Science & Business Media, 2009 (cited on page 6).
- [13] J. R. Howell, M. P. Mengüç, K. Daun, and R. Siegel. *Thermal radiation heat transfer*. CRC press, 2020 (cited on pages 6, 8–12, 14, 15).
- [14] R. Napiwotzki, D. Schönberner, and V. Wenske. "On the determination of effective temperature and surface gravity of B, A, and F stars using Stromgren UVBY beta photometry". In: *Astronomy and Astrophysics* 268 (1993), pp. 653–666 (cited on page 6).
- [15] D. W. Hahn and M. N. Özisik. *Heat conduction*. John Wiley & Sons, 2012 (cited on page 7).
- [16] L. M. Jiji and L. M. Jiji. *Heat conduction*. Springer, 2009 (cited on page 7).
- [17] L. M. Jiji and L. M. Jiji. *Heat convection*. Springer, 2006 (cited on page 7).
- [18] R. Sadri, M. Hosseini, S. N. Kazi, S. Bagheri, A. H. Abdelrazek, G. Ahmadi, N. Zubir, R. Ahmad, and N. I. Z. Abidin. "A facile, bio-based, novel approach for synthesis of covalently functionalized graphene nanoplatelet nano-coolants toward improved thermo-physical and heat transfer properties". In: *Journal of Colloid and Interface Science* 509 (2018), pp. 140–152. doi: 10.1016/j.jcis.2017.07.052 (cited on page 8).
- [19] T. Muneer and S. Ivanova. "Efficient Routines for Obtaining Radiation View-Factor for Non-Uniform Horizons". In: *Energies* 13.10 (2020), p. 2551. doi: 10.3390/en13102551 (cited on page 10).
- [20] K. S. Mudan. "Geometric view factors for thermal radiation hazard assessment". In: *Fire Safety Journal* 12.2 (1987), pp. 89–96. doi: 10.1016/0379-7112(87)90024-5 (cited on page 10).

- [21] Y. K. Khor, Y. M. Hung, and B. K. Lim. "On the role of radiation view factor in thermal performance of straight-fin heat sinks". In: *International Communications in Heat and Mass Transfer* 37.8 (2010), pp. 1087–1095. doi: [10.1016/j.icheatmasstransfer.2010.06.012](https://doi.org/10.1016/j.icheatmasstransfer.2010.06.012) (cited on page 10).
- [22] M. K. Gupta, K. J. Buntariya, H. A. Shukla, P. Patel, and Z. Khan. "Methods for evaluation of radiation view factor: a review". In: *Materials Today: Proceedings* 4.2 (2017), pp. 1236–1243. doi: [10.1016/j.matpr.2017.01.143](https://doi.org/10.1016/j.matpr.2017.01.143) (cited on page 10).
- [23] A. Narayanaswamy. "An analytic expression for radiation view factor between two arbitrarily oriented planar polygons". In: *International Journal of Heat and Mass Transfer* 91 (2015), pp. 841–847. doi: [10.1016/j.ijheatmasstransfer.2015.07.131](https://doi.org/10.1016/j.ijheatmasstransfer.2015.07.131) (cited on page 10).
- [24] I. Newton. "Scala graduum caloris". In: *Philosophical Transactions of the Royal Society (London)* 22 (1701), pp. 824–829 (cited on page 11).
- [25] U. Grigull. "Newton's temperature scale and the law of cooling". In: *Wärme-und Stoffübertragung* 18.4 (1984), pp. 195–199. doi: [10.1007/BF01007129](https://doi.org/10.1007/BF01007129) (cited on page 11).
- [26] R. H. S. Winterton. "Newton's law of cooling". In: *Contemporary Physics* 40.3 (1999), pp. 205–212. doi: [10.1080/001075199181549](https://doi.org/10.1080/001075199181549) (cited on page 11).
- [27] M. Vollmer. "Newton's law of cooling revisited". In: *European Journal of Physics* 30.5 (2009), p. 1063. doi: [10.1088/0143-0807/30/5/014](https://doi.org/10.1088/0143-0807/30/5/014) (cited on page 11).
- [28] A. Adams, F. Nicol, S. McHugh, J. Moore, G. Matis, and G. A. Amparan. "Vantablack properties in commercial thermal infrared imaging systems". In: *Infrared Imaging Systems: Design, Analysis, Modeling, and Testing XXX*. Vol. 11001. SPIE, 2019, pp. 329–339. doi: [10.1117/12.2518768](https://doi.org/10.1117/12.2518768) (cited on page 11).
- [29] K. Cui and B. L. Wardle. "Breakdown of native oxide enables multifunctional, free-form carbon nanotube-metal hierarchical architectures". In: *ACS Applied Materials & Interfaces* 11.38 (2019), pp. 35212–35220. doi: [10.1021/acsami.9b08290](https://doi.org/10.1021/acsami.9b08290) (cited on page 12).
- [30] M. Planck. "Über das Gesetz der Energieverteilung im Normalspektrum". In: *Annalen der Physik* 309 (1901), pp. 553–563. doi: [10.1007/978-3-663-13885-3\\_16](https://doi.org/10.1007/978-3-663-13885-3_16) (cited on pages 12, 13).
- [31] W. Wien. *Über die Gesetze der Wärmestrahlung: Nobel-Vortrag gehalten am 11. Dezember 1911 in Stockholm*. Barth, 1912 (cited on page 13).
- [32] P. T. Landsberg and A. De Vos. "The Stefan-Boltzmann constant in n-dimensional space". In: *Journal of Physics A: Mathematical and General* 22.8 (1989), p. 1073. doi: [10.1088/0305-4470/22/8/021](https://doi.org/10.1088/0305-4470/22/8/021) (cited on page 13).
- [33] P. Haggstrom. *Deriving the Stefan-Boltzmann law from Planck's law*. 2020. url: [gotohaggstrom.com/Deriving%20the%20Stefan-Boltzmann%20law%20from%20Plancks%20law.pdf](http://gotohaggstrom.com/Deriving%20the%20Stefan-Boltzmann%20law%20from%20Plancks%20law.pdf) (visited on 07/27/2022) (cited on page 13).
- [34] C. Niu, T. Zhu, and Y. Lv. "Influence of surface morphology on absorptivity of light-absorbing materials". In: *International Journal of Photoenergy* 2019 (2019). doi: [10.1155/2019/1476217](https://doi.org/10.1155/2019/1476217) (cited on page 14).
- [35] S. Taylor, J. B. Wright, E. C. Forrest, B. Jared, J. Koepke, and J. Beaman. "Investigating relationship between surface topography and emissivity of metallic additively manufactured parts". In: *International Communications in Heat and Mass Transfer* 115 (2020), p. 104614. doi: [10.1016/j.icheatmasstransfer.2020.104614](https://doi.org/10.1016/j.icheatmasstransfer.2020.104614) (cited on page 15).
- [36] G. Kirchhoff. "I. On the relation between the radiating and absorbing powers of different bodies for light and heat". In: *The London, Edinburgh, and Dublin Philosophical Magazine and Journal of Science* 20.130 (1860), pp. 1–21. doi: [10.1080/14786446008642901](https://doi.org/10.1080/14786446008642901) (cited on page 15).
- [37] G. B. Rybicki and A. P. Lightman. *Radiative processes in astrophysics*. John Wiley & Sons, 1991 (cited on page 15).
- [38] W. Li and S. Fan. "Radiative cooling: harvesting the coldness of the universe". In: *Optics and Photonics News* 30.11 (2019), pp. 32–39. doi: [10.1364/OPN.30.11.000032](https://doi.org/10.1364/OPN.30.11.000032) (cited on page 16).
- [39] S. Fan and W. Li. "Photonics and thermodynamics concepts in radiative cooling". In: *Nature Photonics* 16.3 (2022), pp. 182–190. doi: [10.1038/s41566-021-00921-9](https://doi.org/10.1038/s41566-021-00921-9) (cited on pages 16, 20).
- [40] A. A. Penzias and R. W. Wilson. "A measurement of excess antenna temperature at 4080 Mc/s." In: *The Astrophysical Journal* 142 (1965), pp. 419–421. doi: [10.1086/148307](https://doi.org/10.1086/148307) (cited on page 16).
- [41] E. R. Harrison. "Standard model of the early universe". In: *Annual Review of Astronomy and Astrophysics* 11.1 (1973), pp. 155–186 (cited on page 17).

- [42] R. Rohde, R. A. Muller, R. Jacobsen, E. Muller, S. Perlmutter, A. Rosenfeld, J. Wurtele, D. Groom, and C. Wickham. "A New Estimate of the Average Earth Surface Land Temperature Spanning 1753 to 2011, Geoinfor Geostat: An Overview 1: 1". In: *Geoinformatics & Geostatistics: An Overview 7* (2013), p. 2. doi: 10.4172/2327-4581.1000101 (cited on page 17).
- [43] P. Würfel, A. S. Brown, T. E. Humphrey, and M. A. Green. "Particle conservation in the hot-carrier solar cell". In: *Progress in Photovoltaics: Research and Applications* 13.4 (2005), pp. 277–285. doi: 10.1002/pip.584 (cited on page 17).
- [44] D. H. Hathaway. *National Aeronautics and Space Administration (NASA): The Solar Interior*. 2015. url: [solarscience.msfc.nasa.gov/interior.shtml](http://solarscience.msfc.nasa.gov/interior.shtml) (visited on 06/24/2022) (cited on page 17).
- [45] NAVAIR Weapons Division. *EW & Radar Handbook: Electro-optics*. 2022. url: [web.archive.org/web/20010913091738/http://ewhdbks.mugu.navy.mil/EO-IR.htm#transmission](http://web.archive.org/web/20010913091738/http://ewhdbks.mugu.navy.mil/EO-IR.htm#transmission) (visited on 03/31/2022) (cited on page 18).
- [46] M. Stomp, J. Huisman, L. J. Stal, and H. C. P. Matthijs. "Colorful niches of phototrophic microorganisms shaped by vibrations of the water molecule". In: *The ISME journal* 1.4 (2007), pp. 271–282. doi: 10.1038/ismej.2007.59 (cited on page 18).
- [47] R. Olbrycht, M. Kałuzna, W. Wittchen, M. Borecki, B. Wiecek, G. De Mey, and M. Kopec. "Gas identification and estimation of its concentration in a tube using thermographic camera with diffraction grating". In: *Quantitative InfraRed Thermography Journal* 15.1 (2018), pp. 106–120. doi: 10.1080/17686733.2017.1385179 (cited on page 18).
- [48] W. T. Roach and R. M. Goody. "Absorption and emission in the atmospheric window from 770 to 1,250  $\text{cm}^{-1}$ ". In: *Quarterly Journal of the Royal Meteorological Society* 84.362 (1958), pp. 319–333. doi: 10.1002/qj.49708436203 (cited on page 18, 20).
- [49] M. Fingas. *Oil spill science and technology*. Gulf Professional Publishing, 2016. doi: 10.1016/C2015-0-04851-1 (cited on page 18).
- [50] W. C. Wang, Y. L. Yung, A. A. Lacis, T. A. Mo, and J. E. Hansen. "Greenhouse Effects due to Man-Made Perturbations of Trace Gases: Anthropogenic gases may alter our climate by plugging an atmospheric window for escaping thermal radiation". In: *Science* 194.4266 (1976), pp. 685–690. doi: 10.1126/science.194.4266.685 (cited on page 18).
- [51] J. F. B. Mitchell. "The 'greenhouse' effect and climate change". In: *Reviews of Geophysics* 27.1 (1989), pp. 115–139. doi: 10.1029/RG027i001p00115 (cited on page 19).
- [52] B. Bolin and B. R. Doos. *Greenhouse effect*. New York, NY (USA); John Wiley and Sons Inc., 1989 (cited on page 19).
- [53] A. Mikhaylov, N. Moiseev, K. Aleshin, and T. Burkhardt. "Global climate change and greenhouse effect". In: *Entrepreneurship and Sustainability Issues* 7.4 (2020), p. 2897. doi: 10.9770/jesi.2020.7.4(21) (cited on page 19).
- [54] D. W. Kweku, O. Bismark, A. Maxwell, K. A. Desmond, K. B. Danso, E. A. Oti-Mensah, A. T. Quachie, and B. B. Adormaa. "Greenhouse effect: greenhouse gases and their impact on global warming". In: *Journal of Scientific Research and Reports* 17.6 (2018), pp. 1–9. doi: 10.9734/JSRR/2017/39630 (cited on page 19).
- [55] J. Houghton. "Global warming". In: *Reports on Progress in Physics* 68.6 (2005), p. 1343. doi: 10.1088/0034-4885/68/6/R02 (cited on page 19).
- [56] M. Allen, M. Babiker, Y. Chen, H. de Coninck, S. Connors, R. van Diemen, O. P. Dube, K. L. Ebi, F. Engelbrecht, M. Ferrat, J. Ford, P. Foster, S. Fuss, T. Guillen Bolanos, J. Harold, O. Hoegh-Guldberg, J.-C. Hourcade, D. Huppmann, D. Jacob, K. Jiang, et al. *Global Warming of 1.5 C. Summary for Policymakers*. Intergovernmental Panel on Climate Change (IPCC), 2018 (cited on page 19).
- [57] L. D. D. Harvey. *Global warming*. Routledge, 2018. doi: 10.4324/9781315838779 (cited on page 19).
- [58] C. Honsberg and S. Bowden. *Standard Solar Spectra*. 2022. url: [pveducation.org/pvcdrom/appendices/standard-solar-spectra](http://pveducation.org/pvcdrom/appendices/standard-solar-spectra) (visited on 04/13/2022) (cited on page 19).
- [59] I. N. Glushneva, V. I. Shenavrin, and I. A. Roshchina. "Effective temperatures of solar type stars". In: *Astronomical & Astrophysical Transactions* 21.4-6 (2002), pp. 317–325. doi: 10.1080/10556790215603 (cited on page 19).
- [60] M. Isaac and D. P. Van Vuuren. "Modeling global residential sector energy demand for heating and air conditioning in the context of climate change". In: *Energy Policy* 37.2 (2009), pp. 507–521. doi: 10.1016/j.enpol.2008.09.051 (cited on page 20).

- [61] J. Mandal, S. Mandal, J. Brewer, A. Ramachandran, and A. P. Raman. "Radiative Cooling and Thermoregulation in the Earth's Glow". In: *arXiv preprint arXiv:2006.11931* (2020) (cited on page 20).
- [62] J. W. Salisbury and D. M. D'Aria. "Emissivity of terrestrial materials in the 8–14  $\mu\text{m}$  atmospheric window". In: *Remote sensing of Environment* 42.2 (1992), pp. 83–106. doi: 10.1016/0034-4257(92)90092-X (cited on page 20).
- [63] P. Berdahl, M. Martin, and F. Sakka. "Thermal performance of radiative cooling panels". In: *International Journal of Heat and Mass Transfer* 26.6 (1983), pp. 871–880. doi: 10.1016/S0017-9310(83)80111-2 (cited on page 20).
- [64] C. G. Granqvist, A. Hjortsberg, and T. S. Eriksson. "Radiative cooling to low temperatures with selectivity IR-emitting surfaces". In: *Thin Solid Films* 90.2 (1982), pp. 187–190. doi: 10.1016/0040-6090(82)90648-4 (cited on page 20).
- [65] C. G. Granqvist and A. Hjortsberg. "Radiative cooling to low temperatures: General considerations and application to selectively emitting SiO films". In: *Journal of Applied Physics* 52.6 (1981), pp. 4205–4220. doi: 10.1063/1.329270 (cited on page 20).
- [66] C. G. Granqvist and A. Hjortsberg. "Surfaces for radiative cooling: Silicon monoxide films on aluminum". In: *Applied Physics Letters* 36.2 (1980), pp. 139–141. doi: 10.1063/1.91406 (cited on page 20).
- [67] P. Varanasi. "Infrared absorption by water vapor in the atmospheric window". In: *Modeling of the Atmosphere*. Vol. 928. International Society for Optics and Photonics. 1988, pp. 213–230. doi: 10.1117/12.975629 (cited on page 20).
- [68] C. M. Cornelius and J. P. Dowling. "Modification of Planck blackbody radiation by photonic band-gap structures". In: *Physical Review A* 59.6 (1999). doi: 10.1103/PhysRevA.59.4736 (cited on page 20).
- [69] S.-Y. Lin, J. G. Fleming, E. Chow, and J. Bur. "Enhancement and suppression of thermal emission by a three-dimensional photonic crystal". In: *Physical Review B* 62.4 (2000). doi: 10.1103/PhysRevB.62.R2243 (cited on page 20).
- [70] J.-J. Greffet, R. Carminati, K. Joulain, J. P. Mulet, S. Mainguy, and Y. Chen. "Coherent emission of light by thermal sources". In: *Nature* 416.6876 (2002), pp. 61–64. doi: 10.1038/416061a (cited on pages 20, 23).
- [71] M. Laroche, R. Carminati, and J.-J. Greffet. "Coherent thermal antenna using a photonic crystal slab". In: *Physical Review Letters* 96.12 (2006), p. 123903. doi: 10.1103/PhysRevLett.96.123903 (cited on page 20).
- [72] X. Liu, T. Tyler, T. Starr, A. F. Starr, N. M. Jokerst, and W. J. Padilla. "Taming the blackbody with infrared metamaterials as selective thermal emitters". In: *Physical Review Letters* 107.4 (2011), p. 045901. doi: 10.1103/PhysRevLett.107.045901 (cited on page 20).
- [73] J. Xu, J. Mandal, and A. P. Raman. "Broadband directional control of thermal emission". In: *Science* 372.6540 (2021), pp. 393–397. doi: 10.1126/science.abc5381 (cited on page 20).
- [74] S. Fan. "Thermal photonics and energy applications". In: *Joule* 1.2 (2017), pp. 264–273. doi: 10.1016/j.joule.2017.07.012 (cited on page 20).
- [75] W. Li and S. Fan. "Nanophotonic control of thermal radiation for energy applications". In: *Optics Express* 26.12 (2018), pp. 15995–16021. doi: 10.1364/OE.26.015995 (cited on page 20).
- [76] G. Mie. "Beiträge zur Optik trüber Medien, speziell kolloidaler Metallösungen". In: *Annalen der Physik* 330.3 (1908), pp. 377–445. doi: 10.1002/andp.19083300302 (cited on page 20).
- [77] L. Zhu, A. P. Raman, and S. Fan. "Radiative cooling of solar absorbers using a visibly transparent photonic crystal thermal blackbody". In: *Proceedings of the National Academy of Sciences* 112.40 (2015), pp. 12282–12287. doi: 10.1073/pnas.1509453112 (cited on page 20).
- [78] A. Srinivasan, B. Czapla, J. Mayo, and A. Narayanaswamy. "Infrared dielectric function of polydimethylsiloxane and selective emission behavior". In: *Applied Physics Letters* 109.6 (2016), p. 061905. doi: 10.1063/1.4961051 (cited on page 20).
- [79] Y. Zhai, Y. Ma, S. N. David, D. Zhao, R. Lou, G. Tan, R. Yang, and X. Yin. "Scalable-manufactured randomized glass-polymer hybrid metamaterial for daytime radiative cooling". In: *Science* 355.6329 (2017), pp. 1062–1066. doi: 10.1126/science.aai7899 (cited on page 20).
- [80] J. Mandal, Y. Fu, A. C. Overvig, M. Jia, K. Sun, N. N. Shi, H. Zhou, X. Xiao, N. Yu, and Y. Yang. "Hierarchically porous polymer coatings for highly efficient passive daytime radiative cooling". In: *Science* 362.6412 (2018), pp. 315–319. doi: 10.1126/science.aat9513 (cited on page 20).

- [81] J. Mandal, Y. Yang, N. Yu, and A. P. Raman. "Paints as a scalable and effective radiative cooling technology for buildings". In: *Joule* 4.7 (2020), pp. 1350–1356. doi: 10.1016/j.joule.2020.04.010 (cited on page 20).
- [82] E. Moisélo, P. Malcovati, and E. Bonizzoni. "Thermal sensors for contactless temperature measurements, occupancy detection, and automatic operation of appliances during the COVID-19 pandemic: A review". In: *Micromachines* 12.2 (2021), p. 148. doi: 10.3390/mi12020148 (cited on page 22).
- [83] G. B. Dell'Isola, E. Cosentini, L. Canale, G. Ficco, and M. Dell'Isola. "Noncontact body temperature measurement: uncertainty evaluation and screening decision rule to prevent the spread of COVID-19". In: *Sensors* 21.2 (2021), p. 346. doi: 10.3390/s21020346 (cited on page 22).
- [84] F. N. D. D. Pereira and A. C. H. Hallett. "A New Double Beam Optical Lever Refractometer and the Variation of the Refractive Index of NaCl with Temperature". In: *Review of Scientific Instruments* 42.4 (1971), pp. 490–493. doi: 10.1063/1.1685138 (cited on pages 22, 88).
- [85] P. Lu, L. Men, K. Sooley, and Q. Chen. "Tapered fiber Mach–Zehnder interferometer for simultaneous measurement of refractive index and temperature". In: *Applied Physics Letters* 94.13 (2009), p. 131110. doi: 10.1063/1.3115029 (cited on page 22).
- [86] Y. Zhao, M. Dai, Z. Chen, X. Liu, M. S. A. Gandhi, Q. Li, and H. Y. Fu. "Ultrasensitive temperature sensor with Vernier-effect improved fiber Michelson interferometer". In: *Optics Express* 29.2 (2021), pp. 1090–1101. doi: 10.1364/OE.415857 (cited on page 22).
- [87] F. Xia, Y. Zhao, H.-F. Hu, and Y. Zhang. "Optical fiber sensing technology based on Mach-Zehnder interferometer and orbital angular momentum beam". In: *Applied Physics Letters* 112.22 (2018), p. 221105. doi: 10.1063/1.5030900 (cited on pages 22, 91).
- [88] R. Schödel. "Ultra-high accuracy thermal expansion measurements with PTB's precision interferometer". In: *Measurement Science and Technology* 19.8 (2008), p. 084003. doi: 10.1088/0957-0233/19/8/084003 (cited on page 22).
- [89] Y. Wang, Y. Li, C. Liao, D. N. Wang, M. Yang, and P. Lu. "High-temperature sensing using miniaturized fiber in-line Mach–Zehnder interferometer". In: *IEEE Photonics Technology Letters* 22.1 (2009), pp. 39–41. doi: 10.1109/LPT.2009.2035638 (cited on page 22).
- [90] C. Wu, H. Y. Fu, K. K. Qureshi, B.-O. Guan, and H. Y. Tam. "High-pressure and high-temperature characteristics of a Fabry–Perot interferometer based on photonic crystal fiber". In: *Optics Letters* 36.3 (2011), pp. 412–414. doi: 10.1364/OL.36.000412 (cited on page 22).
- [91] H. Y. Choi, K. S. Park, S. J. Park, U.-C. Paek, B. H. Lee, and E. S. Choi. "Miniature fiber-optic high temperature sensor based on a hybrid structured Fabry–Perot interferometer". In: *Optics Letters* 33.21 (2008), pp. 2455–2457. doi: 10.1364/OL.33.002455 (cited on page 22).
- [92] J.-I. Kou, J. Feng, L. Ye, F. Xu, and Y.-Q. Lu. "Miniaturized fiber taper reflective interferometer for high temperature measurement". In: *Optics Express* 18.13 (2010), pp. 14245–14250. doi: 10.1364/OE.18.014245 (cited on page 22).
- [93] D. Liu, Q. Wu, C. Mei, J. Yuan, X. Xin, A. K. Mallik, F. Wei, W. Han, R. Kumar, C. Yu, S. Wan, L. Bo, G.-D. Peng, Semenova Y., and G. Farrell. "Hollow core fiber based interferometer for high-temperature (1000 C) measurement". In: *Journal of Lightwave Technology* 36.9 (2018), pp. 1583–1590 (cited on page 22).
- [94] A. Michelson and E. W. Morley. "On the Relative Motion of the Earth and of the Luminiferous Ether". In: *Sidereal Messenger* 6 (1887), pp. 306–310 (cited on page 23).
- [95] R. S. Shankland. "Michelson: America's first Nobel Prize winner in science". In: *The Physics Teacher* 15.1 (1977), pp. 19–25. doi: 10.1119/1.2339523 (cited on page 23).
- [96] B. P. Abbott, R. Abbott, T. D. Abbott, M. R. Abernathy, F. Acernese, K. Ackley, C. Adams, T. Adams, P. Addesso, R. X. Adhikari, V. B. Adya, C. Affeldt, M. Agathos, K. Agatsuma, N. Aggarwal, O. D. Aguiar, L. Aiello, A. Ain, P. Ajith, B. Allen, A. Allocca, et al. "Observation of Gravitational Waves from a Binary Black Hole Merger". In: *Physical Review Letters* 116.6 (2016), p. 061102. doi: 10.1103/PhysRevLett.116.061102 (cited on page 23).
- [97] R. X. Adhikari. "Gravitational radiation detection with laser interferometry". In: *Review Modern Physics* 86.1 (2014), pp. 121–151. doi: 10.1103/RevModPhys.86.121 (cited on page 23).
- [98] B. C. Barish. "Nobel Lecture: LIGO and gravitational waves II". In: *Reviews of Modern Physics* 90.4 (2018), p. 040502. doi: 10.1002/andp.201800357 (cited on page 23).
- [99] J. C. Wyant. "White light interferometry". In: *Holography: a Tribute to Yuri Denisjuk and Emmett Leith*. Vol. 4737. SPIE. 2002, pp. 98–107. doi: 10.1117/12.474947 (cited on page 23).

- [100] Y.-S. Jang, H. Liu, J. Yang, M. Yu, D.-L. Kwong, and C. W. Wong. “Nanometric precision distance metrology via hybrid spectrally resolved and homodyne interferometry in a single soliton frequency microcomb”. In: *Physical Review Letters* 126.2 (2021), p. 023903. doi: 10.1103/PhysRevLett.126.023903 (cited on page 24).
- [101] Y. Hori, S. Gonda, Y. Bitou, A. Watanabe, and K. Nakamura. “Periodic error evaluation system for linear encoders using a homodyne laser interferometer with 10 picometer uncertainty”. In: *Precision Engineering* 51 (2018), pp. 388–392. doi: 10.1016/j.precisioneng.2017.09.009 (cited on page 24).
- [102] L. Yu, G. Molnar, C. Werner, C. Weichert, R. Köning, H.-U. Danzebrink, J. Tan, and J. Flügge. “A single-beam 3DoF homodyne interferometer”. In: *Measurement Science and Technology* 31.8 (2020), p. 084006. doi: 10.1088/1361-6501/ab7f79 (cited on page 24).
- [103] T. Hausotte, B. Perle, U. Gerhardt, D. Dontsov, E. Manske, and G. Jäger. “Interference signal demodulation for nanopositioning and nanomeasuring machines”. In: *Measurement Science and Technology* 23.7 (2012), p. 074004. doi: 10.1088/0957-0233/23/7/074004 (cited on page 24).
- [104] M. Pisani and A. Giugni. “A portable picometer reference actuator with 100  $\mu\text{m}$  range, picometer resolution, subnanometer accuracy and submicroradian tip-tilt error for the characterization of measuring instruments at the nanoscale”. In: *Metrologia* 55.4 (2018), p. 541. doi: 10.1088/1681-7575/aaca6f (cited on page 24).
- [105] M. Pisani. “A homodyne Michelson interferometer with sub-picometer resolution”. In: *Measurement Science and Technology* 20.8 (2009), p. 084008. doi: 10.1088/0957-0233/20/8/084008 (cited on page 24).
- [106] R. Schödel, A. Yacoot, and A. Lewis. “The new mise en pratique for the metre — a review of approaches for the practical realization of traceable length metrology from  $10^{-11}\text{m}$  to  $10^{+13}\text{m}$ ”. In: *Metrologia* 58 (2021), p. 052002. doi: 10.1088/1681-7575/ac1456 (cited on page 24).
- [107] J. Lawall and E. Kessler. “Michelson interferometry with 10 pm accuracy”. In: *Review of Scientific Instruments* 71.7 (2000), p. 2669. doi: 10.1063/1.1150715 (cited on page 24).
- [108] M. Jin, S.-J. Tang, J.-H. Chen, X.-C. Yu, H. Shu, Y. Tao, A. K. Chen, X. Gong Q. and Wang, and Y.-F. Xiao. “1/f-noise-free optical sensing with an integrated heterodyne interferometer”. In: *Nature Communications* 12.1 (2021), pp. 1–7. doi: 10.1038/s41467-021-22271-4 (cited on page 24).
- [109] I. Verovnik and A. Likar. “The Michelson interferometer—how to detect invisible interference patterns”. In: *European Journal of Physics* 25.6 (2004), pp. 801–806. doi: 10.1088/0143-0807/25/6/012 (cited on page 24).
- [110] R. S. Sternberg and J. F. James. “A new type of Michelson interference spectrometer”. In: *Journal of Scientific Instruments* 41.4 (1964), pp. 225–226. doi: 10.1088/0950-7671/41/4/308 (cited on page 24).
- [111] J. V. Knuutila, P. T. Tikka, and M. M. Salomaa. “Scanning Michelson interferometer for imaging surface acoustic wave fields”. In: *Optics Letters* 25.9 (2000), pp. 613–615. doi: 10.1364/OL.25.000613 (cited on page 24).
- [112] A. V. Postnikov. “Interferometric technique with a reference scale”. In: *Applied Optics* 61.10 (2022), pp. 2869–2873. doi: 10.1364/AO.452544 (cited on page 24).
- [113] B. Mahon. “How Maxwell’s equations came to light”. In: *Nature Photonics* 9.1 (2015), pp. 2–4. doi: 10.1038/nphoton.2014.306 (cited on page 24).
- [114] S. Diner, D. Fargue, G. Lochak, and F. Selleri. *The Wave-particle dualism: a tribute to Louis de Broglie on his 90th birthday*. Vol. 3. Springer Science & Business Media, 2012. doi: 10.1086/289237 (cited on page 24).
- [115] M. J. Padgett. “Orbital angular momentum 25 years on [Invited]”. In: *Optics Express* 25.10 (2017), pp. 11265–11274. doi: 10.1364/OE.25.011265 (cited on pages 24, 26, 27, 31).
- [116] A. E. Siegman. *Lasers*. University Science Books, U.S., 1986 (cited on page 24).
- [117] R. Menzel. “Topics in Photonics”. In: *Photonics*. Springer, 2001, pp. 1–9 (cited on page 24).
- [118] K. Shimoda. *Introduction to laser physics*. Vol. 44. Springer, 2013. doi: 10.1070/QE1986v016n03ABEH006144 (cited on page 24).
- [119] K. F. Riley, M. P. Hobson, and S. J. Bence. *Mathematical Methods for Physics and Engineering: A Comprehensive Guide*. Cambridge University Press, 2006 (cited on page 25).
- [120] F. Pampaloni and J. Enderlein. “Gaussian, Hermite-Gaussian, and Laguerre-Gaussian beams: A primer”. In: *arXiv preprint physics/0410021* (2004) (cited on pages 25, 26, 28).



- [121] Y. Amnon. *Optical waves in crystals: propagation and control of laser radiation*. Wiley, New York, 1984 (cited on page 25).
- [122] J. H. Poynting. "XV. On the transfer of energy in the electromagnetic field". In: *Philosophical Transactions of the Royal Society of London* 175 (1884), pp. 343–361. doi: 10.1098/rstl.1884.0016 (cited on pages 25, 89).
- [123] L. Allen, M. W. Beijersbergen, R. J. Spreeuw, and J. P. Woerdman. "Orbital angular momentum of light and the transformation of Laguerre-Gaussian laser modes". In: *Physical Review A* 45.11 (1992), pp. 8185–8189. doi: 10.1103/physreva.45.8185 (cited on pages 26, 30).
- [124] V. Y. Bazhenov, M. S. Soskin, and M. V. Vasnetsov. "Screw dislocations in light wavefronts". In: *Journal of Modern Optics* 39.5 (1992), pp. 985–990. doi: 10.1080/09500349214551011 (cited on pages 26, 30).
- [125] A. M. Yao and M. J. Padgett. "Orbital angular momentum: origins, behavior and applications". In: *Advances in Optics and Photonics* 3.2 (2011), pp. 161–204. doi: 10.1364/aop.3.000161 (cited on pages 26, 32).
- [126] M. J. Padgett and L. Allen. "Light with a twist in its tail". In: *Contemporary Physics* 41.5 (2000), pp. 275–285. doi: 10.1080/001075100750012777 (cited on pages 26, 32).
- [127] N. B. Simpson, K. Dholakia, L. Allen, and M. J. Padgett. "Mechanical equivalence of spin and orbital angular momentum of light: an optical spanner". In: *Optics Letters* 22.1 (1997), pp. 52–54. doi: 10.1364/OL.22.000052 (cited on page 26).
- [128] R. C. Devlin, A. Ambrosio, N. A. Rubin, J. P. B. Mueller, and F. Capasso. "Arbitrary spin-to-orbital angular momentum conversion of light". In: *Science* 358.6365 (2017), pp. 896–901. doi: 10.1126/science.aao5392 (cited on pages 26, 30).
- [129] R. C. Devlin, A. Ambrosio, . Wintz, S. L. Oscurato, A. Y. Zhu, M. Khorasaninejad, J. Oh, P. Maddalena, and F. Capasso. "Spin-to-orbital angular momentum conversion in dielectric metasurfaces". In: *Optics Express* 25.1 (2017), pp. 377–393. doi: 10.1364/OE.25.000377 (cited on pages 26, 30).
- [130] Y. Shen, X. Wang, Z. Xie, C. Min, X. Fu, Q. Liu, M. Gong, and X. Yuan. "Optical vortices 30 years on: OAM manipulation from topological charge to multiple singularities". In: *Light: Science and Application* 8 (2019), p. 90. doi: 10.1038/s41377-019-0194-2 (cited on pages 27–31).
- [131] S. W. Hell and J. Wichmann. "Breaking the diffraction resolution limit by stimulated emission: stimulated-emission-depletion fluorescence microscopy". In: *Optics Letters* 19.11 (1994), pp. 780–782. doi: 10.1364/OL.19.000780 (cited on page 27).
- [132] T. A. Klar, S. Jakobs, M. Dyba, A. Egner, and S. W. Hell. "Fluorescence microscopy with diffraction resolution barrier broken by stimulated emission". In: *Proceedings of the National Academy of Sciences* 97.15 (2000), pp. 8206–8210. doi: 0.1073/pnas.97.15.8206 (cited on page 27).
- [133] L. I. Fochler. "Twisting the Light for Ultrasensitive Refractive Index Measurements". Master's Thesis. Ludwig Maximilians Universität München, 2021 (cited on pages 28, 32, 68, 69).
- [134] W.N. Plick and M. Krenn. "Physical meaning of the radial index of Laguerre-Gauss beams". In: *Physical Review A* 92.6 (2015). doi: 10.1103/PhysRevA.92.063841 (cited on page 29).
- [135] L. S. Penrose and R. Penrose. "Impossible objects: a special type of visual illusion". In: *British Journal of Psychology* 49 (1958), pp. 31–33. doi: 10.1111/j.2044-8295.1958.tb00634.x (cited on page 29).
- [136] M. W. Beijersbergen, L. Allen, H. E. L. O. Van der Veen, and J. P. Woerdman. "Astigmatic laser mode converters and transfer of orbital angular momentum". In: *Optics Communications* 96.1-3 (1993), pp. 123–132. doi: 10.1016/0030-4018(93)90535-D (cited on page 30).
- [137] M. W. Beijersbergen, R. P. C. Coerwinkel, M. Kristensen, and J. P. Woerdman. "Helical-wavefront laser beams produced with a spiral phaseplate". In: *Optics Communications* 112.5-6 (1994), pp. 321–327. doi: 10.1016/0030-4018(94)90638-6 (cited on page 30).
- [138] K. Sueda, G. Miyali, N. Miyanaaga, and Nakatsuka M. "Laguerre-Gaussian beams generated with a multilevel spiral phase plate for high intensity laser pulses". In: *Optics Express* 12.15 (2004), pp. 3548–3553. doi: 10.1364/OPEX.12.003548 (cited on pages 30, 66).
- [139] S. S. R. Oemrawsingh, J. A. W. van Houwelingen, E. R. Eliel, J. P. Woerdman, E. J. K. Verstegen, J. G. Kloosterboer, and G. W. 't Hooft. "Production and characterization of spiral phase plates for optical wavelengths". In: *Applied Optics* 43 (2004), pp. 688–694. doi: 10.1364/AO.43.000688 (cited on page 30).
- [140] M. Cano-Garcia, X. Quintana, J. M. Oton, and M. A. Geday. "Dynamic multilevel spiral phase plate generator". In: *Scientific Reports* 8.1 (2018), p. 15804. doi: 10.1038/s41598-018-34041-2 (cited on pages 30, 66).

- [141] S. A. Kennedy, M. J. Szabo, H. Teslow, J. Z. Porterfield, and E. R. I. Abraham. "Creation of Laguerre-Gaussian laser modes using diffractive optics". In: *Physical Review A* 66.4 (2002). doi: 10.1103/PhysRevA.66.043801 (cited on page 30).
- [142] L. Marrucci, E. Karimi, S. Slussarenko, B. Piccirillo, E. Santamato, E. Nagali, and F. Sciarrino. "Spin-to-orbital conversion of the angular momentum of light and its classical and quantum applications". In: *Journal of Optics* 13.6 (2011), p. 064001. doi: 10.1088/2040-8978/13/6/064001 (cited on page 30).
- [143] A. Jesacher, A. Schwaighofer, S. FÜRhapter, C. Maurer, S. Bernet, and M. Ritsch-Marte. "Wavefront correction of spatial light modulators using an optical vortex image". In: *Optics Express* 15.9 (2007), pp. 5801–5808. doi: 10.1364/OE.15.005801 (cited on page 30).
- [144] A. Forbes, A. Dudley, and M. McLaren. "Creation and detection of optical modes with spatial light modulators". In: *Advances in Optics and Photonics* 8.2 (2016), pp. 200–227. doi: 10.1364/AOP.8.000200 (cited on page 30).
- [145] C. Maurer, A. Jesacher, S. Bernet, and M. Ritsch-Marte. "What spatial light modulators can do for optical microscopy". In: *Laser & Photonics Reviews* 5.1 (2011), pp. 81–101. doi: 10.1002/lpor.200900047 (cited on page 30).
- [146] M. Mirhosseini, O. S. Magana-Loaiza, C. Chen, B. Rodenburg, M. Malik, and R. W. Boyd. "Rapid generation of light beams carrying orbital angular momentum". In: *Optics Express* 21.25 (2013), pp. 30196–30203. doi: 10.1364/OE.21.030196 (cited on page 30).
- [147] J. Leach and M. J. Padgett. "Observation of chromatic effects near a white-light vortex". In: *New Journal of Physics* 5.1 (2003), p. 154. doi: 10.1088/1367-2630/5/1/154 (cited on page 30).
- [148] H. I. Sztul, V. Kartazayev, and R. R. Alfano. "Laguerre-Gaussian supercontinuum". In: *Optics Letters* 31.18 (2006), pp. 2725–2727. doi: 10.1364/OL.31.002725 (cited on page 30).
- [149] N. Radwell, R. D. Hawley, J. B. Götte, and S. Franke-Arnold. "Achromatic vector vortex beams from a glass cone". In: *Nature Communications* 7.1 (2016), pp. 1–6. doi: 10.1038/nature13883 (cited on page 30).
- [150] I. Nape, B. Sephton, Y.-W. Huang, A. Vallés, C.-W. Qiu, A. Ambrosio, F. Capasso, and A. Forbes. "Enhancing the modal purity of orbital angular momentum photons". In: *APL Photonics* 5.7 (2020). doi: 10.1063/5.0005597 (cited on page 30).
- [151] H. Sroor, Y.-W. Huang, B. Sephton, D. Naidoo, A. Vallés, V. Ginis, C.-W. Qiu, A. Ambrosio, F. Capasso, and A. Forbes. "High-purity orbital angular momentum states from a visible metasurface laser". In: *Nature Photonics* 14.8 (2020), pp. 498–503. doi: 10.1038/s41566-020-0623-z (cited on page 30).
- [152] E. Karimi, S. A. Schulz, I. De Leon, H. Qassim, J. Upham, and R. W. Boyd. "Generating optical orbital angular momentum at visible wavelengths using a plasmonic metasurface". In: *Light: Science & Applications* 3.5 (2014), e167–e167. doi: 10.1038/lsa.2014.48 (cited on page 30).
- [153] T. Y. Fan. "Laser beam combining for high-power, high-radiance sources". In: *IEEE Journal of selected topics in Quantum Electronics* 11.3 (2005), pp. 567–577. doi: 10.1109/JSTQE.2005.850241. (cited on page 31).
- [154] J.R. Leger. "Laser beam combining: Theory and methods". In: *Conference on Lasers and Electro-Optics*. Optical Society of America. 2010, CThG1. doi: 10.1364/CLEO.2010.CThG1 (cited on page 31).
- [155] G. D. Goodno, C. P. Asman, J. Anderegg, S. Brosnan, E. C. Cheung, D. Hammons, H. Injeyan, H. Komine, W. H. Long, M. McClellan, S. J. McNaught, S. Redmond, R. Simpson, J. Sollee, M. Weber, S. B. Weiss, and M. Wickham. "Brightness-scaling potential of actively phase-locked solid-state laser arrays". In: *IEEE Journal of Selected Topics in Quantum Electronics* 13.3 (2007), pp. 460–472. doi: 10.1109/JSTQE.2007.896618. (cited on page 31).
- [156] P. Zhou, Z. Liu, X. Wang, Y. Ma, H. Ma, X. Xu, and S. Guo. "Coherent beam combining of fiber amplifiers using stochastic parallel gradient descent algorithm and its application". In: *IEEE Journal of Selected Topics in Quantum Electronics* 15.2 (2009), pp. 248–256. doi: 10.1109/JSTQE.2008.2010231 (cited on page 31).
- [157] C. X. Yu, S. J. Augst, S. M. Redmond, K. C. Goldizen, D. V. Murphy, A. Sanchez, and T. Y. Fan. "Coherent combining of a 4 kW, eight-element fiber amplifier array". In: *Optics Letters* 36.14 (2011), pp. 2686–2688. doi: 10.1364/OL.36.002686 (cited on page 31).
- [158] E. Seise, A. Klenke, J. Limpert, and A. Tünnermann. "Coherent addition of fiber-amplified ultrashort laser pulses". In: *Optics Express* 18.26 (2010), pp. 27827–27835. doi: 10.1364/OE.18.027827 (cited on page 31).

- [159] A. Flores, I. Dajani, R. H. Holten, T. Ehrenreich, and B. T. Anderson. "Multi-kilowatt diffractive coherent combining of pseudorandom-modulated fiber amplifiers". In: *Optical Engineering* 55.9 (2016), p. 096101. doi: 10.1117/1.OE.55.9.096101 (cited on page 31).
- [160] X. Peng C.and Liang, R. Liu, W. Li, and R. Li. "High-precision active synchronization control of high-power, tiled-aperture coherent beam combining". In: *Optics Letters* 42.19 (2017), pp. 3960–3963. doi: 10.1364/OL.42.003960 (cited on page 31).
- [161] L.-G. Wang, L.-Q. Wang, and S.-Y. Zhu. "Formation of optical vortices using coherent laser beam arrays". In: *Optics Communications* 282.6 (2009), pp. 1088–1094. doi: j.optcom.2008.12.004 (cited on page 31).
- [162] X. Chu, Q. Sun, J. Wang, P. Lü, W. Xie, and X. Xu. "Generating a Bessel-Gaussian beam for the application in optical engineering". In: *Scientific Reports* 5.1 (2015), pp. 1–8. doi: 10.1038/srep18665 (cited on page 31).
- [163] T. Hou, D. Zhi, R. Tao, Y. Ma, . Zhou, and Z. Liu. "Spatially-distributed orbital angular momentum beam array generation based on greedy algorithms and coherent combining technology". In: *Optics Express* 26.12 (2018), pp. 14945–14958. doi: 10.1364/OE.26.014945 (cited on page 31).
- [164] Y. Yang, Y. Dong, C. Zhao, and Y. Cai. "Generation and propagation of an anomalous vortex beam". In: *Optics Letters* 38.24 (2013), pp. 5418–5421. doi: 10.1364/OL.38.005418 (cited on page 31).
- [165] V. P. Aksenov, . V. Dudorov, and V. V. Kolosov. "Properties of vortex beams formed by an array of fibre lasers and their propagation in a turbulent atmosphere". In: *Quantum Electronics* 46.8 (2016), p. 726. doi: 10.1070/QEL16088 (cited on page 31).
- [166] S. L. Lachinova and M. A. Vorontsov. "Exotic laser beam engineering with coherent fiber-array systems". In: *Journal of Optics* 15.10 (2013), p. 105501. doi: 10.1088/2040-8978/15/10/105501 (cited on page 31).
- [167] V.V. Dudorov, V.P. Aksenov, V.V. Kolosov, M.E. Levitsky, T.D. Petukhov, and A.P. Rostov. "Generation of vortex and partially coherent laser beams based on fiber array coherent combining". In: *Environmental Effects on Light Propagation and Adaptive Systems*. Vol. 10787. International Society for Optics and Photonics. 2018, p. 107870M. doi: 10.1117/12.2502158 (cited on page 31).
- [168] D. Zhi, T. Hou, P. Ma, Y. Ma, P. Zhou, R. Tao, X. Wang, and L. Si. "Comprehensive investigation on producing high-power orbital angular momentum beams by coherent combining technology". In: *High Power Laser Science and Engineering* 7 (2019). doi: 10.1017/hpl.2019.17 (cited on page 31).
- [169] T. Hou, Y. An, Q. Chang, P. Ma, J. Li, L. Huang, D. Zhi, J. Wu, R. Su, Y. Ma, and P. Zhou. "Deep-learning-assisted, two-stage phase control method for high-power mode-programmable orbital angular momentum beam generation". In: *Photonics Research* 8.5 (2020), pp. 715–722. doi: 10.1364/PRJ.388551 (cited on pages 31, 89).
- [170] H. Tünnermann and A. Shirakawa. "Deep reinforcement learning for coherent beam combining applications". In: *Optics Express* 27.17 (2019), pp. 24223–24230. doi: 10.1364/OE.27.024223 (cited on page 31).
- [171] T. Hou, Y. An, Q. Chang, P. Ma, J. Li, D. Zhi, L. Huang, R. Su, J. Wu, Y. Ma, and P. Zhou. "Deep-learning-based phase control method for tiled aperture coherent beam combining systems". In: *High Power Laser Science and Engineering* 7 (2019). doi: 10.1017/hpl.2019.46 (cited on page 31).
- [172] N. Cvijetic, G. Milione, E. Ip, and T. Wang. "Detecting Lateral Motion using Light's Orbital Angular Momentum". In: *Scientific Reports* 5 (2015), p. 15422. doi: 10.1038/srep15422 (cited on page 31).
- [173] S. Bernet, A. Jesacher, S. Fürhapter, C. Maurer, and M. Ritsch-Marte. "Quantitative imaging of complex samples by spiral phase contrast microscopy". In: *Optics Express* 14.9 (2006), pp. 3792–3805. doi: 10.1364/OE.14.003792 (cited on page 31).
- [174] A. E. Willner, H. Huang, Y. Yan, Y. Ren, N. Ahmed, G. Xie, C. Bao, L. Li, Y. Cao, Z. Zhao, J. Wang, M. P. J. Lavery, M. Tur, S. Ramachandran, A. F. Molisch, N. Ashrafi, and S. Ashrafi. "Optical communications using orbital angular momentum beams". In: *Advances in Optics and Photonics* 7.1 (2015), pp. 66–106. doi: 10.1364/AOP.7.000066 (cited on page 31).
- [175] G. Gibson, J. Courtial, M. J. Padgett, M. Vasnetsov, V. Pas'ko, S. M. Barnett, and S. Franke-Arnold. "Free-space information transfer using light beams carrying orbital angular momentum". In: *Optics Express* 12.22 (2004), pp. 5448–5456. doi: 10.1364/OPEX.12.005448 (cited on page 31).
- [176] J. Wang, J.-Y. Yang, I. M. Fazal, N. Ahmed, Y. Yan, H. Huang, Y. Ren, Y. Yue, S. Dolinar, M. Tur, and A. E. Willner. "Terabit free-space data transmission employing orbital angular momentum multiplexing". In: *Nature Photonics* 6.7 (2012), pp. 488–496. doi: 10.1038/ncomms5876 (cited on page 31).

- [177] Y. Yan, G. Xie, M. P. J. Lavery, H. Huang, N. Ahmed, C. Bao, Y. Ren, Y. Cao, L. Li, Z. Zhao, A. F. Molisch, M. Tur, M. J. Padgett, and A. E. Willner. “High-capacity millimetre-wave communications with orbital angular momentum multiplexing”. In: *Nature Communications* 5.1 (2014), pp. 1–9. doi: [10.1038/ncomms5876](https://doi.org/10.1038/ncomms5876) (cited on page 31).
- [178] A. Ashkin, J. M. Dziedzic, J. E. Bjorkholm, and S. Chu. “Observation of a single-beam gradient force optical trap for dielectric particles”. In: *Optics Letters* 11.5 (1986), pp. 288–290. doi: [10.1364/OL.11.000288](https://doi.org/10.1364/OL.11.000288) (cited on page 31).
- [179] W. D. Phillips. “Nobel Lecture: Laser cooling and trapping of neutral atoms”. In: *Reviews of Modern Physics* 70.3 (1998), p. 721. doi: [10.1103/RevModPhys.70.721](https://doi.org/10.1103/RevModPhys.70.721) (cited on page 31).
- [180] H. He, M. E. J. Friese, N. R. Heckenberg, and H. Rubinsztein-Dunlop. “Direct observation of transfer of angular momentum to absorptive particles from a laser beam with a phase singularity”. In: *Physical Review Letters* 75.5 (1995), p. 826. doi: [10.1103/PhysRevLett.75.826](https://doi.org/10.1103/PhysRevLett.75.826) (cited on page 31).
- [181] M. E. J. Friese, T. A. Nieminen, N. R. Heckenberg, and H. Rubinsztein-Dunlop. “Optical alignment and spinning of laser-trapped microscopic particles”. In: *Nature* 394.6691 (1998), pp. 348–350. doi: [10.1038/28566](https://doi.org/10.1038/28566) (cited on page 31).
- [182] V. Garcés-Chávez, D. McGloin, M. J. Padgett, W. Dultz, H. Schmitzer, and K. Dholakia. “Observation of the transfer of the local angular momentum density of a multiringed light beam to an optically trapped particle”. In: *Physical Review Letters* 91.9 (2003), p. 093602. doi: [10.1103/PhysRevLett.91.093602](https://doi.org/10.1103/PhysRevLett.91.093602) (cited on page 31).
- [183] C. Maurer, A. Jesacher, S. Fürhapter, S. Bernet, and M. Ritsch-Marte. “Tailoring of arbitrary optical vector beams”. In: *New Journal of Physics* 9.3 (2007), p. 78. doi: [10.1088/1367-2630/9/3/078](https://doi.org/10.1088/1367-2630/9/3/078) (cited on page 31).
- [184] K. J. Mitchell, S. Turtaev, M. J. Padgett, T. Cizmar, and D. B Phillips. “High-speed spatial control of the intensity, phase and polarisation of vector beams using a digital micro-mirror device”. In: *Optics Express* 24.25 (2016), pp. 29269–29282. doi: [10.1364/OE.24.029269](https://doi.org/10.1364/OE.24.029269) (cited on page 31).
- [185] Y.-F. Chen, K.-F. Huang, H. C. Lai, and Y.-P. Lan. “Observation of vector vortex lattices in polarization states of an isotropic microcavity laser”. In: *Physical Review Letters* 90.5 (2003), p. 053904. doi: [10.1103/PhysRevLett.90.053904](https://doi.org/10.1103/PhysRevLett.90.053904) (cited on page 31).
- [186] Y.-F. Chen, T.-H. Lu, and K.-F. Huang. “Observation of spatially coherent polarization vector fields and visualization of vector singularities”. In: *Physical Review Letters* 96.3 (2006), p. 033901. doi: [10.1103/PhysRevLett.96.033901](https://doi.org/10.1103/PhysRevLett.96.033901) (cited on page 31).
- [187] M. Uchida and A. Tonomura. “Generation of electron beams carrying orbital angular momentum”. In: *Nature* 464.7289 (2010), pp. 737–739. doi: [10.1038/nature08904](https://doi.org/10.1038/nature08904) (cited on page 31).
- [188] B. J. McMorran, A. Agrawal, I. M. Anderson, A. A. Herzing, H. J. Lezec, J. J. McClelland, and J. Unguris. “Electron vortex beams with high quanta of orbital angular momentum”. In: *Science* 331.6014 (2011), pp. 192–195. doi: [10.1126/science.1198804](https://doi.org/10.1126/science.1198804) (cited on page 31).
- [189] J. Verbeeck, H. Tian, and P. Schattschneider. “Production and application of electron vortex beams”. In: *Nature* 467.7313 (2010), pp. 301–304. doi: [10.1038/nature09366](https://doi.org/10.1038/nature09366) (cited on page 31).
- [190] C. Greenshields, R. L. Stamps, and S. Franke-Arnold. “Vacuum Faraday effect for electrons”. In: *New Journal of Physics* 14.10 (2012), p. 103040. doi: [10.1088/1367-2630/14/10/103040](https://doi.org/10.1088/1367-2630/14/10/103040) (cited on page 31).
- [191] R. Fickler, R. Lapkiewicz, W. N. Plick, M. Krenn, C. Schaeff, S. Ramelow, and A. Zeilinger. “Quantum Entanglement of High Angular Momenta”. In: *Science* 338 (2012), pp. 640–643. doi: [10.1126/science.1227193](https://doi.org/10.1126/science.1227193) (cited on page 31).
- [192] R. Fickler, G. Campbell, B. Buchler, P. K. Lam, and A. Zeilinger. “Quantum entanglement of angular momentum states with quantum numbers up to 10,010”. In: *Proceedings of the National Academy of Sciences* 113.48 (2016), pp. 13642–13647. doi: [10.1073/pnas.1616889113](https://doi.org/10.1073/pnas.1616889113) (cited on page 31).
- [193] M. P. J. Lavery, A. Dudley, A. Forbes, J. Courtial, and M. J. Padgett. “Robust interferometer for the routing of light beams carrying orbital angular momentum”. In: *New Journal of Physics* 13.9 (2011), p. 093014. doi: [10.1088/1367-2630/13/9/093014](https://doi.org/10.1088/1367-2630/13/9/093014) (cited on page 31).
- [194] P. Senthikumar, Jan Masajada, and Shunichi Sato. “Interferometry with Vortices”. In: *International Journal of Optics* 2012 (2012), pp. 1–18. doi: [10.1155/2012/517591](https://doi.org/10.1155/2012/517591) (cited on page 31).
- [195] A. Popiolek-Masajada, M. Borwinska, and W. Fraczek. “Testing a new method for small-angle rotation measurements with the optical vortex interferometer”. In: *Measurement Science and Technology* 17.4 (2006), pp. 653–658. doi: [10.1088/0957-0233/17/4/007](https://doi.org/10.1088/0957-0233/17/4/007) (cited on page 31).

- [196] S. Barreiro, J. W. Tabosa, H. Failache, and A. Lezama. “Spectroscopic observation of the rotational Doppler effect”. In: *Physical Review Letters* 97.11 (2006), p. 113601. doi: [10.1103/PhysRevLett.97.113601](https://doi.org/10.1103/PhysRevLett.97.113601) (cited on page 31).
- [197] A. Allocca, A. Gatto, M. Tacca, R. A Day, M. Barsuglia, G. Pillant, C. Buy, and G. Vajente. “Higher-order Laguerre-Gauss interferometry for gravitational-wave detectors with in situ mirror defects compensation”. In: *Physical Review D* 92.10 (2015), p. 102002. doi: [10.1103/PhysRevD.92.102002](https://doi.org/10.1103/PhysRevD.92.102002) (cited on page 31).
- [198] A. Gatto, M. Tacca, F. Kéfélian, C. Buy, and M. Barsuglia. “Fabry-Pérot-Michelson interferometer using higher-order Laguerre-Gauss modes”. In: *Physical Review D* 90.12 (2014). doi: [10.1103/PhysRevD.90.122011](https://doi.org/10.1103/PhysRevD.90.122011) (cited on page 31).
- [199] M. Granata, C. Buy, R. Ward, and M. Barsuglia. “Higher-order Laguerre-Gauss mode generation and interferometry for gravitational wave detectors”. In: *Physical Review Letters* 105.23 (2010), p. 231102. doi: [10.1103/PhysRevLett.105.231102](https://doi.org/10.1103/PhysRevLett.105.231102) (cited on page 31).
- [200] B. Sorazu, P. J. Fulda, B. W. Barr, A. S. Bell, C. Bond, L. Carbone, A. Freise, S. Hild, S. H. Huttner, J. Jacarthur, and K. A. Strain. “Experimental test of higher-order Laguerre-Gauss modes in the 10 m Glasgow prototype interferometer”. In: *Classical and Quantum Gravity* 30 (2013), p. 035004. doi: [10.1088/0264-9381/30/3/035004](https://doi.org/10.1088/0264-9381/30/3/035004) (cited on page 31).
- [201] S. Fürhapter, A. Jesacher, S. Bernet, and M. Ritsch-Marte. “Spiral interferometry”. In: *Optics Letters* 30.15 (2005), p. 1953. doi: [10.1364/OL.30.001953](https://doi.org/10.1364/OL.30.001953) (cited on page 31).
- [202] J. Masajada, M. Leniec, E. Jankowska, H. Theinpont, H. Ottevaere, and V. Gomez. “Deep microstructure topography characterization with optical vortex interferometers”. In: *Optics Express* 16.23 (2008), pp. 19179–19191. doi: [10.1364/OE.16.019179](https://doi.org/10.1364/OE.16.019179) (cited on page 31).
- [203] L. Chen, W. Zhang, Q. Lu, and X. Lin. “Making and identifying optical superpositions of high orbital angular momenta”. In: *Physical Review A* 88.5 (2013). doi: [10.1103/PhysRevA.88.053831](https://doi.org/10.1103/PhysRevA.88.053831) (cited on page 32).
- [204] J. Guo, B. Guo, R. Fan, W. Zhang, Y. Wang, L. Zhang, and P. Zhang. “Measuring topological charges of Laguerre-Gaussian vortex beams using two improved Mach-Zehnder interferometers”. In: *Optical Engineering* 55.3 (2016). doi: [10.1117/1.Oe.55.3.035104](https://doi.org/10.1117/1.Oe.55.3.035104) (cited on page 32).
- [205] O. Emile and J. Emile. “Naked eye picometer resolution in a Michelson interferometer using conjugated twisted beams”. In: *Optics Letters* 42.2 (2017), pp. 354–357. doi: [10.1364/OL.42.000354](https://doi.org/10.1364/OL.42.000354) (cited on pages 32, 66).
- [206] D. Polder and M. Van Hove. “Theory of Radiative Heat Transfer between Closely Spaced Bodies”. In: *Physical Review B* 4.10 (1971), pp. 3303–3314. doi: [10.1103/PhysRevB.4.3303](https://doi.org/10.1103/PhysRevB.4.3303) (cited on page 36).
- [207] A. R. Clapp, I. L. Medintz, and H. Mattoussi. “Förster resonance energy transfer investigations using quantum-dot fluorophores”. In: *ChemPhysChem* 7.1 (2006), pp. 47–57. doi: [10.1002/cphc.200500217](https://doi.org/10.1002/cphc.200500217) (cited on page 36).
- [208] S. M. Sadeghi, W. J. Wing, R. R. Gutha, J. S. Wilt, and J. Z. Wu. “Balancing silicon/aluminum oxide junctions for super-plasmonic emission enhancement of quantum dots via plasmonic metafilms”. In: *Nanoscale* 10.10 (2018), pp. 4825–4832. doi: [10.1039/C7NR09396A](https://doi.org/10.1039/C7NR09396A) (cited on page 36).
- [209] M. Tschikin, S. A. Biehs, F. S. S. Rosa, and P. Ben-Abdallah. “Radiative cooling of nanoparticles close to a surface”. In: *The European Physical Journal B* 85.7 (2012). doi: [10.1140/epjb/e2012-30219-7](https://doi.org/10.1140/epjb/e2012-30219-7) (cited on page 36).
- [210] B. Guha, C. Otey, C. B. Poitras, S. Fan, and M. Lipson. “Near-field radiative cooling of nanostructures”. In: *Nano Letters* 12.9 (2012), pp. 4546–50. doi: [10.1021/nl301708e](https://doi.org/10.1021/nl301708e) (cited on page 36).
- [211] ACM COATINGS GmbH. *Metal Velvet*. 2022. url: [de.acktar.com/produkt/metal-velvet/](https://de.acktar.com/produkt/metal-velvet/) (visited on 04/27/2022) (cited on page 38).
- [212] Optiforms. *Infrared imaging components*. 2022. url: [optiforms.com/ir-imaging/#electrodeposited-gold](https://optiforms.com/ir-imaging/#electrodeposited-gold) (visited on 04/27/2022) (cited on page 42).
- [213] N. M. Kerschbaumer, S. Niedermaier, T. Lohmüller, and J. Feldmann. “Contactless and spatially structured cooling by directing thermal radiation”. In: *Scientific Reports* 11.1 (2021), pp. 1–8. doi: [10.1364/OPN.30.11.000032](https://doi.org/10.1364/OPN.30.11.000032) (cited on pages 43, 45, 47, 53, 58, 59, 61).
- [214] J. Carvill. *Mechanical engineer’s data handbook*. Butterworth-Heinemann, 1994 (cited on page 48).

- [215] Imetra. *Borosilicate Glass Material Properties*. 2022. url: [imetra.com/borosilicate-glass-material-properties/](https://imetra.com/borosilicate-glass-material-properties/) (visited on 07/27/2022) (cited on page 49).
- [216] R. L. Hays. "The thermal conductivity of leaves". In: *Planta* 125.3 (1975), pp. 281–287. doi: [10.1007/BF00385604](https://doi.org/10.1007/BF00385604) (cited on page 55).
- [217] M. J. Powell-Palm, A. Koh-Bell, and B. Rubinsky. "Isochoric conditions enhance stability of metastable supercooled water". In: *Applied Physics Letters* 116.12 (2020), p. 123702. doi: [10.1063/1.5145334](https://doi.org/10.1063/1.5145334) (cited on pages 56, 57).
- [218] E. J. Langham and B. J. Mason. "The heterogeneous and homogeneous nucleation of supercooled water". In: *Proceedings of the Royal Society of London. Series A. Mathematical and Physical Sciences* 247.1251 (1958), pp. 493–504. doi: [10.1098/rspa.1958.0207](https://doi.org/10.1098/rspa.1958.0207) (cited on page 56).
- [219] G. Vali. "Quantitative evaluation of experimental results an the heterogeneous freezing nucleation of supercooled liquids". In: *Journal of Atmospheric Sciences* 28.3 (1971), pp. 402–409. doi: [10.1175/1520-0469\(1971\)028<0402:QEOERA>2.0.CO;2](https://doi.org/10.1175/1520-0469(1971)028<0402:QEOERA>2.0.CO;2) (cited on page 56).
- [220] M. Wisniewski, M. Fuller, R. Margesin, and F. Schinner. "Cold-adapted organisms. Ecology, physiology, enzymology and molecular biology". In: (1999) (cited on page 56).
- [221] P. W. Wilson, A. F. Heneghan, and A. D. J. Haymet. "Ice nucleation in nature: supercooling point (SCP) measurements and the role of heterogeneous nucleation". In: *Cryobiology* 46.1 (2003), pp. 88–98. doi: [10.1016/S0011-2240\(02\)00182-7](https://doi.org/10.1016/S0011-2240(02)00182-7) (cited on page 56).
- [222] W. Que, X. Hu, M. Fujino, H. Terayama, K. Sakabe, N. Fukunishi, P. Zhu, S.-Q. Yi, Y. Yamada, L. Zhong, and X.-K. Li. "Prolonged cold ischemia time in mouse heart transplantation using supercooling preservation". In: *Transplantation* 104.9 (2020), pp. 1879–1889. doi: [10.1097/TP.0000000000003089](https://doi.org/10.1097/TP.0000000000003089) (cited on page 56).
- [223] T. A. Berendsen, B. G. Bruinsma, C. F. Puts, N. Saeidi, O. B. Usta, B. E. Uygun, M.-L. Izamis, M. Toner, M. L. Yarmush, and K. Uygun. "Supercooling enables long-term transplantation survival following 4 days of liver preservation". In: *Nature Medicine* 20.7 (2014), pp. 790–793. doi: [10.1038/nm.3588](https://doi.org/10.1038/nm.3588) (cited on page 56).
- [224] R. J. de Vries, S. N. Tessier, P. D. Banik, S. Nagpal, S. E. J. Cronin, S. Ozer, E. O. A. Hafiz, T. M. van Gulik, M. L. Yarmush, J. F. Markmann, M. Toner, H. Yeh, and K. Uygun. "Supercooling extends preservation time of human livers". In: *Nature Biotechnology* 37.10 (2019), pp. 1131–1136. doi: [10.1038/s41587-019-0223-y](https://doi.org/10.1038/s41587-019-0223-y) (cited on page 56).
- [225] T. Kang, Y. You, and S. Jun. "Supercooling preservation technology in food and biological samples: A review focused on electric and magnetic field applications". In: *Food Science and Biotechnology* 29.3 (2020), pp. 303–321. doi: [10.1007/s10068-020-00750-6](https://doi.org/10.1007/s10068-020-00750-6) (cited on page 57).
- [226] G. Jacoby, K. Cohen, K. Barkan, Y. Talmon, D. Peer, and R. Beck. "Metastability in lipid based particles exhibits temporally deterministic and controllable behavior". In: *Scientific Reports* 5.1 (2015), pp. 1–7. doi: [10.1038/srep09481](https://doi.org/10.1038/srep09481) (cited on page 57).
- [227] M.-C. Huang, B.-R. Chen, M.-J. Hsiao, and S.-L. Chen. "Application of thermal battery in the ice storage air-conditioning system as a subcooler". In: *International Journal of Refrigeration* 30.2 (2007), pp. 245–253. doi: [10.1016/j.ijrefrig.2006.07.027](https://doi.org/10.1016/j.ijrefrig.2006.07.027) (cited on page 57).
- [228] E. Oró, A. de Gracia, A. Castell, M. M. Farid, and L. F. Cabeza. "Review on phase change materials (PCMs) for cold thermal energy storage applications". In: *Applied Energy* 99 (2012), pp. 513–533. doi: [10.1016/j.apenergy.2012.03.058](https://doi.org/10.1016/j.apenergy.2012.03.058) (cited on page 57).
- [229] D. Zhou, C. Y. Zhao, and Y. Tian. "Review on thermal energy storage with phase change materials (PCMs) in building applications". In: *Applied Energy* 92 (2012), pp. 593–605. doi: [10.1016/j.apenergy.2011.08.025](https://doi.org/10.1016/j.apenergy.2011.08.025) (cited on page 57).
- [230] A. Safari, R. Saidur, F. A. Sulaiman, Y. Xu, and J. Dong. "A review on supercooling of Phase Change Materials in thermal energy storage systems". In: *Renewable and Sustainable Energy Reviews* 70 (2017), pp. 905–919. doi: [10.1016/j.rser.2016.11.272](https://doi.org/10.1016/j.rser.2016.11.272) (cited on page 57).
- [231] S. Abramov, K. Shah, L. Weißenstein, and H. P. Karbstein. "Effect of alkane chain length on crystallization in emulsions during supercooling in quiescent systems and under mechanical stress". In: *Processes* 6.1 (2018), p. 6. doi: [10.3390/pr6010006](https://doi.org/10.3390/pr6010006) (cited on page 60).

- [232] N. M. Kerschbaumer, L. I. Fochler, M. Reichensperner, S. Rieger, M. Fedoruk, J. Feldmann, and T. Lohmüller. "Twisted light Michelson interferometer for high precision refractive index measurements". In: *Optics Express* 30.16 (2022), pp. 29722–29734. doi: 10.1364/OE.462782 (cited on pages 64, 66, 71–73, 75, 77, 79, 81–87).
- [233] Q. Jia, X. Qiu, Z. Wu, W. Zhang, and L. Chen. "Transferring linear motion of an optical wedge to rotational frequency shift in an orbital angular momentum interferometer". In: *Applied Physics Letters* 111.9 (2017), p. 091102. doi: 10.1063/1.4995366 (cited on pages 32, 66).
- [234] G. Verma and G. Yadav. "Compact picometer-scale interferometer using twisted light". In: *Optics Letters* 44.14 (2019), pp. 3594–3597. doi: 10.1364/OL.44.003594 (cited on pages 66, 80, 91).
- [235] R. A. Sampaio and R. M. de Souza. "Vibration Analysis of a Residential Building". In: *MATEC Web of Conferences*. Vol. 24. EDP Sciences. 2015, p. 09007. doi: 10.1051/mateconf/20152409007 (cited on page 72).
- [236] D. P. Connolly, P. Galvín, B. Olivier, A. Romero, and G. Kouroussis. "A 2.5 D time-frequency domain model for railway induced soil-building vibration due to railway defects". In: *Soil Dynamics and Earthquake Engineering* 120 (2019), pp. 332–344. doi: 10.1016/j.soildyn.2019.01.030 (cited on page 72).
- [237] D. P. Subedi, D. R. Adhikari, U. M. Joshi, H. N. Poudel, and B. Niraula. "Study of temperature and concentration dependence of refractive index of liquids using a novel technique". In: *Kathmandu University Journal of Science, Engineering and Technology* 2 (2006) (cited on pages 76, 79).
- [238] P. Schiebener, J. Straub, J. M. H. Levelt Sengers, and J. S. Gallagher. "Refractive index of water and steam as function of wavelength, temperature and density". In: *Journal of Physical and Chemical Reference Data* 19.3 (1990), pp. 677–717. doi: 10.1063/1.555859 (cited on pages 79, 80).
- [239] J. F. Domenegueti, A. A. Andrade, V. Pilla, and S. C. Zilio. "Simultaneous measurement of thermo-optic and thermal expansion coefficients with a single arm double interferometer". In: *Optics Express* 25.1 (2017), pp. 313–319. doi: 10.1364/OE.25.000313 (cited on pages 79, 80).
- [240] Y. H. Kim, S. J. Park, S.-W. Jeon, S. Ju, C.-S. Park, W.-T. Han, and B. L. Lee. "Thermo-optic coefficient measurement of liquids based on simultaneous temperature and refractive index sensing capability of a two-mode fiber interferometric probe". In: *Optics Express* 20.21 (2012), pp. 23745–23754. doi: 10.1364/OE.20.023744 (cited on pages 79, 80).
- [241] Merck Product Z801674. *Specac sealed flow cell for IR spectroscopy*. 2022. url: [sigmaaldrich.com/DE/de/product/sial/z801674](https://sigmaaldrich.com/DE/de/product/sial/z801674) (visited on 07/14/2022) (cited on page 80).
- [242] C.-Y. Tan and Y.-X. Huang. "Dependence of Refractive Index on Concentration and Temperature in Electrolyte Solution, Polar Solution, Nonpolar Solution, and Protein Solution". In: *Journal of Chemical & Engineering Data* 60.10 (2015), pp. 2827–2833. doi: 10.1021/acs.jced.5b00018 (cited on pages 80, 83, 85, 86).
- [243] Misto, E. Purwandari, Supriyadi, A. Arkundato, L. Rohman, and B. E. Cahyono. "Analyses of Concentration and Wavelength Dependent Refractive Index of Sugar Solution Using Sellmeier Equation". In: *Journal of Physics: Conference Series* 1825 (2021), p. 012030. doi: 10.1088/1742-6596/1825/1/012030 (cited on pages 80, 83, 86, 87).
- [244] J. B. Cole and J. C. Florez. "Genetics of diabetes mellitus and diabetes complications". In: *Nature Reviews Nephrology* 16.7 (2020), pp. 377–390. doi: 10.1038/s41581-020-0278-5 (cited on page 83).
- [245] D. Bruen, C. Delaney, L. Florea, and D. Diamond. "Glucose Sensing for Diabetes Monitoring: Recent Developments". In: *Sensors* 17.8 (2017), p. 1866. doi: 10.3390/s17081866 (cited on page 83).
- [246] J. Zhang, W. Hodge, C. Hutnick, and X. Wang. "Noninvasive diagnostic devices for diabetes through measuring tear glucose". In: *Journal of Diabetes Science and Technology* 5.1 (2011), pp. 166–172. doi: 10.1177/193229681100500123 (cited on page 88).
- [247] Y. Kostov, X. Ge, G. Rao, and L. Tolosa. "Portable system for the detection of micromolar concentrations of glucose". In: *Measurement Science and Technology* 25.2 (2014), p. 025701. doi: 10.1088/0957-0233/25/2/025701 (cited on page 88).
- [248] D. R. Vogus, V. Mansard, M. V. Rapp, and T. M. Squires. "Measuring concentration fields in microfluidic channels in situ with a Fabry-Perot interferometer". In: *Lab on a Chip* 15.7 (2015), pp. 1689–1696. doi: 10.1039/c5lc00095e (cited on page 88).

- [249] A. Crespi, Y. Gu, B. Ngamsom, H. J. Hoekstra, C. Dongre, M. Pollnau, R. Ramponi, H. H. van den Vlekkert, P. Watts, G. Cerullo, and R. Osellame. "Three-dimensional Mach-Zehnder interferometer in a microfluidic chip for spatially-resolved label-free detection". In: *Lab on a Chip* 10.9 (2010), pp. 1167–1173. doi: 10.1039/b920062b (cited on page 88).
- [250] R. G. Heideman and P. V. Lambeck. "Remote opto-chemical sensing with extreme sensitivity: design, fabrication and performance of a pigtailed integrated optical phase-modulated Mach-Zehnder interferometer system". In: *Sensors and Actuators B: Chemical* 61.1 (1999), pp. 100–127. doi: 10.1016/S0925-4005(99)00283-X (cited on pages 88, 90).
- [251] J. Tian, Y. Lu, Q. Zhang, and M. Han. "Microfluidic refractive index sensor based on an all-silica in-line Fabry-Perot interferometer fabricated with microstructured fibers". In: *Optics Express* 21.5 (2013), pp. 6633–6639. doi: 10.1364/OE.21.006633 (cited on page 88).
- [252] T. Wei, Y. Han, Y. Li, H. L. Tsai, and H. Xiao. "Temperature-insensitive miniaturized fiber inline Fabry-Perot interferometer for highly sensitive refractive index measurement". In: *Optics Express* 16 (2008), pp. 5764–5769. doi: 10.1364/OE.16.005764 (cited on page 88).
- [253] S. Ghosh and B. M. A. Rahman. "Design of on-chip hybrid plasmonic Mach-Zehnder interferometer for temperature and concentration detection of chemical solution". In: *Sensors and Actuators B: Chemical* 279 (2019), pp. 490–502. doi: 10.1016/j.snb.2018.09.070 (cited on page 88).
- [254] G. H. Cross, A. A. Reeves, S. Brand, J. F. Popplewell, L. L. Peel, M. J. Swann, and N. J. Freeman. "A new quantitative optical biosensor for protein characterisation". In: *Biosensors & Bioelectronics* 19.4 (2003), pp. 383–390. doi: 10.1016/s0956-5663(03)00203-3 (cited on page 88).
- [255] D. J. Bornhop, J. C. Latham, A. Kussrow, D. A. Markov, R. D. Jones, and H. S. Sorensen. "Free-solution, label-free molecular interactions studied by back-scattering interferometry". In: *Science* 317.5845 (2007), pp. 1732–1736. doi: 10.1126/science.1146559 (cited on page 88).
- [256] A. Brandenburg. "Differential refractometry by an integrated-optical Young interferometer". In: *Sensors and Actuators B: Chemical* 39 (1997), pp. 266–271. doi: 10.1016/S0925-4005(97)80216-X (cited on page 88).
- [257] K. E. You, N. Uddin, T. H. Kim, Q. H. Fan, and H. J. Yoon. "Highly sensitive detection of biological substances using microfluidic enhanced Fabry-Perot etalon-based optical biosensors." In: *Sensors and Actuators B: Chemical* 277 (2018), pp. 62–68. doi: 10.1016/j.snb.2018.08.146 (cited on page 88).
- [258] A. Ymeti, J. S. Kanger, J. Greve, G. A. Besselink, P. V. Lambeck, R. Wijn, and R. G. Heideman. "Integration of microfluidics with a four-channel integrated optical Young interferometer immunosensor". In: *Biosens. Bioelectron.* 20.7 (2005), pp. 1417–21. doi: 10.1016/j.bios.2004.04.015 (cited on page 88).
- [259] H. Sobral and M. Pena-Gomar. "Determination of the refractive index of glucose-ethanol-water mixtures using spectroscopic refractometry near the critical angle". In: *Applied Optics* 54.28 (2015), pp. 8453–8458. doi: 10.1364/AO.54.008453 (cited on page 88).
- [260] C. Wu, M. L. Tse, Z. Liu, B. O. Guan, A. P. Zhang, C. Lu, and H. Y. Tam. "In-line microfluidic integration of photonic crystal fibres as a highly sensitive refractometer". In: *Analyst* 139.21 (2014), pp. 5422–5429. doi: 10.1039/c4an01361a (cited on page 88).
- [261] D. P. Duarte, R. N. Nogueira, and L. B. Bilro. "A low-cost liquid refractive index sensor based on plastic optical fibre and CCD array". In: *Measurement Science and Technology* 31.4 (2020), p. 047001. doi: 10.1088/1361-6501/ab46ff (cited on page 88).
- [262] B. Schreiber, C. Wacinski, and R. Chiarello. "Index of Refraction as a Quality Control Metric for Liquids in Pharmaceutical Manufacturing". In: *Pharmaceutical Engineering* 33.2 (2013), pp. 1–7 (cited on pages 88, 91).
- [263] L. V. Allen Jr. "Quality control analytical methods: refractive index." In: *International Journal of Pharmaceutical Compounding* 19.1 (2015), pp. 43–47 (cited on page 88).
- [264] W. Schottky. "Über spontane Stromschwankungen in verschiedenen Elektrizitätsleitern". In: *Annalen der Physik* 362.23 (1918), pp. 541–567. doi: 10.1002/andp.19183622304 (cited on page 89).
- [265] Y. M. Blanter and M. Büttiker. "Shot noise in mesoscopic conductors". In: *Physics Reports* 336.1-2 (2000), pp. 1–166. doi: 10.1016/S0370-1573(99)00123-4 (cited on page 89).
- [266] C. W. J. Beenakker and C. Schonenberger. "Quantum shot noise". In: *Physics Today* 56.5 (2003), p. 37. doi: 10.1063/1.1583532 (cited on page 89).
- [267] M. Xiao, L.-A. Wu, and H. J. Kimble. "Precision measurement beyond the shot-noise limit". In: *Physical Review Letters* 59.3 (1987), p. 278. doi: 10.1103/PhysRevLett.59.278 (cited on page 89).



- [268] J. Abadie, B.P. Abbott, R. Abbott, T.D. Abbott, M. Abernathy, C. Adams, R. Adhikari, C. Affeldt, P. Ajith, B. Allen, G. S. Allen, E. Amador Ceron, D. Amariutei, R. S. Amin, S. B. Anderson, W. G. Anderson, K. Arai, M. A. Arain, M. C. Araya, S. M. Aston, et al. "A gravitational wave observatory operating beyond the quantum shot-noise limit". In: *Nature Physics* 7.12 (2011), pp. 962–965. doi: [10.1038/nphys2083](https://doi.org/10.1038/nphys2083) (cited on page 89).
- [269] S. Kalinin, E. Sisamakias, S. W. Magennis, S. Felekyan, and C. A. M. Seidel. "On the origin of broadening of single-molecule FRET efficiency distributions beyond shot noise limits". In: *The journal of physical chemistry B* 114.18 (2010), pp. 6197–6206. doi: [10.1021/jp100025v](https://doi.org/10.1021/jp100025v) (cited on page 89).
- [270] C. Lee, F. Dieleman, J. Lee, C. Rockstuhl, S. A. Maier, and M. Tame. "Quantum plasmonic sensing: beyond the shot-noise and diffraction limit". In: *ACS Photonics* 3.6 (2016), pp. 992–999. doi: [10.1021/acsp Photonics.6b00082](https://doi.org/10.1021/acsp Photonics.6b00082) (cited on page 89).
- [271] M. Zhang, J. Soutanis, I. Novikova, and E. E. Mikhailov. "Generating squeezed vacuum field with nonzero orbital angular momentum with atomic ensembles". In: *Optics Letters* 38.22 (2013), pp. 4833–4836. doi: [10.1364/OL.38.004833](https://doi.org/10.1364/OL.38.004833) (cited on page 89).
- [272] R. Schödel, A. Walkov, and A. Abou-Zeid. "High-accuracy determination of water vapor refractivity by length interferometry". In: *Optics Letters* 31.13 (2006), pp. 1979–1981. doi: [10.1364/OL.31.001979](https://doi.org/10.1364/OL.31.001979) (cited on page 90).
- [273] R. Schödel. "Utilization of coincidence criteria in absolute length measurements by optical interferometry in vacuum and air". In: *Measurement Science and Technology* 26.8 (2015), p. 084007. doi: [10.1088/0957-0233/26/8/084007](https://doi.org/10.1088/0957-0233/26/8/084007) (cited on page 90).
- [274] R. Schödel, A. Walkov, M. Voigt, and G. Bartl. "Measurement of the refractive index of air in a low-pressure regime and the applicability of traditional empirical formulae". In: *Measurement Science and Technology* 29.6 (2018), p. 064002. doi: [10.1088/1361-6501/aab31a](https://doi.org/10.1088/1361-6501/aab31a) (cited on page 90).
- [275] Y. Ren, S. Qiu, T. Liu, and Z. Liu. "Compound motion detection based on OAM interferometry". In: *Nanophotonics* 11.6 (2022), pp. 1127–1135. doi: [10.1515/nanoph-2021-0622](https://doi.org/10.1515/nanoph-2021-0622) (cited on page 91).
- [276] Q. Zhao, M. Dong, Y. Bai, and Y. Yang. "Measuring high orbital angular momentum of vortex beams with an improved multipoint interferometer". In: *Photonics Research* 8.5 (2020). doi: [10.1364/prj.384925](https://doi.org/10.1364/prj.384925) (cited on page 91).
- [277] M. Dong, L. Zhu, B. Jiang, S. Fan, and Z. Chen. "Concentrated radiative cooling and its constraint from reciprocity". In: *Optics Express* 30.1 (2022), pp. 275–285. doi: [10.1364/OE.445544](https://doi.org/10.1364/OE.445544) (cited on page 94).
- [278] J. Peoples, Y.-W. Hung, X. Li, D. Gallagher, N. Fruehe, M. Pottschmidt, C. Breseman, C. Adams, A. Yuksel, J. Braun, T. Horton, and X. Ruan. "Concentrated radiative cooling". In: *Applied Energy* 310 (2022), p. 118368. doi: [10.1016/j.apenergy.2021.118368](https://doi.org/10.1016/j.apenergy.2021.118368) (cited on page 94).



# List of Figures

2.1	Thermal conduction illustrated schematically . . . . .	7
2.2	Convection illustrated schematically . . . . .	8
2.3	Thermal radiation illustrated schematically . . . . .	9
2.4	View factor in Cartesian and spherical coordinates . . . . .	10
2.5	Planck spectra for different temperatures . . . . .	12
2.6	Total emissivities of selected materials . . . . .	15
2.7	Radiative thermal exchange between the Sun, the Earth and the universe . . .	16
2.8	Planck spectra of the Sun, the Earth and the universe . . . . .	17
2.9	Transmittance of the Earth's atmosphere . . . . .	18
2.10	Solar spectrum above and below the Earth's atmosphere . . . . .	19
2.11	Basic interferometer in a Michelson configuration . . . . .	23
2.12	Fundamental Gaussian mode . . . . .	25
2.13	Spin angular momentum and orbital angular momentum . . . . .	26
2.14	Laguerre Gaussian mode . . . . .	27
2.15	Beam profiles of LG modes . . . . .	28
2.16	LG modes with different topological charges . . . . .	29
2.17	The phase distribution in LG beams . . . . .	30
2.18	Interference of two OAM beams with $l = 6$ and $l = -6$ . . . . .	32
3.1	Planck spectra of the room temperature sample and cryostat cooled sample .	37
3.2	Reflectance of the metal velvet coating . . . . .	38
3.3	Germanium window transmission . . . . .	38
3.4	Tunable view factor of the sample . . . . .	40
3.5	Concepts of enhancing the thermal exchange of two bodies . . . . .	41
3.6	Reflectance of the bare Au elliptical mirror . . . . .	42
3.7	Illustrating the view factor . . . . .	43
3.8	Schematic of the spatially structured radiative cooling setup . . . . .	45
3.9	Exemplary IR camera image . . . . .	46
3.10	Lateral temperature profile for different cryostat temperatures . . . . .	47
3.11	Temperature profiles of coated borosilicate glass and metal velvet . . . . .	49
3.12	Advanced cooling pattern . . . . .	50
3.13	Decreasing the cold reservoir diameter . . . . .	51

---

3.14	Cooling dynamics of the metal velvet sample . . . . .	53
3.15	Cooling dynamics of a biological sample . . . . .	55
3.16	Schematic supercooling of a liquid . . . . .	56
3.17	Home-built microfluidic chip . . . . .	58
3.18	Radiative supercooling of hexadecane . . . . .	59
3.19	Bi-exponential fitting of the hexadecane cooling process . . . . .	61
4.1	Schematic of the interferometer setup . . . . .	64
4.2	Spiral phase plate . . . . .	65
4.3	Turning the helicity of an OAM beam . . . . .	66
4.4	OAM beams and interference patterns for various SPPs . . . . .	68
4.5	Phase shifts leading to an interference pattern rotation . . . . .	69
4.6	Evaluation software calculating the rotation angle for each acquisition frame	70
4.7	Fluctuations of the rotation angle over time . . . . .	71
4.8	Fluctuations of the rotation angle from frame to frame . . . . .	72
4.9	Fourier transformation of the rotation angle fluctuation . . . . .	73
4.10	Flow cell for liquid samples . . . . .	74
4.11	Temperature sensing of the flow cell with IR camera . . . . .	75
4.12	Acquired temperature data . . . . .	77
4.13	Mono-exponential fits of change in refractive index and temperature data . .	78
4.14	Change in refractive index against temperature . . . . .	79
4.15	NaCl concentration measurements . . . . .	81
4.16	Refractive index dependence on concentration of NaCl . . . . .	82
4.17	Glucose concentration measurements . . . . .	83
4.18	Refractive index dependence on concentration for glucose . . . . .	84
4.19	NaCl literature comparison . . . . .	85
4.20	Glucose literature comparison . . . . .	86
4.21	Optical absorbance measurements . . . . .	87

# List of Tables

3.1	Surface areas of the hot and cold hemisphere sectors . . . . .	44
3.2	Fit parameters of the supercooling dynamics in hexadecane . . . . .	60
3.3	Half-life of the supercooling peak in hexadecane . . . . .	61
4.1	Literature values of the thermo-optic coefficient of ddH <sub>2</sub> O . . . . .	79
4.2	Comparison of the OAM interferometer and best in class interferometers . . .	90



# Acknowledgments

*The highest forms of understanding we can achieve are laughter and human compassion.*  
- Richard Feynmann

With this in mind, I would like to mentioned the people in my life, who supported me on this journey and without whom this work would not have been possible.

First are foremost I would like to thank **Prof. Dr. Jochen Feldmann** for providing the framework for this doctoral thesis and your guidance throughout. Over the years we've had many helpful discussions and managed to develop novel ideas from scratch to publication. I learned many valuable scientific and leadership lessons from you. The new facilities at the Nano-Institute provide an excellent basis for conducting research.

**PD Dr. Theobald Lohmüller** – I am very grateful for the time I got to work with you. We've worked well together on several projects, developed many ideas and I really appreciate your guidance and support throughout my PhD. From your signature rooftop Margaritas to multiple iterations on the manuscripts and many other documents, to great stories and fun facts – thank you!

**Prof. Dr. Jacek Stolarczyk** you are actually the reason I joined the PhOG group - thank you for your Optoelectronics II lecture and your encouragement that I could completely change fields once again after my Master's. You welcomed me into the group in Venice and ever since we had many fun events and talks, not to forget your famous Mad Dog.

**Prof. Dr. Alexander Urban** our overlap at the chair was not that big but you were always nearby in the new building and your door was always open. Thank you for all the fun times we had together!

**Dr. Michael Fedoruk** – I want to thank you for the great discussions, interesting ideas and solid solutions to problems. I learned a lot from you and was very happy to be able to work together with you.

**Dr. Sebastian Rieger** thank thou for thou pleasant collaboration and hence great scientific input over the years.

**Simone Ezendam** – you're definitely the person who accompanied me longest on this journey. We met right in the first semester and by the third we were studying together almost every day. If it wasn't for you, I would not have come this far. Since then we managed to do our Master's thesis together and I remember the day in Venice (your birthday) so well when you interviewed for the Maier chair. I am really happy we remained close throughout all degrees and I am infinitely grateful for all your help, your advice, your listening and lunches.

**Gerlinde Adam** you are definitely my work mom. You've always provided me with chocolate and support at times of need and I could always rely on you. Thank you for everything and here you have it in writing: I will come visit!

Thank you **Stefan Niedermaier** for always having a solution to every problem imaginable. You own every type of glue or tape imaginable and made our project very enjoyable. You are the real-life McGyver.

**Talee Barghouti** – thank you for always helping with chemistry lab-related problems and all the flow cells.

My uttermost thanks goes to my thesis correction committee, **Anja Barfüsser, Ilka Vincon, Mariam Kurashvili, Dominik Kammerer and Christian Kerschbaumer!** You saved me from many small errors and definitely streamlined this work. Thank you also for the great time together!

**Lucas Fochler, Michael Reichenspurner, Max Gruber, Lars Mannich** thank you for letting me support and guide you during your Master's and Bachelor's theses. You've helped me become a better leader and I truly enjoyed working with you.

**Dr. Alexander Richter, Francis Schuknecht, Simone Strohmer, Philipp Bootz, Viola Steidl, Matthias Kestler, Fei He, Jinhua Zhang, Dr. Amrita Dey, Dr. Tushar Debnath, Dr. Jiawen Fang, Dr. Yiou Wang** and everyone else from the chair for the great times we had together, even during a pandemic we managed to hold up our team spirit.

**Dr. Sebastian Rieger**, I doubt I could prank you one last time and actually have you believe that my gratitude to you could be expressed in a single line, but I had to try. We've walked our journeys together since the Bachelor's thesis and I am more than happy that we continued our journey together until the very end of our academic careers. You were a big part of keeping me sane all this time and helping me grow into the person I am today. You became like a brother to me and I'm sure deep in our Bavarian ancestry we can find where we are actually related. Sepp, we are not just lucky, we've earned it!

**Dr. Bernhard Bohn** – you were one of the first Phoggies I got to meet in Venice and since then we've come a long way. Even if we never did a paper together, we managed to do lots of little projects, from Christmas cards to stages that never got finished. You've stood by me during the hardest times of my PhD and celebrated the wins with me. No matter what, you always supported me. You are one of the most loyal, supportive and caring people I know. I am forever grateful for all you've done for me and I am more than happy that we met each other here. I'm looking forward to all of our big and small projects still to come.

My parents **Christine, Christian**, my brother **Tim** and my grandmother **Gisi**: I am extremely lucky to have the most supportive family I could imagine. You're always providing me with the most important backbone – a place to escape to, emotional support, appropriate drinks for celebrations and the confidence that has made me who I am today. Thank you for the unconditional love all the way.